BAYESIAN ANALYSIS OF SYSTEMATIC EFFECTS IN INTERFEROMETRIC OBSERVATIONS OF THE COSMIC MICROWAVE BACKGROUND POLARIZATION

by

Ata Karakci

B.Sc., Bogazici University; Istanbul, Turkey, 2002

M.Sc., Bogazici University; Istanbul, Turkey, 2004

Submitted in partial fulfillment of the requirements
for the degree of Doctor of Philosophy in the
Department of Physics at Brown University

Providence, Rhode Island

May 2014

This dissertation by Ata Karakci is accepted in its present form by
the Department of Physics as satisfying the dissertation requirement
for the degree of Doctor of Philosophy.

Date ______________ ______________________________________

Gregory S. Tucker, Advisor

Recommended to the Graduate Council

Date ______________ ______________________________________

Ian Dell’Antonio, Reader

Date ______________ ______________________________________

Savvas Koushiappas, Reader

Approved by the Graduate Council

Date ______________ ______________________________________

Peter M. Weber, Dean of the Graduate School

Vitae

Ata Karakci was born in Ödemiş, İzmir, Turkey in 1980. He graduated from İstanbul's Boğaziçi Üniversitesi in 2002 with a Bachelor of Science degree in physics. He received his Master of Science degree in physics from Boğaziçi Üniversitesi in 2004.

Publications:

- Sutter, P. M., Wandelt, B. D., McEwen, J. D., Bunn, E. F., Karakci, A., Korotkov, A., Timbie, P., Tucker, G. S. and Zhang, L. (2013) *Probabilistic image reconstruction for radio interferometers*, to appear in MNRAS
  arXiv:1309.1469

- Karakci, A., Zhang, L., Sutter, P. M., Bunn, E. F., Korotkov, A., Timbie, P., Tucker, G. S. and Wandelt, B. D. (2013) *Systematic Effects in Interferometric Observations of the CMB Polarization*, ApJS 207 14, 2013
  arXiv:1302.6608

- Karakci, A., Sutter, P. M., Zhang, L., Bunn, E. F., Korotkov, A., Timbie, P., Tucker, G. S. and Wandelt, B. D. (2013) *Bayesian Inference of Polarized CMB Power Spectra from Interferometric Data*, ApJS 204 10, 2013
  arXiv:1209.2930

- Zhang, L., Karakci, A., Sutter, P. M., Bunn, E. F., Korotkov, A., Timbie, P., Tucker,

G. S. and Wandelt, B. D. (2012) *Maximum likelihood analysis of systematic errors in interferometric observations of the cosmic microwave background*, ApJS, 206, 24
arXiv:1209.2676

- Arapoglu, S., Karakci, A. and Kaya, A. (2007) *S-duality in String Gas Cosmology*, Phys. Lett. B 645:255 - 260, 2007
  arXiv:hep-th/0611193

Acknowledgements

I would like to thank my advisor Gregory Tucker for his support and guidance. I also thank my collaborators Emory F. Bunn, Andrei Korotkov, Peter Timbie, Benjamin D. Wandelt, and Le Zhang for sharing their ideas, and their help. I owe special thanks to P. M. Sutter, without his previous work this thesis would not have been possible.

Finally, I would like to thank my parents Durdane and Ziyaettin, and my brothers Ali and Cem, for their constant support and encouragement.

During my last year of study, I was supported by a generous fellowship from the Galkin foundation.

To the memory of my beloved mother

Durdane Karakçı

15 July 1951 - 26 November 2013

Contents

List of Tables

List of Figures

Chapter 1

Introduction

Since the first detection of the cosmic microwave background (CMB) radiation in 1965, cosmologist have established a standard model of cosmology, ΛCDM model, to describe the structure of the universe. The model has been tested to a very high degree of precision by a wide variety of observations, such as the CMB radiation precision measurements, observations of large scale structure from the Sloan Digital Sky Survey and 2dF Galaxy Redshift Survey, and distant Type Ia supernovae observations that suggest an accelerating expansion of the universe. According to the current model the universe is spatially flat and consists of 4% baryonic matter, 23% cold dark matter (CDM) and 73% dark energy described by the cosmological constant Λ.

The homogeneity and isotropy of the observable universe is explained by an almost exponentially expanding epoch of the early universe known as inflation. During the inflationary period, Gaussian distributed quantum fluctuations in the gravitational field were amplified to cosmological scales. The primordial perturbations created during inflation leave an imprint on the CMB sky in the form of the observed cold and hot spots. These gravitational fluctuations, in turn, produce the large scale structure, such as galaxies and galaxy clusters. The CMB power spectrum measurements suggest that the fluctuations are Gaussian and nearly scale-invariant as predicted by inflation.

The CMB anisotropy observations, such as the Wilkinson Microwave Anisotropy Probe (*WMAP*) [33] and *Planck* [60] (satellites missions), and ACBAR [64] and PolarBear [41] (ground based telescopes), can be used to estimate cosmological parameters accurately by using sophisticated computer programs, such as CMBFAST [68] and CAMB [7].

The metric perturbations create quadrupole anisotropies in the CMB temperature signal, which together with Thomson scattering produce a net linear polarization of the observed CMB radiation. The polarization signal is described in terms of a combination of scalar, E-mode, and pseudo-scalar, B-mode, fields. Observation of the CMB polarization signal constrains cosmological parameters to a further precision. Furthermore, since the gravitational shock waves created during inflation are the only cause of the primordial B-modes, the measurement of the primordial B-mode spectrum, whose amplitude is a linear function of the energy scale of the inflation, would provide the most direct observational evidence for inflation. The observational projects, such as ground based observations BICEP-II [31], QUIJOTE [66], QUIET [36] and and QUBIC [63], and balloon borne experiments EBEX [65] and Spider [9], have been specifically aiming at obtaining a precise measurement of this faint, yet to be observed primordial B-mode polarization signal.

Because B-modes are not produced by scalar perturbations, they are smaller than E-modes by more than an order of magnitude. Detection of such weak signals requires excellent control of systematic effects. Since traditional imagers measure Stokes parameters by differencing two orthogonal polarizations, mismatched beams and pointing errors cause leakage from the much stronger temperature signal into the polarization signal, significantly contaminating the much weaker B-modes. Interferometers, on the other hand, directly measure the Stokes parameters without subtraction of the signals from different detectors. Thus, mismatch in the beam patterns or differential pointing errors do not cause contamination of the polarization by the temperature signal. Moreover, for finite sky patches and pixellated maps, E and B-modes mix into each other, causing major contamination of B-modes by much stronger E-modes. Since interferometric data live in

Fourier space, separation of E and B-modes can be achieved more cleanly by interferometers than imagers [58].

Interferometers have already been applied to the detection of the polarized CMB signal. The first detection of polarization anisotropies in the CMB was achieved by the Degree Angular Scale Interferometer (DASI) [35]. The Cosmic Background Imager (CBI) [55] and the Very Small Array (VSA) [10] obtained detailed observations enabling them to extract the E-mode polarization angular power spectrum up to $\ell \sim 600$. Advancing techniques, such as bolometric interferometry employed by the QUBIC experiment, provide promising developments in detecting the long-sought B-mode polarization anisotropies yet to be observed.

The basic assumption in analyzing the CMB signal is that the anisotropies are Gaussian, so that the statistical information is completely contained in the angular power spectrum C_ℓ. Since the brute force approach is computationally unfeasible, efficient methods, such as maximum likelihood and Bayesian inference methods, have been investigated for estimating the power spectrum. Since the observed CMB signal can be interpreted as a single realization of a random process, CMB data is most suitably analyzed in a Bayesian, rather than frequentist, approach.

Direct evaluation of the likelihood for the power spectrum of the CMB was possible for the early measurements, for which the signal to noise ratios were close to unity. However, computational complexity of direct likelihood evaluation scales as $\mathcal{O}(n_p^3)$, n_p being the number of pixels, making it unfeasible for current and future high resolution CMB observations. An iterative method of Bayesian sampling by a Markov Chain Monte Carlo (MCMC) process, known as Gibbs sampling, was introduced by [25] and [76]. The method was later applied to the Cosmic Background Explorer Satellite (*COBE*) data [76], extended to high-resolution on the sphere [16], applied to analysis of the *WMAP* data [4, 21, 56, 54, 13, 14], and generalized to include foreground removal [12, 15]. The Gibbs sampling analysis of CMB polarization signal was introduced by [38]. The application of

Gibbs sampling to interferometric observations of the CMB temperature signal was examined by [71]. We extended the method to analysis of interferometric data of the CMB polarization signal [28] as shown in Chapter 5.

In this chapter, we will introduce the standard model of cosmology, and discuss the theory of inflation and its predictions. Then we will present the theoretical framework of the fluctuations in the gravitational field. In Chapter 2 we will describe the nature of the CMB radiation and introduce the major sources of the anisotropies in its temperature and polarization signals. Then, we will describe how we can constrain cosmological parameters through analysis of these anisotropies on the temperature and polarization angular power spectra of the CMB. In Chapter 3 we will sketch the basic theoretical formalism behind radio interferometers and discuss their advantages over imagers in observations of the CMB polarization signal. The main categories of systematic effects in interferometric observations and their analytical treatment will also be presented in Chapter 3. As one of the main objectives of this thesis, the development of the method of Gibbs sampling for interferometric data of the CMB polarization signal will be presented in Chapter 4 where the main advantages of the method of Gibbs sampling over the frequentist approaches, such as maximum likelihood method, will also be discussed. In Chapter 5 we will present realistic simulations of systematic errors in interferometric observations of the CMB polarization signal. The main results of the thesis is the assessment of the control levels of the systematic effects in interferometric observations, which will be obtained by analyzing the simulated data by both Gibbs sampling and maximum likelihood methods. The systematic induced biases in power spectra and tensor-to-scalar ratio will also be given in Chapter 5. Further directions, such as introducing a foreground removal method within the Gibbs sampling analysis, and extending our Bayesian techniques for recovering power spectra from 2-D sky maps to 3-D data sets of HI emission-line tomography, will be discussed in Chapter 6. And finally, a summary of the results and conclusions of the thesis will be presented in Chapter 7.

1.1 Friedmann-Lemaitre-Robertson-Walker Metric

The observable universe looks the same in all directions, which leads us to the assumption that the universe is homogeneous and isotropic on large scales. Under this assumption, the space-time metric takes a simple form:

$$ds^2 = -dt^2 + a^2(t)\left[\frac{dr^2}{1-kr^2} + r^2(d\theta^2 + sin^2\theta d\phi^2)\right], \tag{1.1}$$

where $(r,\ \theta,\ \phi)$ are comoving coordinates and $a(t)$ is the scale factor describing the dynamical expansion of the universe, in units where $c = 1$. The dimensionless constant k describes the curvature of the universe: $k > 0$ corresponds to a closed, spherical universe; $k = 0$ corresponds to a flat, Euclidean universe; and $k < 0$ corresponds to an open, hyperbolic universe. The scale factor is related to the cosmological redshift z as $a(t)/a(t_0) = (1+z)^{-1}$, t_0 being present time. We can approximate the content of the universe as a non-viscous fluid whose energy-momentum tensor takes the form

$$T^{00} = \rho(t), \quad T^{0i} = 0, \quad T^{ij} = g^{ij}a^{-2}(t)p(t), \tag{1.2}$$

where ρ is the energy density and p is the pressure. The conservation equation for the energy-momentum tensor, $T^{\mu}_{\nu;\mu} = 0$, gives the relation

$$\dot{\rho} + 3H(t)(\rho + p) = 0. \tag{1.3}$$

where $H(t) = \dot{a}(t)/a(t)$ is the Hubble parameter.

The first Friedmann equation can be derived by substituting the metric (1.1) into the Einstein's equations:

$$\left(\frac{\dot{a}}{a}\right)^2 = \frac{8\pi G}{3}\rho + \frac{\Lambda}{3} - \frac{k}{a^2}. \tag{1.4}$$

The cosmological constant Λ can be interpreted as the vacuum energy density $\rho_{vac} = \Lambda/8\pi G$. We can obtain the second Friedmann equation by using Eq. (1.3) and the time derivative of Eq. (1.4):

$$\frac{\ddot{a}}{a} = -\frac{4\pi G}{3}(\rho + 3p), \tag{1.5}$$

where we have included the cosmological constant into the total energy density $\rho + \rho_{vac} \to \rho$. As we can see from Eq. (1.5), the sign of $(\rho + 3p)$ determines whether the universe is accelerating $(\ddot{a} > 0)$ or decelerating $(\ddot{a} < 0)$. The equations of state for cold matter $(p_m = 0)$ and radiation $(p_r = \rho_r/3)$ indicate that the expansion of universe containing only matter and radiation would be slowed down by gravity. However, the pressure from dark energy $(p_\Lambda = -\rho_\Lambda)$ accelerates the expansion of the universe.

The evolution equation for Hubble parameter is determined from Eq. (1.4) [77]:

$$H(z) = H_0 \left[\Omega_\Lambda + \Omega_k(1+z)^2 + \Omega_m(1+z)^3 + \Omega_r(1+z)^4\right]^{\frac{1}{2}}, \tag{1.6}$$

where H_0 is the present day Hubble parameter, $\rho_{cr} = 3H_0^2/8\pi G$ is the critical density, and $\Omega_i = \rho_i/\rho_{crit}$ are the present fractional densities of matter $(i = m)$, radiation $(i = r)$, and dark energy $(i = \Lambda)$. The fractional curvature density is given by $\Omega_k = -k/a^2(t_0)H_0^2 = 1 - \Omega_m - \Omega_r - \Omega_\Lambda$. The sign of the curvature constant k is determined by whether the present density is greater $(k = +1)$ or less $(k = -1)$ than the critical density for which $k = 0$. Current observational data suggests that $k \approx 0$; i.e., the universe is spatially flat.

Since each fractional density has a different dependence on the scale factor, the equation of state of the universe changes with the expansion. The expansion of the universe, the abundance of the light elements, and the observations of the CMB radiation suggest that the universe evolved from a radiation dominated era into a matter dominated era first, then finally into a dark energy dominated era.

In order to explain the observed homogeneity, isotropy, and the flatness of the universe, cosmologists theorized that the early universe must have gone through an inflationary phase.

1.2 Inflation

The Inflationary scenario can solve some of the classical cosmological problems, such as the flatness problem, the horizon problem, and the magnetic monopoles problem, by asserting that the early universe went through an exponential expansion for a short period of time. It is possible that during the inflation, a small patch would have increased to the cosmological scales. After the inflationary phase ended, the universe entered into a period of ”reheating” in which matter and radiation were created.

1.2.1 Flatness Problem

Measurements of the CMB anisotropies, together with Type Ia supernovae observations and measurements of the ages of the oldest stars, strongly favor a spatially flat universe [77], which imposes strong constraints on the initial conditions. Since the end of the radiation dominated era at temperature $T \sim 10^4$K, the comoving Hubble radius $(aH)^{-1}$ has been growing as $t^{1/3} \propto T^{-1/2}$. During the radiation dominated epoch it had been growing as $t^{1/2} \propto T^{-1}$. Thus, the curvature density

$$|\Omega_k| = \frac{|k|}{(aH)^2}. \tag{1.7}$$

must have increased by a factor of 10^{16} since the time of nucleosynthesis at $T = 10^{10}$K [77]. To account for the current observed spatial flatness, $|\Omega_k|$ in the early universe must be close to zero to a great precision, a phenomenon that requires an explanation.

According to the inflationary scenario, during the inflation, the scale factor increased as $a \sim e^{Ht}$, and the Hubble parameter H was nearly a constant, which would exponentially decrease the curvature density over the time period of the inflation t_I:

$$|\Omega_k| \sim e^{-2Ht_I}, \tag{1.8}$$

solving the flatness problem.

1.2.2 Horizon Problem

At the time of last scattering ($z_L \approx 1100$), the universe has already entered into the matter dominated era, where the horizon size was approximately $d_H \sim H_0^{-1}(1 + z_L)^{-3/2}$

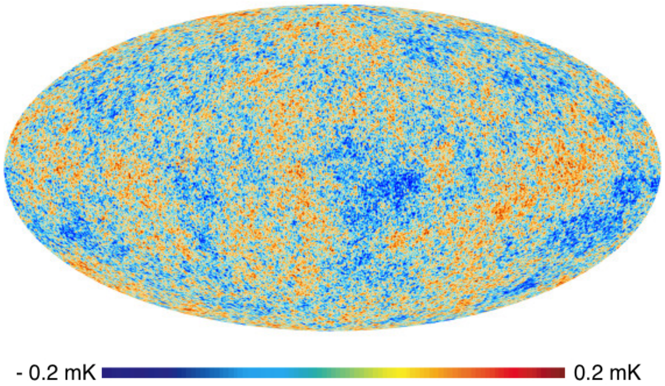

Figure 1.1: The anisotropies of the Cosmic microwave background as observed by *Planck*. The image is taken from ESA and the Planck Collaboration webpage [50]

[77]. Since the distance from the last scattering surface to present is approximately $d_L \sim H_0^{-1}(1+z_L)^{-1}$ [77], the regions on the observed sky, separated by an angle of order $d_H/d_L \sim (1+z_L)^{-1/2} \approx 1.6^\circ$ could not have thermalized at the time of last scattering. However, the nearly perfect isotropy of the observed CMB temperature field (Fig. 1.1) indicates that the regions on the last scattering surface that were not causally connected have nearly the same temperature, suggesting thermal equilibrium. This is known as the horizon problem.

During the inflation, the size of the proper horizon increases as

$$d_H(t_I) = a(t_I)\int_{t_*}^{t_I} \frac{dt}{a(t)}, \tag{1.9}$$

where t_* (possibly $-\infty$ [77]) and t_I are the times of the beginning and the end of the inflation, respectively. At the end of the inflation, the size of the horizon becomes

$$d_H(t_I) \approx \frac{a_I}{a_I H_I} e^{H_I(2t_I - t_*)}. \tag{1.10}$$

Therefore, after a sufficiently long inflationary period, the horizon is pushed beyond the comoving Hubble radius $(a_I H_I)^{-1}$ and the regions that were once in causal contact will appear outside of the Hubble radius at the time of last scattering.

1.2.3 Magnetic Monopoles

According to *Grand Unified Theories*, a large number of stable magnetic monopoles must be created during the spontaneous symmetry breaking at the end of the epoch of grand unification. Their density must be on the order of nucleon density of the universe, yet, not a single monopole has ever been observed. However, if the monopoles are created during the inflation, their density will be exponentially decreased to a negligible fraction of the matter density by the time of reheating.

1.2.4 Slow-roll Inflation

The exponential expansion of the early universe can be explained by introducing a spatially homogeneous scalar field $\phi(t)$, called the *inflaton*, which dominates the early universe. Since the Hubble constant decreases very slowly as the inflaton slowly rolls down its large and nearly flat potential $V(\phi)$, the scale parameter grows almost exponentially. The inflaton action can be written as

$$\mathcal{S} = \int d^4x\sqrt{|g|}\mathcal{L} = \int d^4x\sqrt{|g|}\left[\frac{1}{2}\partial_\mu\phi\partial^\mu\phi + V(\phi)\right], \tag{1.11}$$

where g is the determinant of the Robertson-Walker metric. The density and the pressure of inflaton is found by its energy-momentum tensor $T_{\mu\nu} = \partial_\mu\phi\partial_\nu\phi - g_{\mu\nu}\mathcal{L}$:

$$\rho = T_{00} = -\frac{1}{2}\dot{\phi}^2 + V(\phi), \tag{1.12a}$$

$$p = -T_{ii} = -\frac{1}{2}\dot{\phi}^2 - V(\phi). \tag{1.12b}$$

Slow roll occurs when the potential term is much larger than the kinetic term; i.e., $V(\phi) \gg \frac{1}{2}\dot{\phi}^2$. Then, according to the first Friedman equation (1.4), the Hubble constant becomes nearly constant, $H \approx \sqrt{8\pi GV(\phi)/3}$, and the equation of state becomes

$$p \approx V(\phi) \approx -\rho, \tag{1.13}$$

which solves Eq. (1.5) for an exponentially growing scale parameter $a(t) \sim e^{Ht}$ [77]. Inflation ends when the potential becomes smaller than the kinetic energy and the inflaton decays into ordinary matter, which is known as reheating.

The expectation value of the inflaton, ϕ_{cl}, given by the solution of the classical Euler-Lagrange equation for the action (1.11), is responsible for the inflation. Whereas, the quantum fluctuations $\delta\phi$ around ϕ_{cl} generate perturbations on the homogeneous and isotropic metric which is being inflated by ϕ_{cl}.

1.3 Gravitational Fluctuations

The approximate homogeneity and isotropy of the observable universe can be described by the Robertson-Walker metric. In reality, fluctuations in the gravitational field created during inflation cause departures from homogeneity and isotropy. The analysis of these metric perturbations is illuminating in understanding the observed fluctuations in the cosmic microwave background and evolution of structure. Since the observable universe is nearly homogeneous the actual metric can be treated as a first-order perturbation over the Robertson-Walker metric [77]:

$$g_{\mu\nu} = g_{\mu\nu}^{RW} + h_{\mu\nu} \tag{1.14}$$

where $g_{\mu\nu}^{RW}$ is the unperturbed Robertson-Walker metric and $h_{\mu\nu} = h_{\nu\mu}$ is a small perturbation. The perturbation to the metric can be decomposed into scalar, divergenceless vector, and divergenceless, traceless symmetric tensor parts [77]:

$$h_{00} = -E, \tag{1.15a}$$

$$h_{i0} = a\left[\frac{\partial F}{\partial x^i} + G_i\right], \tag{1.15b}$$

$$h_{ij} = a^2\left[A\delta_{ij} + \frac{\partial^2 B}{\partial x^i \partial x^j} + \frac{\partial C_i}{\partial x^j} + \frac{\partial C_j}{\partial x^i} + D_{ij}\right], \tag{1.15c}$$

where $\nabla^2 F = a^{-1}\partial_i h_{i0}$, $\nabla^2 A + \nabla^4 B = a^{-2}\partial_i\partial_j h_{ij}$, $3A + \nabla^2 B = a^{-2}h_{ii}$, and $\nabla^2 C_i = a^{-1}\partial_j h_{ij} - \partial_i[A + \nabla^2 B]$. The perturbations C_i, G_i, and D_{ij} satisfy the conditions

$$\frac{\partial C_i}{\partial x^i} = \frac{\partial G_i}{\partial x^i} = 0, \quad \frac{\partial D_{ij}}{\partial x^i} = 0, \quad D_{ii} = 0. \tag{1.16}$$

With theses decompositions and using the Einstein equations and the conservation equation for the energy-momentum tensor, the gravitational field perturbations fall into three categories [77]:

1.3.1 Scalar (Density) Perturbations

The perturbations involving the scalars A, B, E, and F constitute the scalar modes. They describe the perturbations in the density of the primordial plasma at last scattering and they are the only type of perturbations that can lead to structure formation through gravitational instability.

During the course of the evolution of cosmic fluctuations, the radiation temperature and gravitational potential gradients create a quadrupole anisotropy that can be described in terms of an *effective temperature*;

$$(\Delta T/T)_{eff} = \Delta T/T + \phi, \tag{1.17}$$

where ϕ is the gravitational potential. These gradients cause a bulk flow from hot to cold effective temperature. The local quadrupole moment caused by hot photons flowing into cold regions is essential for creating a polarization pattern through Thomson scattering, as discussed in the next chapter.

1.3.2 Vector (Vortical) Perturbations

The perturbations involving the divergenceless vectors C_i and G_i constitute the vector modes which represent vortical motions of the plasma. Because of the Doppler shift, the radiation fields at either side of the vortex exhibits opposing dipole patterns, creating a quadrupole moment around the vortex. As before, the quadrupole anisotropy polarizes the radiation through Thomson scattering. However, since the vortical modes are not associated with density, they decay as $1/a^2$ as the universe expands.

1.3.3 Tensor (Radiative) Perturbations

The perturbations involving the traceless divergenceless tensor D_{ij} constitute the tensor modes which represent the wave equation for gravitational radiation. As the gravitational waves distort the space in a quadrupole pattern a local quadrupole anisotropy is created in the radiation temperature which in turn is converted into polarization by Thomson scattering. We will examine these quadrupole anisotropies in detail when discussing the CMB polarization in the next chapter.

Chapter 2

The Cosmic Microwave Background

The observational evidence for the standard model of cosmology suggests that the early universe consisted of a hot dense plasma, which is in thermal equilibrium with radiation because of the rapid collisions of photons with baryonic matter. Since radiation in equilibrium with matter is described by the *black body spectrum*, at temperature T, the intensity of the radiation at frequency ν is given by the Planck's law:

$$I_\nu(T) = \frac{2h\nu^3}{c^2} \frac{1}{\exp(h\nu/k_B T) - 1} \ , \tag{2.1}$$

where h is the Planck's constant and k_B is the Boltzmann's constant.

As the universe expanded, the matter cooled down and at the time of *last scattering* around 380,000 years after the Big Bang, when the temperature of the universe was of order 3,000 K, the radiation *decoupled* from matter; i.e., the mean free path of the photons became on the order of the size of the universe. After decoupling, the radiation began a free expansion retaining its black body spectrum with a redshifted temperature of

$$T = T_0(1 + z). \tag{2.2}$$

The existence of a cosmic black body radiation was already predicted in the late 1940s [18, 1, 2, 19]. However, observational evidence did not come until A. Penzias and R. Wilson's famous discovery by a radio telescope in 1965 [59].

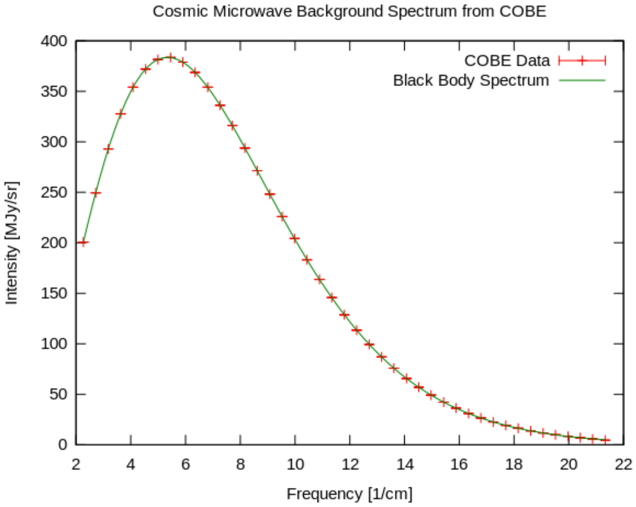

Figure 2.1: Spectrum of the cosmic background radiation measured by the FIRAS radiometer on *COBE*. The temperature of the black body radiation is found as 2.728 K [17]. Intensity in kiloJansky per steradian is plotted against the reciprocal wavelength cm^{-1}. The 1σ uncertainties in both directions are shown by red error bars.

After the initial observation of a 3.5 K radiation at a wavelength 7.5 cm, further measurements were made down to a wavelength of 3.2 cm. However, to established the black body nature of the radiation, measurements had to be made at wavelengths shorter than 0.3 cm, where the intensity of the radiation has its maximum. Since the earth's atmosphere becomes opaque at such short wavelengths, *COBE* was launched in 1989 [47]. The cosmic microwave background spectrum measured by the *COBE* (see Fig. 2.1) is the most precise black body spectrum observed in nature [78].

2.1 Temperature Anisotropies

Although the CMB radiation is almost perfectly homogeneous and isotropic to a large extent, the most important information about the evolution of the universe comes from small departures from isotropy in its spectrum.

The statistical aspects of these anisotropies can be best understand by expanding the temperature fluctuation in spherical harmonic basis [77]:

$$\Delta T(\hat{n}) = T(\hat{n}) - T_0 = \sum_{m=-\ell}^{\ell} \sum_{\ell=1}^{\infty} a_{\ell m} Y_\ell^m(\hat{n}), \quad T_0 = \frac{1}{4\pi} \int d^2\hat{n} T(\hat{n}). \tag{2.3}$$

The *dipole anisotropy*, arising from the earth's motion relative to the Hubble flow, contributes to the $\ell = 1$ and $m = 0$ terms.

Since according to the ΛCDM model the coefficients $a_{\ell m}$ describe a pure Gaussian random field, all the statistical information is contained in the angular power spectrum C_ℓ:

$$\langle a_{\ell m} a^*_{\ell' m'} \rangle = \delta_{\ell \ell'} \delta_{m m'} C_\ell \tag{2.4}$$

where $a^*_{\ell m} = a_{\ell\ -m}$ and the average is to be taken over all the possible positions in the universe from which the radiation could be observed. Since we can only observe the CMB from a single position, namely the earth, the observed spectrum is actually averaged over m instead of position:

$$C_\ell^{obs} = \frac{1}{2\ell + 1} \sum_m a_{\ell m} a^*_{\ell m}. \tag{2.5}$$

The mean square difference between the actual and the observed angular power spectra is known as the *cosmic variance.*

$$\left\langle \left(\frac{C_\ell - C_\ell^{obs}}{C_\ell} \right) \right\rangle = \frac{2}{2\ell + 1}. \tag{2.6}$$

Since cosmic variance is more pronounced for small values of ℓ, accuracy of C_ℓ measurements for small ℓ is limited.

On the other hand, towards the high ℓ values, the anisotropies in the CMB temperature are dominated by the *Sunyaev-Zel'dovich effect* [77] which is created by the scattering of the CMB photons by energetic charged particles along the line of sight in intergalactic space within galaxy clusters. Measurements of C_ℓ for large ℓ are corrupted by such foreground effects.

The cosmologically interesting contribution to the CMB spectrum come from the so called *primary anisotropies*, which have their origin in the early universe. Primary anisotropies arise from four main sources which are caused by the fluctuations in the gravitational field [77]:

i) Sachs-Wolfe effect: Time independent perturbations in the gravitational potential at the surface of last scattering causes the photons undergo gravitational redshift or blueshift. These perturbations also change the local rate of expansion, effectively changing the observed temperature by a fractional amount according to Eq. (2.2). In Newtonian approximation, the angular power spectrum due to the Sachs-Wolfe effect is found to be [77]

$$C_{\ell,SW} = \frac{24\pi Q^2}{5\ell(\ell+1)} \tag{2.7}$$

where Q is known as the quadrupole moment. SW effect is the first observed primary CMB anisotropy detected by *COBE* [69], which revealed the value of quadrupole moment as $Q = 18 \pm 0.7\ \mu$K for $2 \leq \ell \leq 40$.

ii) Integrated Sachs-Wolfe effect: Since the energy gained by photons falling into a time dependent gravity well is not equal to the energy lost when climbing out of it, the time dependent perturbations in the gravitational potential between the time of last scattering ($z = 1,090$) and present cause fluctuations in the observed temperature of the CMB radiation, which mainly affects the angular power spectrum for $\ell < 10$ [77].

iii) Doppler effect: Fluctuations in the plasma velocity also create a temperature anisotropy through Doppler shift. Since only compressional modes, for which the velocity can be written as a gradient, survive the expansion, Doppler effect contribution in power spectrum will be suppressed for small wave numbers corresponding to the multipole range of $\ell \ll 100$ [77].

iv) Intrinsic temperature fluctuations: Since the intrinsic temperature fluctuations at the time of last scattering are driven by the perturbations in the plasma density, their contribution is also suppressed for small wave numbers.

The temperature angular power spectrum for $10 < \ell < 50$ is dominated by Sachs-Wolfe effect [77], whereas anisotropies for $\ell \geq 50$ are dominated by intrinsic perturbations in the gravitational field.

The scalar perturbations introduced in section 1.3 can be simplified by choosing the Newtonian gauge, where $F = B = 0$ and, under the assumption of spatial homogeneity of the fluctuations, $E = A$. Writing $A = -2\Psi$, the perturbed metric becomes

$$g^s_{00} = -(1 + 2\Psi), \quad g^s_{0i} = 0, \quad g^s_{ij} = a^2(1 - 2\Psi)\delta_{ij}, \tag{2.8}$$

where the superscript s indicates scalar perturbations. The power spectrum of the scalar perturbations

$$\langle \Psi_{\mathbf{k}} \Psi_{\mathbf{k}'} \rangle = (2\pi)^3 \delta^3(\mathbf{k} - \mathbf{k}') \frac{2\pi^2}{k^3} \mathcal{P}_s(k), \tag{2.9}$$

where $\Psi_{\mathbf{k}}$ is the Fourier component of $\Psi(\mathbf{x})$, can be approximated as a power law:

$$\mathcal{P}_s(k) = A_s \; k^{\;n_s - 1}, \tag{2.10}$$

where n_s is the *scalar spectral index*. The fact that n_s is slightly different from 1 indicates the scale dependence of the scalar modes. To the extent that the primordial perturbations are Gaussian, the power spectrum contains all the statistical information.

The primordial perturbations in the gravitational field create slightly denser regions in the primordial plasma. Over time, dark matter accumulates at these regions, acting as a source of gravitational attraction for baryonic matter. Before recombination, gravitational attraction towards over-dense regions is countered by the outward pressure from photon-baryon interactions creating pressure waves in the plasma traveling with a speed of $c/\sqrt{3}$, known as *baryon acoustic oscillations*. Decoupling relieves the pressure driven by the photon-baryon interactions and the waves freeze out, imprinting shells of baryonic matter at a characteristic length scale, called the *sound horizon*, on the surface of last scattering. This produces a harmonic series of maxima and minima in the anisotropy power spectrum [11]. The ratios of the positions of maxima and the ratios of the amplitudes depend only on fractional baryon density $\Omega_b h^2$, $\Omega_m h^2$, and n_s.

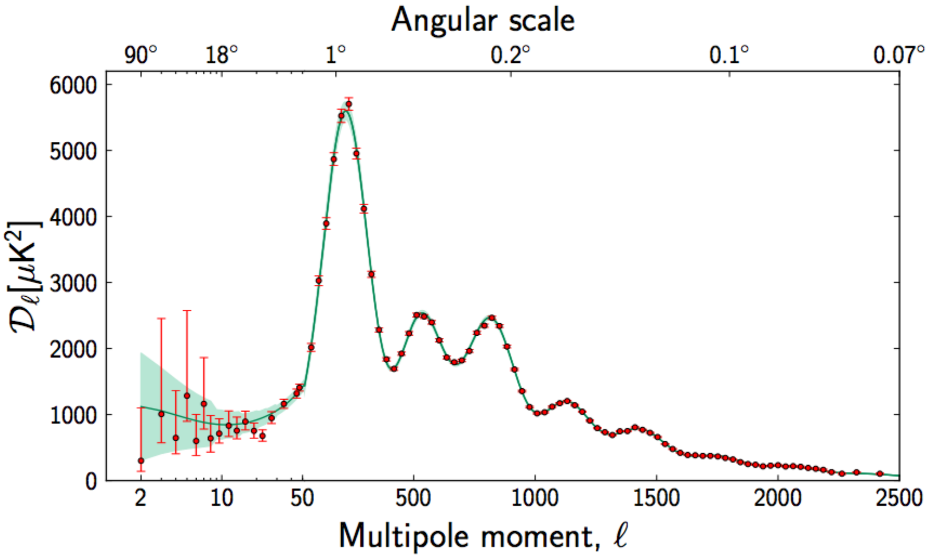

Figure 2.2: The temperature angular power spectrum of the CMB from *Planck*, showing seven acoustic peaks, that are fit by a six-parameter ΛCDM model. The shaded area represents cosmic variance. The error bars include cosmic variance. The horizontal axis is logarithmic up to $\ell = 50$, and linear beyond. The vertical scale is $\mathcal{D}_\ell = \ell(\ell+1)C_{TT,\ell}/2\pi$ [60].

The actual size of the sound horizon is given by the distance the fundamental modes travel until the time of last scattering. The position of the first peak of the scalar anisotropy power spectrum, $C^S_{TT,\ell}$, determines the apparent size of the sound horizon, which is related to the actual size by the spatial curvature and the distance to the last scattering surface, given by the Hubble parameter. Therefore, assuming that the universe is spatially flat, h can be determined from the measurements of $C^S_{TT,\ell}$ [77].

At around redshift $z \approx 10$, ultraviolet light from the first stars reionizes the neutral hydrogen formed during recombination. Scattering of the CMB photons by the reionized plasma diminishes the amplitude of $C^S_{TT,\ell}$ by a factor $\exp(-2\tau_{reion})$, where τ_{reion} is the optical depth of the reionized plasma. Therefore, measurements of $C^S_{TT,\ell}$ can only determine the combination $A_s \exp(-2\tau_{reion})$. Separate determination of the quantities A_s and $\exp(-2\tau_{reion})$ requires measurements of gravitational lensing of the CMB [60].

The first acoustic peak was tentatively detected by MAT/TOCO [48] and the result was

Parameter	Best fit	68% limits
H_0	67.11	67.4±1.4
$\Omega_b h^2$	0.022068	002207 ± 0.00033
$\Omega_c h^2$	0.12029	0.1196 ± 0.0031
Ω_Λ	0.6825	0.686 ± 0.020
Ω_m	0.3175	0.314 ± 0.020
Age (Gyr)	13.819	13.813 ± 0.058
n_s	0.9624	0.9616 ± 0.0094
τ_{reion}	0.0925	0.097 ± 0.038
$10^9 A_s$	2.215	2.23 ± 0.16

Table 2.1: Values of some of the cosmological parameters for the six-parameter ΛCDM model [61]. Results for the *Planck* temperature power spectrum data and 68% condence limits are given.

confirmed by BOOMERanG [67] and MAXIMA [40]. Their results improved to a great accuracy by *WMAP* [4]. The the most precise measurement of the CMB temperature anisotropies to this day are made by the *Planck* satellite [60]. Some of the cosmological parameters obtained from the temperature angular power spectrum of Fig. 2.2 are given in Table 2.1, where Ω_c is the fractional dark matter density.

Although Fig. 2.2 matches remarkably well with the angular power spectrum of the scalar modes, in reality, it also contains contribution from tensor modes. The power spectrum of the tensor modes D_{ij} is

$$\langle D_{\mathbf{k}} D_{\mathbf{k}'} \rangle = (2\pi)^3 \delta^3(\mathbf{k} - \mathbf{k}') \frac{2\pi^2}{k^3} \mathcal{P}_t(k), \tag{2.11}$$

where scale dependence is defined through the tensor spectral index, n_t:

$$\mathcal{P}_t(k) = A_t \; k^{n_t}. \tag{2.12}$$

The ratio of the tensor to scalar fluctuation amplitudes

$$r = \frac{\mathcal{P}_t(k)}{\mathcal{P}_s(k)} \tag{2.13}$$

depends on the energy scale of inflation: $E_{inflation} = 1.06 \times 10^{16} (\frac{r}{0.01})^{\frac{1}{4}}$ GeV [24].

The tensor-to-scalar ratio r can, in principle, be obtained from temperature power spectrum. However, as we can see from the theoretical plot in Fig. 2.3, tensor contribution

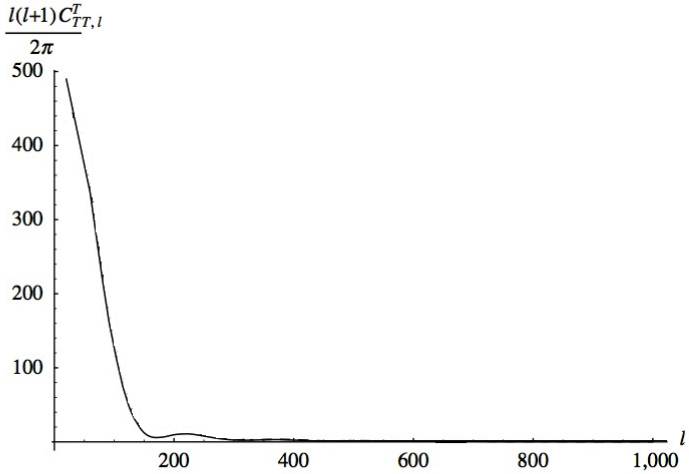

Figure 2.3: The theoretical tensor temperature angular power spectrum $\ell(\ell+1)C^{T}_{TT,\ell}/2\pi$ in μK^2, vs. ℓ [77].

to the temperature anisotropies is strongest where the cosmic variance dominates, setting a limit to the accuracy of the separation of tensor modes from scalar modes. Thus, the actual detection of tensor-to-scalar ratio has to come directly from B-mode polarization measurements. We will return to this in the following sections.

2.2 CMB Polarization

At the time of last scattering, temperature of the universe was low enough that photon-baryon interaction could be described as *Thomson scattering*, which is the classical limit of *Compton scattering*. In classical electromagnetism, the electric field of the incident wave accelerates the charged particle in the direction of its oscillation. The dipole radiation emitted by the particle is linearly polarized along the particle's motion and the intensity of the scattered radiation peaks in the direction normal to the direction of incident wave.

If the temperature of the radiation was isotropic, polarizations from incident waves coming from orthogonal directions would balance and the scattered radiation would be unpolarized. In order to produce a net polarization in the scattered radiation, the incident

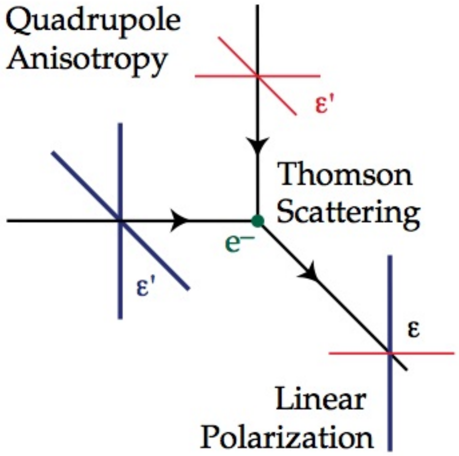

Figure 2.4: Linear polarization is generated by Thomson scattering of radiation in the presence of quadrupole temperature anisotropy. Blue and red lines represent hot and cold radiation, respectively [24].

field must have quadrupole temperature anisotropy (see Fig. 2.4.)

The quadrupole anisotropies are represented by $Y^m_{\ell=2}(\theta, \phi)$ components in the spherical harmonic expansion of the temperature field. The scalar, vector, and tensor modes described in the previous chapter correspond to $m = 0$, $m = \pm 1$, and $m = \pm 2$ modes, respectively.

2.2.1 E and B Modes

The electric field, $\boldsymbol{\mathcal{E}}$, of a radiation signal can be decomposed into orthogonal polarization components, $\boldsymbol{\mathcal{E}}_x$ and $\boldsymbol{\mathcal{E}}_y$, in the plane normal to the wave vector $\mathbf{k}$. The polarization field is described by *Stokes parameters* I, Q, U, and V, defined by the *coherence matrix* $\boldsymbol{\mathcal{S}}$:

$$\boldsymbol{\mathcal{S}}_\nu = \begin{pmatrix} \left\langle |\boldsymbol{\mathcal{E}}_x|^2 \right\rangle & \left\langle \boldsymbol{\mathcal{E}}_x \boldsymbol{\mathcal{E}}_y^* \right\rangle \\ \left\langle \boldsymbol{\mathcal{E}}_y \boldsymbol{\mathcal{E}}_x^* \right\rangle & \left\langle |\boldsymbol{\mathcal{E}}_y|^2 \right\rangle \end{pmatrix} = \frac{1}{2} \begin{pmatrix} I_\nu + Q_\nu & U_\nu - iV_\nu \\ U_\nu + iV_\nu & I_\nu - Q_\nu \end{pmatrix}, \tag{2.14}$$

where the brackets represent the time averages [27, 26]. The Stokes parameter $I = \left\langle |\boldsymbol{\mathcal{E}}_x|^2 \right\rangle + \left\langle |\boldsymbol{\mathcal{E}}_y|^2 \right\rangle$ describes the total intensity of the signal.

The linear polarization state is described by the Stokes parameters Q and U which

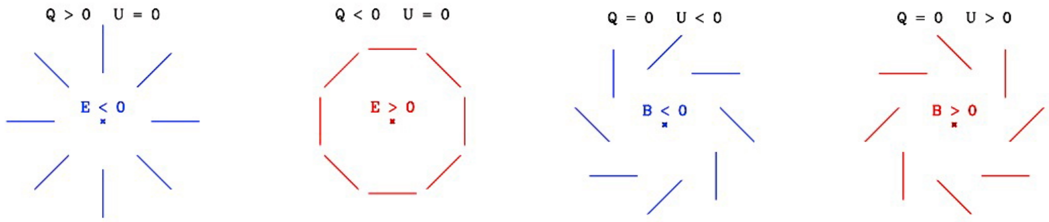

Figure 2.5: Example of positive parity E-mode and negative parity B-mode patterns [80].

form an object that transforms as a spin-2 field under a rotation by an angle ψ:

$$Q \pm iU \to Q' \pm iU' = e^{\pm 2i\psi}(Q \pm iU). \tag{2.15}$$

The Stokes parameter V describes the circular polarization state. However, we expect that the CMB radiation is only linearly polarized; i.e., $V = 0$, since circular polarization is not produced by Thomson scattering.

Because of its spin-2 nature, the polarization field cannot be expanded in ordinary spherical harmonic basis. The harmonic expansion of the polarization field requires the introduction of spin-2 spherical harmonics ${}_{\pm 2}Y_\ell^m$ [81]:

$$Q(\hat{n}) \pm iU(\hat{n}) = \sum_{\ell=2}^{\infty} \sum_{m=-\ell}^{\ell} a_{\pm 2,\ell m} \; {}_{\pm 2}Y_\ell^m(\hat{n}). \tag{2.16}$$

Through the spin-2 harmonic coefficients, a positive parity real scalar field E and a negative parity real pseudo-scalar field B can be constructed (Fig. 2.5) :

$$E(\hat{n}) = \sum_{\ell=2}^{\infty} \sum_{m=-\ell}^{\ell} a_{E,\ell m} Y_\ell^m(\hat{n}), \qquad a_{E,\ell m} = -(a_{2,\ell m} + a_{-2,\ell m})/2, \tag{2.17a}$$

$$B(\hat{n}) = \sum_{\ell=2}^{\infty} \sum_{m=-\ell}^{\ell} a_{B,\ell m} Y_\ell^m(\hat{n}), \qquad a_{B,\ell m} = i\;(a_{2,\ell m} - a_{-2,\ell m})/2, \tag{2.17b}$$

where $a^*_{E,\ell m} = a_{E,\ell\; -m}$ and $a^*_{B,\ell m} = a_{B,\ell\; -m}$. This decomposition into E and B modes completely determines the polarization field on the sphere.

The statistical information about the polarization field is contained in the two-point correlation functions. Since B type polarization is a negative parity field, there cannot

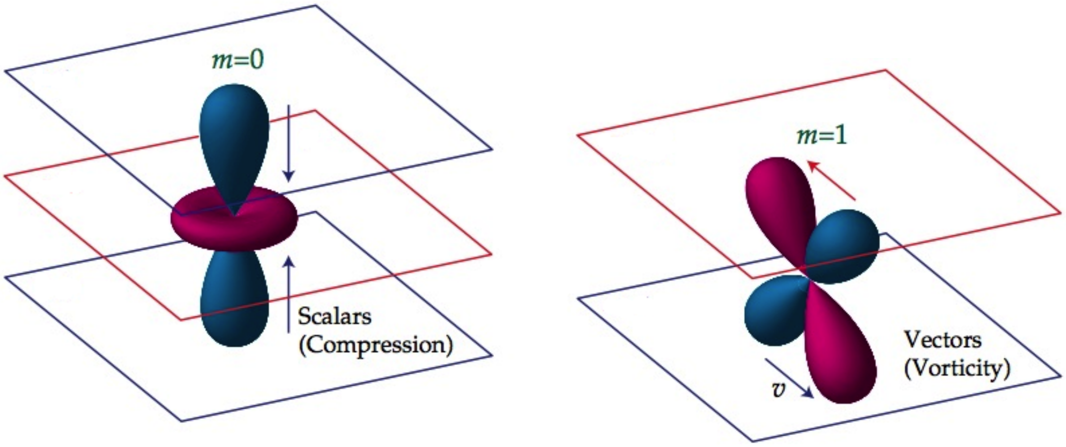

Figure 2.6: Scalar and vector perturbations induce quadrupole anisotropies, $\ell = 2$, with $m = 0$ and $m = \pm 1$, respectively [24].

be cross-correlation between B modes and temperature fluctuations or E modes. Thus, the statistical properties of the CMB fluctuations are characterized by four angular power spectra:

$$\left\langle a^*_{T,\ell m} a_{T,\ell' m'} \right\rangle = C_\ell^{TT} \delta_{\ell\ell'} \delta_{mm'}, \tag{2.18a}$$

$$\left\langle a^*_{T,\ell m} a_{E,\ell' m'} \right\rangle = C_\ell^{TE} \delta_{\ell\ell'} \delta_{mm'}, \tag{2.18b}$$

$$\left\langle a^*_{E,\ell m} a_{E,\ell' m'} \right\rangle = C_\ell^{EE} \delta_{\ell\ell'} \delta_{mm'}, \tag{2.18c}$$

$$\left\langle a^*_{B,\ell m} a_{B,\ell' m'} \right\rangle = C_\ell^{BB} \delta_{\ell\ell'} \delta_{mm'}. \tag{2.18d}$$

2.2.2 Anisotropies in the CMB Polarization

As previous discussed, the quadrupole temperature anisotropy can be produced by scalar, vector, and tensor fluctuations each having a distinct polarization pattern. We will consider each case in this section.

Scalar perturbations represent fluctuations in the density of the primordial plasma and they are the only source of structure formation. As shown in Fig. 2.6, the velocity gradient of the plasma flowing from hot to cold effective temperature induces quadrupole anisotropy because of the Doppler effect. Since density fluctuations are invariant under

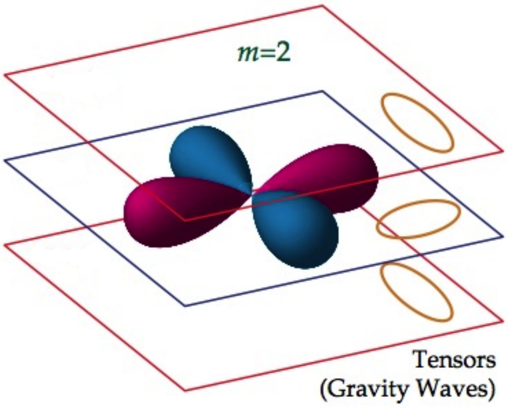

Figure 2.7: Tensor perturbations induce quadrupole anisotropies, $\ell = 2$, with $m = \pm 2$ [24].

parity, scalar perturbations can only produce E mode polarizations.

Vector perturbations are generated by the vortical motions of the primordial plasma and as shown in Fig. 2.6, quadrupole anisotropy is induced by Doppler effect from the plasma motion. However, vector modes are damped by the expansion of the universe.

Tensor perturbations, generated by primordial gravity waves predicted by the inflation, represent quadrupolar distortions in the space (Fig. 2.7), inducing gravitational shifts in the radiation frequencies. Tensor fluctuations can produce both E type and B type polarization pattern. The amplitude of the tensor B modes, which is proportional to the amplitude of the gravitational waves, depends linearly on the tensor-to-scalar ratio, which itself is a function of the energy scale of inflation.

The E modes and TE cross-correlation were first detected by DASI [35] and their accuracies were greatly improved by *WMAP* [33]. The most remarkable results of E mode observations have been the redshift z_r and the optical depth τ_r of the reionization of the intergalactic matter.

Since B type polarization is only generated by tensor modes, detection of primordial B modes will be definite evidence for inflationary gravitational waves. Figure 2.8 shows

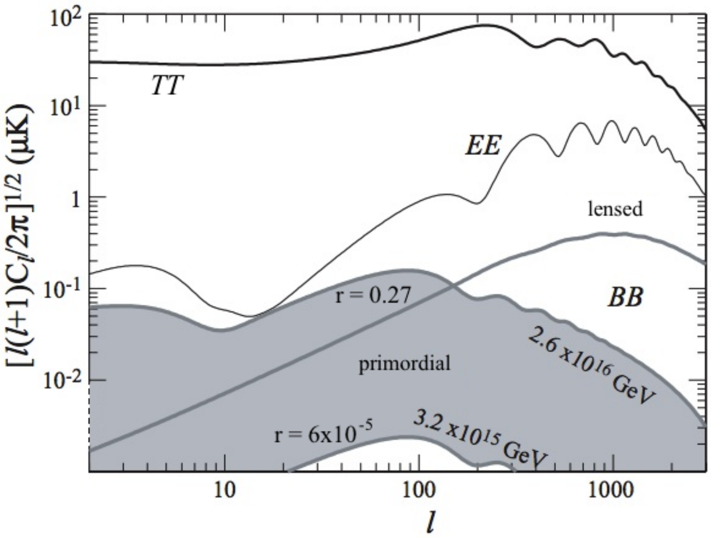

Figure 2.8: CMB power spectra of temperature and E modes compared with primordial (tensor) and lensed B modes [23]. Shaded area is bounded by the maximum allowable and minimum detectable levels of the primordial B type polarization.

upper and lower bounds of the detectable primordial B mode amplitude relative to the amplitudes of temperature and E mode spectra. Lensed B mode spectrum generated by weak gravitational lensing of E modes is also shown. Detection of primordial B modes, which are orders of magnitude fainter than E mode and temperature signals, will require excellent control of systematics.

Chapter 3

Interferometers

Interferometers have been used in radio astronomy for high resolution observations since the 1940s [74]. Angular resolution, $\Delta\theta$, of a circular aperture is determined by *Rayleigh criterion* as the angle of the first minimum of the Airy diffraction pattern:

$$\Delta\theta = 1.22\frac{\lambda}{D}, \tag{3.1}$$

where λ is the wavelength of the signal, and D is the diameter of the aperture. A single-baseline interferometer, which consists of a pair of antennas separated by a *baseline* of length $|\mathbf{b}|$, can achieve the angular resolution of a single telescope with diameter $|\mathbf{b}|$ at the expense of observed intensity [72, 74]. The technique of obtaining high resolution observations by correlating signals from a collection of antennas is known as *aperture synthesis* or *synthesis imaging.*

The interferometric data, called *visibilities*, give Fourier components of the intensity distribution of the observed object. Therefore, the power spectrum of the signal can be directly obtained from visibilities, instead of analyzing the constructed image as in the case of imagers. High accuracy measurements of CMB fluctuations have been obtained by a number of ground based interferometers, such as VSA [10], DASI [35], and CBI [55]. The polarization of the CMB was first detected by DASI and the angular power spectrum of the E mode polarization was first measured by the CBI.

In this chapter we will discuss the theory behind interferometric measurements and the relation between the power spectrum and visibilities. Then we will introduce the main categories of systematic errors in interferometric observations and their effects on visibility data.

3.1 Visibilities

Astronomical sources can be conceived of bright regions on a very large sphere of radius ρ, called the *celestial sphere*. According to Huygen's principle [72], the electric field, $\boldsymbol{\mathcal{E}}_\nu(\boldsymbol{\rho})$, distributed on the surface of the celestial sphere propagates to the observation point at $\mathbf{r}$ as

$$\mathbf{E}_\nu(\mathbf{r}) = \int \boldsymbol{\mathcal{E}}_\nu(\boldsymbol{\rho}) \frac{e^{-2\pi i\nu|\boldsymbol{\rho}-\boldsymbol{r}|/c}}{|\boldsymbol{\rho}-\boldsymbol{r}|} dS, \tag{3.2}$$

where ν is the frequency of the signal and $dS = \rho^2 d\Omega$ is the surface element on the celestial sphere. The correlation between the electric fields received at positions $\mathbf{r}_1$ and $\mathbf{r}_2$ is given by

$$c_\nu(\mathbf{r}_1, \mathbf{r}_2) = \langle \mathbf{E}_\nu(\mathbf{r}_1)\mathbf{E}^*_\nu(\mathbf{r}_2)\rangle \,. \tag{3.3}$$

With the assumption that the astronomical signals are not spatially correlated; i.e., $\langle \boldsymbol{\mathcal{E}}_\nu(\boldsymbol{\rho}_1)\boldsymbol{\mathcal{E}}^*_\nu(\boldsymbol{\rho}_2)\rangle \propto \delta(\boldsymbol{\rho}_1 - \boldsymbol{\rho}_2)$, and ignoring the terms of order r/ρ, the correlation at baseline $\mathbf{b} = \mathbf{r}_1 - \mathbf{r}_2$ can be written as

$$c_\nu(\mathbf{b}) = \int I_\nu(\mathbf{s}) e^{-2\pi i\nu \mathbf{s}\cdot\mathbf{b}/c} d\Omega, \tag{3.4}$$

where $\mathbf{s} = \boldsymbol{\rho}/|\boldsymbol{\rho}|$, and the observed intensity, $I_\nu(\mathbf{s})$, is defined as $I_\nu(\mathbf{s}) = \left\langle |\boldsymbol{\mathcal{E}}_\nu(\boldsymbol{\rho})|^2 \right\rangle \rho^2$.

The correlation in Eq. (3.4) requires pointwise voltage measurements, which cannot be achieved by antennas of finite size. The intensity received by a physical antenna is weighted by a function, called the *primary beam*, which has its maximum at the pointing center, $\mathbf{s}_0$, and falls rapidly to zero. For a circular antenna with diameter D, the beam pattern becomes the Airy disk with full width at half maximum (FWHM) [72],

$$FWHM = 1.02\frac{\lambda}{D}. \tag{3.5}$$

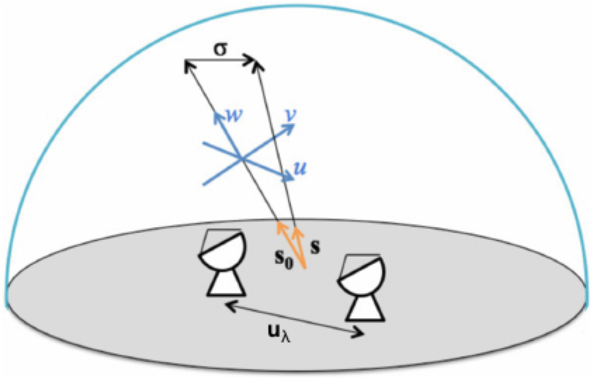

Figure 3.1: Single baseline interferometer with pointing center $\mathbf{s}_0$ and baseline $\mathbf{u}_\lambda = (u, v, w)$ [3].

The interferometer response is obtained by correlating the signal power received from each antenna in bandwidth $\Delta\nu$:

$$c_\lambda(\mathbf{u}_\lambda, \mathbf{s}_0) = \Re\left\{\int_{\nu_0-\Delta\nu/2}^{\nu_0+\Delta\nu/2} e^{-2\pi i \mathbf{s}_0\cdot\mathbf{u}_\lambda} V(\mathbf{u}_\lambda) d\nu\right\}, \tag{3.6}$$

where ν_0 is the observation frequency and $\mathbf{u}_\lambda = \mathbf{b}/\lambda$ is the baseline measured in wavelengths λ. The complex visibility is defined as [72, 74]

$$V(\mathbf{u}_\lambda) = \int A(\boldsymbol{\sigma}) I_\lambda(\boldsymbol{\sigma}) e^{-2\pi i \boldsymbol{\sigma}\cdot\mathbf{u}_\lambda} d\Omega, \tag{3.7}$$

where $\boldsymbol{\sigma} = \mathbf{s} - \mathbf{s}_0$, and the *beam pattern*, $A(\boldsymbol{\sigma})$, is the product of the primary beams of the antennas.

It is convenient to introduce an orthonormal coordinate system $(\mathbf{u}, \mathbf{v}, \mathbf{w})$ with $\mathbf{w}$ lying in the pointing direction $\mathbf{s}_0$ (see Fig. 3.1). In these coordinates, the baseline is written as $\mathbf{u}_\lambda = (u, v, w)$. For an interferometer with coplanar baselines, each baseline traces out an elliptic locus on the baseline plane because of the Earth's rotation. The ensemble of these elliptical loci, which is known as the *interferometer pattern*, represents the data points at which the visibilities are sampled [72, 74].

Polarization measurements can be made by using a pair of orthogonal polarizers, linear or circular, on each antenna. For linear polarizers, a visibility matrix, $\boldsymbol{\mathcal{V}}$, is constructed by correlating the components of the signal received by the antennas j and k:

$$\boldsymbol{\mathcal{V}}(\mathbf{u}) = \begin{pmatrix} \langle \mathbf{E}_{jx}\mathbf{E}^*_{kx} \rangle & \left\langle \mathbf{E}_{jx}\mathbf{E}^*_{ky} \right\rangle \\ \langle \mathbf{E}_{jy}\mathbf{E}^*_{kx} \rangle & \left\langle \mathbf{E}_{jy}\mathbf{E}^*_{ky} \right\rangle \end{pmatrix} = \int A(\boldsymbol{\sigma})\boldsymbol{\mathcal{S}}(\boldsymbol{\sigma})e^{-2\pi i \boldsymbol{\sigma}\cdot\mathbf{u}} d\Omega, \tag{3.8}$$

where $\boldsymbol{\mathcal{S}}$ is the coherence matrix defined in Eq. (2.14).

Circular polarizers measure the *left circular*, $\mathbf{e}_L$, and the *right circular*, $\mathbf{e}_R$, polarization components of the signal, which are related to the linear polarization basis, $\mathbf{e}_x$ and $\mathbf{e}_y$, by a unitary transformation [5]:

$$\begin{pmatrix} \mathbf{e}_R \\ \mathbf{e}_L \end{pmatrix} = \mathbf{T}_{circ} \begin{pmatrix} \mathbf{e}_x \\ \mathbf{e}_y \end{pmatrix} = \frac{1}{\sqrt{2}} \begin{pmatrix} 1 & i \\ 1 & -i \end{pmatrix} \begin{pmatrix} \mathbf{e}_x \\ \mathbf{e}_y \end{pmatrix}. \tag{3.9}$$

In a circular basis, the coherence matrix, $\boldsymbol{\mathcal{S}}$, becomes:

$$\boldsymbol{\mathcal{S}}_{circ} = \mathbf{T}_{circ} \cdot \boldsymbol{\mathcal{S}} \cdot \mathbf{T}^{-1}_{circ}. \tag{3.10}$$

The main goal of the CMB observations is to characterize the temperature anisotropies of the Stokes parameters. Small fluctuations in the total radiation intensity can be converted into temperature fluctuations by differentiating the Planck equation (2.1):

$$\Delta I_\lambda(T) = \frac{dI_\lambda}{dT}\frac{\Delta T}{T_0} = \frac{2(k_B T_0)^3}{(hc)^2}\frac{x^4 e^x}{(e^x - 1)^2}\Delta T, \tag{3.11}$$

where $x = hc/\lambda k_B T_0$. Fluctuations in the polarization intensities can also be converted into temperature fluctuations in a similar fashion. At a given observation wavelength, the temperature visibilities are found by multiplying Eq. (3.8) by a constant factor. From this point on, visibilities should be understood as temperature fluctuation visibilities.

3.1.1 Power Spectra from Visibility Correlations

The visibilities in CMB polarimetry, for which Stokes $V = 0$, can be written in terms of spherical harmonic coefficients of the temperature and the polarization fluctuations:

$$V_T = \int \Delta T A e^{-2\pi i \boldsymbol{\sigma}\cdot\mathbf{u}} d\Omega = \sum_{m,\ell} a_{T,\ell m}\beta_{\ell m}, \tag{3.12a}$$

$$V_Q \pm iV_U = \int \left(\Delta Q \pm i\Delta U\right) A e^{-2\pi i \boldsymbol{\sigma}\cdot\mathbf{u}} d\Omega = \sum_{m,\ell} (a_{E,\ell m} \pm i a_{B,\ell m})\beta_{\pm 2,\ell m}, \tag{3.12b}$$

where

$$\beta_{\ell m} = \int Y_\ell^m(\mathbf{s}) A(\boldsymbol{\sigma}) e^{-2\pi i \boldsymbol{\sigma}\cdot\mathbf{u}} d\Omega, \tag{3.13a}$$

$$\beta_{\pm 2,\ell m} = -\int {}_{\pm 2}Y_\ell^m(\mathbf{s}) A(\boldsymbol{\sigma}) e^{-2\pi i \boldsymbol{\sigma}\cdot\mathbf{u}} d\Omega. \tag{3.13b}$$

Correlations of the visibilities of Eq. (3.12) are related to the angular power spectra, Eq. (2.18), of the CMB fluctuations:

$$\left\langle |V_T|^2 \right\rangle = \sum_\ell C_\ell^{TT} \sum_m |\beta_{\ell m}|^2, \tag{3.14a}$$

$$\left\langle |V_Q|^2 \right\rangle = \sum_\ell C_\ell^{EE} \sum_m \frac{1}{4}|\beta_{+2,\ell m} + \beta_{-2,\ell m}|^2 + \sum_\ell C_\ell^{BB} \sum_m \frac{1}{4}|\beta_{+2,\ell m} - \beta_{-2,\ell m}|^2, \tag{3.14b}$$

$$\left\langle |V_U|^2 \right\rangle = \sum_\ell C_\ell^{BB} \sum_m \frac{1}{4}|\beta_{+2,\ell m} + \beta_{-2,\ell m}|^2 + \sum_\ell C_\ell^{EE} \sum_m \frac{1}{4}|\beta_{+2,\ell m} - \beta_{-2,\ell m}|^2, \tag{3.14c}$$

$$\left\langle V_T V_Q^* \right\rangle = \sum_\ell C_\ell^{TE} \sum_m \frac{1}{2}\beta_{\ell m}(\beta_{+2,\ell m} + \beta_{-2,\ell m})^*. \tag{3.14d}$$

Because of the discrete nature of visibility sampling, these equations are, in fact, singular, and the inversion to obtain power spectra is a highly non-trivial task. We will discuss efficient power spectrum estimation methods in the next chapter.

3.1.2 Flat Sky Approximation

In an interferometric observation, the observed region usually subtends a small angle on the celestial sphere. In such cases, the region can be approximated as a planar patch with $\mathbf{s}\cdot\boldsymbol{\sigma} \approx 0$, and the visibilities given by Eq. (3.8) become convolutions in Fourier space:

$$V_S(\mathbf{u}) = \int \tilde{S}(\mathbf{k}) \tilde{A}(\mathbf{k} - 2\pi\mathbf{u}) d^2\mathbf{k}, \tag{3.15}$$

where $\tilde{f}(\mathbf{k})$ is the Fourier transform of $f(\boldsymbol{\sigma})$, and $S = \Delta T$, ΔQ or ΔU. In a flat sky approximation, the relation between E and B mode polarizations and Stokes Q and U can be expressed in Fourier space:

$$\begin{pmatrix} \tilde{T}(\mathbf{k}) \\ \tilde{Q}(\mathbf{k}) \\ \tilde{U}(\mathbf{k}) \end{pmatrix} = \mathbf{U}_\phi \cdot \begin{pmatrix} \tilde{T}(\mathbf{k}) \\ \tilde{E}(\mathbf{k}) \\ \tilde{B}(\mathbf{k}) \end{pmatrix} = \begin{pmatrix} 1 & 0 & 0 \\ 0 & \cos(2\phi) & -\sin(2\phi) \\ 0 & \sin(2\phi) & \cos(2\phi) \end{pmatrix} \begin{pmatrix} \tilde{T}(\mathbf{k}) \\ \tilde{E}(\mathbf{k}) \\ \tilde{B}(\mathbf{k}) \end{pmatrix}, \tag{3.16}$$

where ϕ is the angle between $\mathbf{k}$ and the x-axis of the uv-plane. Since the beam function $\tilde{A}$ in Eq. (3.15) is centered at $\mathbf{k} = 2\pi\mathbf{u}$ and decays rapidly to zero, the power spectra can be treated as constant in the vicinity of the beam function corresponding to a multipole range $\Delta\ell$ with the center value of $\ell = 2\pi|\mathbf{u}|$. With these assumptions, for a baseline $\mathbf{u}$ pointing in the x-direction, the correlations of Eq. (3.14), normalized by the beam pattern, can be simplified as [29]

$$\left\langle |V_T|^2 \right\rangle = C_b^{TT}, \tag{3.17a}$$

$$\left\langle |V_Q|^2 \right\rangle = C_b^{EE}\overline{c^2} + C_b^{BB}\overline{s^2}, \tag{3.17b}$$

$$\left\langle |V_U|^2 \right\rangle = C_b^{EE}\overline{s^2} + C_b^{BB}\overline{c^2}, \tag{3.17c}$$

$$\left\langle V_T V_Q^* \right\rangle = C_b^{TE}\overline{c}, \tag{3.17d}$$

where $\overline{c^n}$ and $\overline{s^n}$ are normalized averages of $\cos^n(\phi)$ and $\sin^n(\phi)$ over the beam pattern:

$$\overline{s^n} = \frac{\int |\tilde{A^2}(\mathbf{k} - 2\pi\mathbf{u})|^2 \sin^n(\phi) d^2\mathbf{k}}{\int |\tilde{A^2}(\mathbf{k})|^2 d^2\mathbf{k}}, \tag{3.18a}$$

$$\overline{c^n} = \frac{\int |\tilde{A^2}(\mathbf{k} - 2\pi\mathbf{u})|^2 \cos^n(\phi) d^2\mathbf{k}}{\int |\tilde{A^2}(\mathbf{k})|^2 d^2\mathbf{k}}, \tag{3.18b}$$

$\tilde{A^2}$ being the Fourier transform of the beam pattern squared, and $b = \left[2\pi u - \frac{\Delta\ell}{2}, 2\pi u + \frac{\Delta\ell}{2}\right]$ is the spectral band.

3.2 Systematic Effects in Interferometry

For polarimetric observations with low signal-to-noise ratios, such as B mode measurements of the CMB polarization, interferometers offer many advantages over imagers. In an imaging experiment, Stokes parameters are measured by differencing two orthogonally polarized beams. Thus, any mismatch in the beam shapes and positions will induce false polarization signals because of the temperature anisotropy. Interferometers, on the other hand, measure Stokes parameters directly, inherently avoiding such leakage from temperature to polarization signal. Interferometers with horn antennas have extremely low sidelobes and symmetric, nearly Gaussian beam patterns, which eliminates the contamination that plagues imagers having different sidelobe responses for the two polarizations. Moreover, having no reflections from optical surfaces, interferometers with horn antennas do not suffer from cross-polar beam response as severely as imagers.

The systematic effects relevant to interferometric measurements of the CMB polarization can be considered in two categories [5]: *instrument errors* that are introduced within the detectors, and *beam errors* that vary across the sky. We shall discuss two major types of instrument errors, namely *antenna gain* and *antenna coupling* errors. The types of beam errors that we shall consider are *beam shape*, *antenna pointing*, and *beam cross-polarization* errors.

Antenna gain is the increase in power output of the antenna relative to the received signal. Taking arbitrary phases in the errors into account, gain can be represented by a pair of complex factors, g_1 and g_2, one for each orthogonal polarization state. The cross-polar response of a detector to the signal from orthogonal polarization is known as the antenna coupling, which can also be represented by a pair of complex parameters, ϵ_1 and ϵ_2. Instrument errors can be modeled by the *Jones matrix* which multiplies the signal matrix in Eq. (3.8). The Jones matrix, $\mathbf{J}_k$, of the k^{th} antenna is given by

$$\mathbf{J}_k = \begin{pmatrix} 1+g_1^k & \epsilon_1^k \\ \epsilon_2^k & 1+g_2^k \end{pmatrix}, \tag{3.19}$$

where g_1^k and g_2^k are the *gain* parameters, and ϵ_1^k and ϵ_2^k are the *coupling* parameters of the k^{th} antenna.

The difference between the beam center of an antenna and the pointing center that is intended to be observed is known as the pointing error and represented by the vector $\boldsymbol{\delta}^k$. Beam shape error is defined as the departure of an antenna's primary beam from the ideal circular Gaussian beam pattern. Together with the pointing error, shape error can be modeled by an elliptic Gaussian function:

$$A^k(\boldsymbol{\sigma}, \boldsymbol{\delta}^k, \boldsymbol{\zeta}^k, \psi_k) = \exp\left\{-\frac{((\sigma_x - \delta_x^k)\cos\psi_k + (\sigma_y - \delta_y^k)\sin\psi_k)^2}{2a^2(1+\zeta_1^k)^2}\right\} \times \exp\left\{-\frac{((\sigma_y - \delta_y^k)\cos\psi_k - (\sigma_x - \delta_x^k)\sin\psi_k)^2}{2a^2(1+\zeta_2^k)^2}\right\}, \tag{3.20}$$

where a is the radius of the ideal beam, ζ_1^k and ζ_2^k measure the deviations of the axes of the elliptic beam from the ideal circular beam, and ψ_k is the angle between the major axis of the ellipse and the x-axis on the sky. Note that ζ_1^k and ζ_2^k incorporate beam size errors, as well.

Beam cross-polarization, which is defined as any type of cross-polar antenna response that has a beam pattern on the sky, can be described by a beam matrix $\mathbf{B}_k$. Reflection symmetry requires that $\mathbf{B}_k$ must be diagonal along the x-axis since any coupling between orthogonal polarization signals would change sign upon reflection [5]. For an arbitrary direction, the beam matrix can be found by a rotation of this diagonal matrix [5]:

$$\mathbf{B}_k = A^k(\boldsymbol{\sigma}, \boldsymbol{\delta}^k, \boldsymbol{\zeta}^k, \psi_k)\begin{pmatrix} 1 + \frac{1}{2}\alpha_k(r)\cos 2\theta & \frac{1}{2}\alpha_k(r)\sin 2\theta \\ \frac{1}{2}\alpha_k(r)\sin 2\theta & 1 - \frac{1}{2}\alpha_k(r)\cos 2\theta \end{pmatrix}, \tag{3.21}$$

where $\boldsymbol{\sigma} = (r, \theta)$ is written in polar coordinates. The cross-polar response $\alpha_k(r)$ is expected to be small near the beam center and can be modeled as

$$\alpha(r) = \mu_k \frac{r^2}{a^2}. \tag{3.22}$$

This particular form of the cross-polarization occurs, with $\mu_k = a^2/2$, when the curved sky patch is projected onto the plane [5], however, this effect is known and can be corrected. The cross-polarization parameter μ_k represents any residual systematics that is not accounted for.

The systematic errors can be modeled by writing the visibility matrix for the antenna pair j and k as

$$\boldsymbol{\mathcal{V}}_{jk} = \int \boldsymbol{\mathcal{A}}_k \cdot \mathbf{H} \cdot \boldsymbol{\mathcal{S}} \cdot \mathbf{H}^{-1} \boldsymbol{\mathcal{A}}_j^{\dagger} e^{-2\pi i \boldsymbol{\sigma}\cdot\mathbf{u}_{jk}} d\Omega, \tag{3.23}$$

where $\boldsymbol{\mathcal{A}}_k = \mathbf{J}_k \cdot \mathbf{H} \cdot \mathbf{B}_k \cdot \mathbf{H}^{-1}$ is the *antenna pattern* of the k^{th} antenna. For linear polarizers $\mathbf{H}$ is the identity matrix, $\mathbf{I}$, for circular polarizers $\mathbf{H} = \mathbf{T}_{circ}$ of Eq. (3.9).

3.2.1 Biases in Power Spectra Induced by Systematics

The systematic effects on the power spectra can be described by the root-mean-square difference between the observed spectrum, C^{XY}_{actual}, which is recovered from the data of an experiment with systematic errors, and the ideal spectrum, C^{XY}_{ideal}, which would have been recovered from the data of an experiment with no systematic errors;

$$\Delta C^{XY}_{rms} = \left\langle \left(C^{XY}_{actual} - C^{XY}_{ideal} \right)^2 \right\rangle^{1/2}, \tag{3.24}$$

where $X, Y = \{T, E, B\}$. Although the power spectra C^{TB} and C^{EB} vanish because of the odd parity of the B modes, systematics may still induce biases for them. It is, therefore, reasonable to include two more terms to Eq. (3.17) [29]:

$$\langle V_T V_U^* \rangle = C^{TB}_{\ell=2\pi u} \overline{c}, \tag{3.25a}$$

$$\langle V_Q V_U^* \rangle = C^{EB}_{\ell=2\pi u} (\overline{c^2} - \overline{s^2}), \tag{3.25b}$$

for a baseline in x direction. The unbiased estimator for $C^{XY} = \left\langle \hat{C}^{XY} \right\rangle$ is obtained as

$$\hat{C}^{XY} = \mathbf{v}^\dagger \cdot \mathbf{N}_{XY} \cdot \mathbf{v}, \tag{3.26}$$

where $\mathbf{v} = (V_T, V_Q, V_U)$ is the vector of ideal visibilities with covariance $\mathbf{M} = \langle \mathbf{v}\mathbf{v}^\dagger \rangle$. The explicit forms of the 3×3 matrices, $\mathbf{N}_{XY}$, involving $\overline{s^2}$, $\overline{c^2}$ and $\overline{c}$ are given Appendix A.

Systematic effects on the visibilities can be described, to first order, by $\mathbf{v}_{actual} = \mathbf{v} + \delta\mathbf{v}$, which, according to Eq. (3.26), gives

$$\Delta\hat{C}^{XY} = \mathbf{v}^\dagger \cdot \mathbf{N}_{XY} \cdot \delta\mathbf{v} + \delta\mathbf{v}^\dagger \cdot \mathbf{N}_{XY} \cdot \mathbf{v}. \tag{3.27}$$

Combining $\mathbf{v}$ and $\delta\mathbf{v}$ into a 6-dimensional vector $\mathbf{w} = (\mathbf{v}, \delta\mathbf{v})$, we can write the first order approximation as [5]

$$\Delta\hat{C}^{XY} = \mathbf{w}^\dagger \cdot \boldsymbol{\mathcal{N}}_{XY} \cdot \mathbf{w} = \mathbf{w}^\dagger \begin{pmatrix} 0 & \mathbf{N}_{XY} \\ \mathbf{N}_{XY} & 0 \end{pmatrix} \mathbf{w}, \tag{3.28}$$

where the covariance matrix of the vector $\mathbf{w}$ is defined as

$$\boldsymbol{\mathcal{M}}_w = \left\langle \mathbf{w} \cdot \mathbf{w}^{\dagger} \right\rangle . \tag{3.29}$$

In order to find the mean squared value of $\Delta\hat{C}^{XY}$, first we Cholesky decompose $\boldsymbol{\mathcal{M}}_w = \mathbf{U} \cdot \mathbf{U}^{\dagger}$, and perform a similarity transformation $\boldsymbol{\mathcal{N}'}_{XY} = \mathbf{U}^{\dagger} \cdot \boldsymbol{\mathcal{N}}_{XY} \cdot \mathbf{U}$ [5]. Then we can write $\Delta C^{XY} = \mathbf{w}'^{\dagger} \cdot \boldsymbol{\mathcal{N}'}_{XY} \cdot \mathbf{w}'$, where $\mathbf{w}' = \mathbf{U}^{-1}\mathbf{w}$ and $\left\langle \mathbf{w}'\mathbf{w}'^{\dagger} \right\rangle = \mathbf{I}$. Diagonalizing $\boldsymbol{\mathcal{N}'}_{XY} = \mathbf{P}^{\dagger} \cdot \boldsymbol{\Lambda} \cdot \mathbf{P}$, we have

$$\Delta\hat{C}^{XY} = \mathbf{m}^{\dagger} \cdot \boldsymbol{\Lambda} \cdot \mathbf{m} = \sum_i \lambda_i |m_i|^2, \tag{3.30}$$

where $\mathbf{m} = \mathbf{P} \cdot \mathbf{w}'$ and m_i are complex Gaussian univariate variables with zero mean, so $\left\langle |m_i|^2 |m_j|^2 \right\rangle = 1 + \delta_{ij}$. Therefore,

$$\begin{aligned} \left\langle \left(\Delta\hat{C}^{XY}\right)^2 \right\rangle &= \sum_{i,j} \lambda_i \lambda_j \left\langle |m_i|^2 |m_j|^2 \right\rangle \\ &= \left(\sum_i \lambda_i \right)^2 + \sum_i \lambda_i^2 \\ &= \left(Tr\left[\boldsymbol{\Lambda}\right]\right)^2 + Tr\left[(\boldsymbol{\Lambda})^2\right] . \end{aligned} \tag{3.31}$$

Since $Tr[\boldsymbol{\Lambda}^n] = Tr[(\boldsymbol{\mathcal{N}'}_{XY})^n] = Tr[(\boldsymbol{\mathcal{N}}_{XY} \cdot \boldsymbol{\mathcal{M}}_w)^n]$, we can write

$$\left(\Delta C^{XY}_{rms}\right)^2 = \left(Tr\left[\boldsymbol{\mathcal{N}}_{XY} \cdot \boldsymbol{\mathcal{M}}_w\right]\right)^2 + Tr\left[(\boldsymbol{\mathcal{N}}_{XY} \cdot \boldsymbol{\mathcal{M}}_w)^2\right] . \tag{3.32}$$

For a baseline pointing in an arbitrary direction, the analysis is done in a rotated coordinate system:

$$\mathbf{v}_{rot} = \mathbf{R} \cdot \mathbf{v} = \begin{pmatrix} 1 & 0 & 0 \\ 0 & \cos 2\eta & \sin 2\eta \\ 0 & -\sin 2\eta & \cos 2\eta \end{pmatrix} \mathbf{v}, \tag{3.33}$$

η being the angle between $\mathbf{u}$ and the x-axis, where the matrices $\mathbf{M}$ and $\mathbf{N}_{XY}$ must be transformed as $\mathbf{M} \to \mathbf{R}^{-1} \cdot \mathbf{M} \cdot \mathbf{R}$ and $\mathbf{N}_{XY} \to \mathbf{R}^{-1} \cdot \mathbf{N}_{XY} \cdot \mathbf{R}$. The resulting expression in Eq. (3.32) will, then, be averaged over η.

The root-mean-squared bias on a particular band power is, then, given as an expansion in terms of ideal power spectra C_b^{XY}:

$$(\Delta \hat{C}_{rms,b}^{XY})^2 = p_{rms}^2 \sum_{I,J} \kappa_{XY,I,J}^2 C_b^I C_b^J \tag{3.34}$$

where p is the parameter that characterizes the error, such as gain g, coupling ϵ, or cross-polarization μ, and $I, J = \{TT, TE, EE, BB\}$. This expression is valid for a single baseline. For a system with n_b baselines in band b, $\Delta \hat{C}_{rms,b}^{XY}$ must be normalized by $1/\sqrt{n_b}$, assuming there is no correlation between error parameters of different baselines. Analytical estimations of the coefficients $\kappa_{XY,I,J}^2$ for various systematic errors are presented in the Appendix A.

The strength of the systematic effects can be quantified by a tolerance parameter α^{XY} defined by [53, 49]

$$\alpha^{XY} = \frac{\Delta C^{XY}}{\sigma_{stat}^{XY}}, \tag{3.35}$$

where σ_{stat}^{XY} is the statistical 1-σ error in XY-spectrum of the ideal experiment with no systematic errors.

The main interest in a B-mode experiment is the tensor-to-scalar ratio r which can be estimated as [53]

$$r = \frac{\sum_b \partial_r C_b^{BB} (C_b^{BB} - C_{b,lens}^{BB})/(\sigma_{b,stat}^{BB})^2}{\sum_b (\partial_r C_b^{BB}/\sigma_{b,stat}^{BB})^2}, \tag{3.36}$$

where b denotes the power band, $C_{b,lens}^{BB}$ is the B-mode spectrum due to weak gravitational lensing, and C_b^{BB} depends linearly on r through the amplitude of the primordial B-modes. The tolerance parameter of r is given by $\alpha_r = \Delta r/\sigma_r$, where [53]

$$\Delta r = \frac{\sum_b \alpha_b^{BB} (\partial_r C_b^{BB}/\sigma_{b,stat}^{BB})}{\sum_b (\partial_r C_b^{BB}/\sigma_{b,stat}^{BB})^2}, \tag{3.37a}$$

$$\sigma_r = \left(\sum_b (\partial_r C_b^{BB}/\sigma_{b,stat}^{BB})^2 \right)^{-1/2}. \tag{3.37b}$$

For good control of systematics, the value of α_r is required to stay below a determined tolerance limit.

Chapter 4

Analysis Methods for the Visibility Data

The visibility data from an interferometric observation of a polarized signal can be modeled by pixellating the uv-plane and writing the data as a $3n_p$ dimensional vector of visibilities given by the linear equation:

$$\mathbf{d} = \boldsymbol{\mathcal{I}} \cdot (\mathbf{B} \cdot \mathbf{s} + \mathbf{n}), \tag{4.1}$$

where n_p is the number of pixels, $\mathbf{s}$ is a vector of signal harmonic coefficients $(a^T_{\ell m}, a^E_{\ell m} a^B_{\ell m})$ for each ℓ and m, $\mathbf{B}$ is a linear operator that involves with the beam harmonic coefficients given by Eq. (3.13), and $\mathbf{n}$ is the Gaussian random instrumental noise. The noise covariance for baselines $\mathbf{u}_j$ and $\mathbf{u}_k$ can be modeled as [79]

$$\mathbf{N}_{kj} = \left\langle (\boldsymbol{\mathcal{I}} \cdot \mathbf{n})(\boldsymbol{\mathcal{I}} \cdot \mathbf{n})^\dagger \right\rangle_{jk} = \left(\frac{\lambda^2 T_{sys}}{\eta^A A_D} \right)^2 \left(\frac{1}{\Delta_\nu t \overline{n}} \right) \mathcal{I}_j \mathcal{I}_k \delta_{jk}, \tag{4.2}$$

where T_{sys} is the system temperature, λ is the observation wavelength, η^A is the aperture efficiency, A_D is the antenna area, Δ_ν is the bandwidth, $\overline{n}$ is the number of baselines with the same baseline vector, and t is the observation time. The interferometer pattern, $\boldsymbol{\mathcal{I}}$, is a diagonal matrix with elements taking the value of 1 at points where visibilities are sampled and 0 everywhere else.

There are two dominant approaches to statistical inference from visibility data given in Eq. (4.1): the frequentist approach, which focuses on the probability of obtaining the data for a given hypothesis, and the Bayesian approach, which explores the probability of a hypothesis given the data. In this chapter we shall first present a frequentist method, called the maximum likelihood method, for power spectra inference from the visibilities. Then we will introduce the method of Gibbs sampling, a Bayesian method of simultaneous inferences of power spectra and signal maps.

4.1 Maximum Likelihood Method

Maximum likelihood (ML) method treats the data set as one realization of a probabilistic process with a known statistical model for power spectrum distribution. The method provides estimates for the parameters of the model as the set of values that maximize the *likelihood function*, $\mathcal{L}(C_\ell)$, which is given by the distribution $P(\mathbf{d}|C_\ell)$.

For computational efficiency, the total ℓ-range can be divided into N_b spectral bands of equal bin-width, $\Delta\ell$, in which $\ell(\ell+1)C_\ell$ is approximately constant, $\ell(\ell+1)C_\ell \approx \ell_b(\ell_b+1)C_b$. Furthermore, since the maximum likelihood method does not recover the observed signal, the data vector can be reduced to a $3n_d$ dimensional vector $\mathbf{d}_V$, n_d being the total number of visibility samples, by taking only the sampled points [82, 29].

In an ideal experiment, the visibilities would be Gaussian random variables since both the anisotropies in the observed CMB sky and the instrumental noise are assumed to have Gaussian distributions with zero means. Although imperfections, such as incomplete uv-coverage, finite beam size, and pixelation, slightly spoil the Gaussianity, the likelihood of obtaining the data may still be assumed to be Gaussian with zero mean [22]:

$$\mathcal{L}(C_b) = P(\mathbf{d}_V|C_b) = \frac{1}{(2\pi)^{n_d/2}|\mathbf{C}_V+\mathbf{N}|^{1/2}} \exp\left\{-\frac{1}{2}\mathbf{d}_V^\dagger(\mathbf{C}_V+\mathbf{N})^{-1}\mathbf{d}_V\right\}, \tag{4.3}$$

where $\mathbf{C}_V = \left\langle \mathbf{V}\mathbf{V}^\dagger \right\rangle$ is the visibility covariance.

Evaluation of the likelihood function requires the determinant, $|\mathbf{\Sigma}|$, of the covariance matrix $\mathbf{\Sigma} = \mathbf{C}_V + \mathbf{N}$ and calculation of the quadratic form $\mathbf{d}_V^\dagger\mathbf{\Sigma}^{-1}\mathbf{d}_V$. The quadratic form can be evaluated by solving

$$\mathbf{\Sigma}\cdot\mathbf{x} = \mathbf{d}_V, \tag{4.4}$$

with a preconditioned conjugate-gradient technique [22]. A computationally efficient choice for the preconditioner is the sparse incomplete Cholesky decomposition:

$$\mathbf{P} = \mathbf{L} \cdot \mathbf{D} \cdot \mathbf{L}^{\dagger}, \tag{4.5}$$

where $\mathbf{L}$ is lower triangular with unit diagonals, and $\mathbf{D}$ is diagonal. Since the preconditioner $\mathbf{P}$ gives an approximation to the covariance, the determinant can be estimated as

$$|\mathbf{\Sigma}| \approx |\mathbf{P}| = |\mathbf{L}||\mathbf{D}||\mathbf{L}^{\dagger}| = |\mathbf{D}|. \tag{4.6}$$

Maximization of the likelihood function can efficiently be achieved by *Powell's directional set* algorithm, which maximizes iteratively by only function calls. Each spectral bin is represented as an independent direction. At each iteration, a new set of directions is determined and the function is maximized along each direction. Independent direction-maximization is performed for each band-power parameter in turn, while fixing the others. Typically, this process requires order $\mathcal{O}(n_d^2)$ iterations to achieve the maximum-likelihood solution. Although it is a very efficient maximization method, the major drawback is that it does not produce confidence intervals. The statistical errors can be estimated by the Taylor expansion of the likelihood around its maximum, $\overline{\mathbf{C}}_{\{b\}}$ [22]:

$$\delta(\ln \mathcal{L}(\mathbf{C}_{\{b\}})) = \frac{1}{2}\delta\mathbf{C}^{\dagger}_{\{b\}} \cdot \mathbf{H}(\overline{\mathbf{C}}_{\{b\}}) \cdot \delta\mathbf{C}_{\{b\}}, \tag{4.7}$$

where $\mathbf{H}_{ij} = \frac{\partial^2 \ln \mathcal{L}}{\partial C_i \partial C_j}$ is the *Hessian*, and $\mathbf{C}_{\{b\}}$ is the n_b dimensional vector of band powers C_b. The variance of statistical errors is given by the quadratic form (4.7) in the Gaussian distribution:

$$\left\langle (\delta C_i)^2 \right\rangle = -\left(\mathbf{H}^{-1}\right)_{ii}. \tag{4.8}$$

In general, evaluation of the Hessian requires $\mathcal{O}(n_d^3)$ operations for each element.

4.2 Method of Gibbs Sampling

Bayesian approach investigates the distribution of possible spectra for a given data set, which is given by the posterior $P(C_\ell|\mathbf{d})$. The relation to the maximum likelihood method can be shown by applying Bayes' theorem to the posterior

$$P(C_\ell|\mathbf{d}) \propto \mathcal{L}(\mathbf{d}|C_\ell)P(C_\ell), \tag{4.9}$$

where the *prior* $P(C_\ell)$ is the a priori distribution of the spectra. Traditionally, the posterior is obtained by marginalizing the *joint posterior* density:

$$P(C_\ell|\mathbf{d}) = \int d\mathbf{s} P(C_\ell, \mathbf{s}|\mathbf{d}), \tag{4.10}$$

where $\mathbf{s}$ is the signal vector of Eq. (4.1). It is possible to evaluate the marginalization integral by assuming Gaussianity, however, computational complexity of the problem makes it unfeasible, especially for high resolution data.

Instead of marginalizing the joint posterior, a computationally efficient algorithm can be developed for obtaining samples from $P(C_\ell, \mathbf{s}|\mathbf{d})$ by employing the *Gibbs sampling* method. Gibbs sampling is a Markov chain Monte Carlo process that generates simultaneous samples of signal $\mathbf{s}$ and spectra C_ℓ from the joint distribution by an iterative fashion [76, 25].

In interferometric observations of the CMB polarization, the signal covariance $\mathbf{S} = \left\langle \mathbf{s} \cdot \mathbf{s}^\dagger \right\rangle$ becomes a block diagonal matrix with a 3×3 submatrix $\mathbf{C}_i$ at each pixel i [38]:

$$\mathbf{C}_i = \begin{pmatrix} C_{\ell_i}^{TT} & C_{\ell_i}^{TE} & C_{\ell_i}^{TB} \\ C_{\ell_i}^{TE} & C_{\ell_i}^{EE} & C_{\ell_i}^{EB} \\ C_{\ell_i}^{TB} & C_{\ell_i}^{EB} & C_{\ell_i}^{BB} \end{pmatrix}. \tag{4.11}$$

The Gibbs sampling method obtains samples, $\mathbf{s}$ and $\mathbf{S}$, from the joint density $P(\mathbf{S}, \mathbf{s}|\mathbf{d})$ by successively sampling from the conditional distributions $P(\mathbf{s}|\mathbf{S}, \mathbf{d})$ and $P(\mathbf{S}|\mathbf{s}, \mathbf{d}) \propto P(\mathbf{S}|\mathbf{s})$. Starting from an initial guess $\mathbf{S}^0$, the sampling is done iteratively [38]:

$$\mathbf{s}^{a+1} \leftarrow P(\mathbf{s} \mid \mathbf{S}^a,\ \mathbf{d}), \tag{4.12a}$$

$$\mathbf{S}^{a+1} \leftarrow P(\mathbf{S} \mid \mathbf{s}^{a+1}). \tag{4.12b}$$

After a "burn-in" phase, the stationary distribution of the Markov chain is reached and the samples approximate to being samples from the sought-after joint distribution.

For mathematical simplicity, it is instructive to introduce *de-convolved* map, $\mathbf{m} = \mathbf{s} + \mathbf{n}_r$, through $\mathbf{d} = \boldsymbol{\mathcal{I}} \cdot \mathbf{B} \cdot \mathbf{m}$, where $\mathbf{n}_r$ is the residual noise with covariance

$$\mathbf{N}_r = \left\langle \mathbf{n}_r \cdot \mathbf{n}_r^\dagger \right\rangle = \left(\mathbf{B}^\dagger \cdot \mathbf{N}^{-1} \cdot \mathbf{B} \right)^{-1}, \tag{4.13}$$

where we have used $\boldsymbol{\mathcal{I}}^2 = \boldsymbol{\mathcal{I}}$, and the inverses should be understood as pseudo-inverses. Since the noise is Gaussian with zero mean, so is the residual noise. The conditional signal distribution of Eq. (4.12a) can be found by using the Bayes' theorem:

$$P(\mathbf{s}|\mathbf{S}, \mathbf{m}) \propto P(\mathbf{m}|\mathbf{s}, \mathbf{S}) P(\mathbf{s}|\mathbf{S}), \tag{4.14}$$

which can be written as [15]

$$\begin{aligned} P(\mathbf{m}|\mathbf{s}, \mathbf{S}) P(\mathbf{s}|\mathbf{S}) &= \exp\left\{ -\frac{1}{2} (\mathbf{m} - \mathbf{s})^\dagger \mathbf{N}_r^{-1} (\mathbf{m} - \mathbf{s}) \right\} \exp\left\{ -\frac{1}{2} \mathbf{s}^\dagger \mathbf{S}^{-1} \mathbf{s} \right\} \\ &\propto \exp\left\{ -\frac{1}{2} (\mathbf{s} - \bar{\mathbf{s}})^\dagger (\mathbf{S}^{-1} + \mathbf{N}_r^{-1}) (\mathbf{s} - \bar{\mathbf{s}}) \right\}, \end{aligned} \tag{4.15}$$

where we have defined the *Wiener filtered* mean signal

$$\bar{\mathbf{s}} = \left(\mathbf{S}^{-1} + \mathbf{N}_r^{-1} \right)^{-1} \mathbf{N}_r^{-1} \mathbf{m}. \tag{4.16}$$

Sampling from the Gaussian (4.15) is achieved adding a fluctuation field $\boldsymbol{\xi}$, a zero-mean Gaussian field with covariance $\langle \boldsymbol{\xi} \cdot \boldsymbol{\xi}^\dagger \rangle = \left(\mathbf{S}^{-1} + \mathbf{N}_r^{-1} \right)^{-1}$, to the mean field signal $\bar{\mathbf{s}}$. Because of the computational difficulty of calculating the inverse matrix $\left(\mathbf{S}^{-1} + \mathbf{N}_r^{-1} \right)^{-1}$, we define the transformed field $\boldsymbol{\chi} = \left(\mathbf{S}^{-1} + \mathbf{N}_r^{-1} \right) \boldsymbol{\xi}$ [25]:

$$\left\langle \boldsymbol{\chi} \cdot \boldsymbol{\chi}^\dagger \right\rangle = \left(\mathbf{S}^{-1} + \mathbf{N}_r^{-1} \right) \left\langle \boldsymbol{\xi} \cdot \boldsymbol{\xi}^\dagger \right\rangle \left(\mathbf{S}^{-1} + \mathbf{N}_r^{-1} \right) = \left(\mathbf{S}^{-1} + \mathbf{N}_r^{-1} \right). \tag{4.17}$$

Samples for the transformed Gaussian field is obtained by drawing two independent Gaussian zero-mean univariate fields $\boldsymbol{\omega}_1$ and $\boldsymbol{\omega}_2$:

$$\boldsymbol{\chi} = \mathbf{S}^{-1/2} \boldsymbol{\omega}_1 + \mathbf{P}^\dagger \boldsymbol{\omega}_2, \tag{4.18}$$

where $\mathbf{P}^\dagger \mathbf{P} = \mathbf{N}_r^{-1} = \mathbf{B}^\dagger \mathbf{N}^{-1} \mathbf{B}$ from Eq. (4.13). An obvious choice for $\mathbf{P}$ is, therefore, $\mathbf{P} = \mathbf{N}^{-1/2} \mathbf{B}$. The sampled signal can be written as $\mathbf{s} = \bar{\mathbf{s}} + \boldsymbol{\xi}$. Since $\mathbf{N}_r^{-1} \mathbf{m} = \mathbf{B}^\dagger \mathbf{N}^{-1} \mathbf{d}$, after rearranging Eq. (4.16), we reach the signal sampling equation:

$$\left(\mathbf{S}^{-1} + \mathbf{B}^{\dagger}\mathbf{N}^{-1}\mathbf{B}\right)\mathbf{s} = \mathbf{B}^{\dagger}\mathbf{N}^{-1}\mathbf{d} + \mathbf{S}^{-1/2}\boldsymbol{\omega}_1 + \mathbf{B}^{\dagger}\mathbf{N}^{-1/2}\boldsymbol{\omega}_2. \tag{4.19}$$

Solution of the linear system (4.19) is the most computationally expensive step of the Gibbs sampler. The computational complexity can be reduced by employing the *preconditioned conjugate gradients* technique. A good choice for the preconditioner is the inverse of the operator on the left hand side of Eq. (4.19), which can be computed in $\mathcal{O}(n_p^{3/2})$ operations [76]. In spherical harmonic basis, action of the powers of $\mathbf{S}$ on vectors scales as $\mathcal{O}(n_p^2)$ [76]. Complexity is significantly reduced in flat sky approximation where the spherical harmonic transforms replaced by FFTs, which scale as $\mathcal{O}(n_p \log n_p)$.

To sample the power spectra, the last sampled signal $\mathbf{s}$ is used as an the input for the posterior $P(\mathbf{S}|\mathbf{s})$. In Bayesian statistics, if an uninformative prior, such as *Jeffrey's prior*, is used, the marginal posterior distribution for the unknown covariance matrix of a multivariate Gaussian process is given by the *inverse Wishart* distribution $\mathcal{W}(\mathbf{S}, f)$ with f degrees of freedom:

$$P(\mathbf{S}|\mathbf{s}) = \mathcal{W}(\mathbf{S}, f) \propto \prod_{\ell} \frac{1}{\sqrt{|\mathbf{C}_\ell|^{2\ell+1+2q}}} \exp\left(-\frac{1}{2} Tr\{\boldsymbol{\sigma}_\ell \cdot \mathbf{C}_\ell^{-1}\}\right), \tag{4.20}$$

where we have defined

$$\boldsymbol{\sigma}_\ell = \sum_{m=-\ell}^{m=\ell} \mathbf{s}_{\ell m}\mathbf{s}_{\ell m}^{\dagger} \tag{4.21}$$

with the three-vector $\mathbf{s}_{\ell m} = (a_{\ell m}^T, a_{\ell m}^E, a_{\ell m}^B)$. The uninformative prior is chosen to be $P(\mathbf{S}) \propto \prod_\ell |\mathbf{C}_\ell|^{-q}$, where $q = 0$ for a uniform prior, and $q = 1$ for a Jeffrey's prior [76].

To improve sampling efficiency we can define uniform bins, with width $\Delta\ell$, in which $\ell(\ell+1)C_\ell$ is nearly flat. Then $\boldsymbol{\sigma}_\ell$ is defined for bin b as [76]

$$\boldsymbol{\sigma}_b = \sum_{\ell\in b} \sum_{m=-\ell}^{m=\ell} \ell(\ell+1)\mathbf{s}_{\ell m}\mathbf{s}_{\ell m}^{\dagger} \tag{4.22}$$

Sampling from the inverse Wishart distribution $\mathcal{W}(\mathbf{S}, f_b)$ can be done by drawing $f_b = L_b - 4 + 2q$ vectors, L_b being the number of monopoles in the bin b, from a Gaussian distribution with covariance matrix $\boldsymbol{\sigma}_b^{-1}$. The sample $\mathbf{C}_b$ is, then, given by the inverse of the sum of outer products of these independently sampled vectors [76]. The actual power spectrum coefficients are given by $\mathbf{C}_\ell = \mathbf{C}_b/\ell(\ell+1)$.

A powerful statistical tool, known as Gelman-Rubin (G-R) convergence diagnostic [20], can be employed to determine that the stationary distribution of the Markov chain has been reached. Given multiple instances of chains, convergence is reached when the *potential scale reduction factor*, $\mathcal{R}$, of the G-R statistic, determined by the ratio of the variance within each chain to the variance among chains, assumes a value less than a given tolerance (usually chosen to be 1.1) for each bin. A more detailed discussion on G-R convergence diagnostic is given in Appendix B.

Chapter 5

Simulated Observations

In Section 3.2 we have presented analytical estimations for various systematic effects on interferometers measurements of the CMB power spectrum. This approach is of course only a first-order approximation for assessing systematics, since many important effects, such as the configuration of the array, instrumental noise, the sampling variance due to the finite beam size, and incomplete *uv*-coverage, are not taken into account. Any actual experiment, therefore, will naturally require realistic simulations to examine how systematic effects bias the power spectrum and, more importantly, tensor-to-scalar ratio inferences. In this chapter, we shall first present simulated observations of the CMB polarization signal by an ideal interferometer design and apply the analysis techniques discussed in the previous chapter to obtain power spectra and signal inferences. Then we will introduce various systematic errors in our interferometer design and present a complete pipeline of simulations to assess the control levels for each systematic error.

The interferometer configuration is a close-packed square array of 400 antennas with diameters of 7.89λ. The observation frequency is 150 GHz with a 10-GHz bandwidth. This configuration is similar to the QUBIC design [63]. With this frequency and antenna radius, the minimum available multipole is $\ell_{min} = 28$. The baselines are uniformly rotated in the *uv*-plane over a period of 12 hours while observing the same sky patch. The interferometer pattern, $\boldsymbol{\mathcal{I}}$, is constructed by placing a value of one at each pixel that coincides with a baseline length during the observation period and zeros everywhere else. The antenna

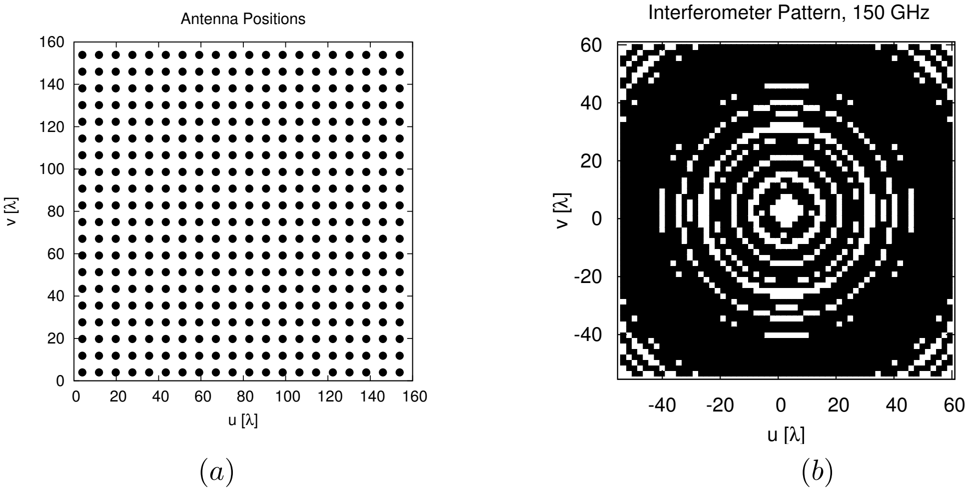

(*a*) (*b*)

Figure 5.1: Positions of 20 × 20 close-packed array of antennas of radius 7.89λ (a), and the interferometer pattern created over an observation period of 12 hours (b) [29].

positions and the resulting interferometer pattern is shown in Fig. 5.1.

Beam pattern of horn antennas with diameters of 7.89λ can be modeled as a Gaussian with peak value of unity and $FWHM \approx 12^\circ$. With such a wide field of view, the flat-sky approximation is clearly not valid. The observed sky should be simulated as a spherical cap, and the visibilities must be constructed and analyzed in spherical harmonic basis. Since we are not dealing with data from an actual observation, for the purpose of analyzing the systematics, a computationally much less demanding, yet approximately equivalent, set up may be simulated. Constructing the signal on a flat patch and working in Fourier space would not significantly alter the effects of systematic errors. Any residual systematic error that we want to investigate will induce approximately the same effect in both spherical and flat sky simulations.

Another crucial point is that the polarization signal cannot be uniquely decomposed into E and B parts on a cut sky. The non-uniqueness of the decomposition causes leakage from the E mode into the much weaker B mode power spectrum [42]. Therefore, in dealing with actual data from an observation with finite field of view, E and B modes must be separated from each other. Since we want to analyze the systematic effects after the E-B separation is achieved, we can by-pass the mode mixing problem by constructing the input signal maps on a flat sky patch with periodic boundary conditions. Because the E-B decomposition is unique in this domain, the so-called E-B coupling problem does not arise. A short discussion about E-B mode mixing is presented in Appendix C.

The input T, Q and U maps are constructed over 30-degree square patches with 64 pixels per side. The size of the patch is chosen in such a way that the ideal beam pattern drops to the value of 10^{-4} at the edges of the patch, reducing the edge-effects caused by the periodic boundary conditions of the fast Fourier transformations. The signal realizations are generated as maps of Gaussian fluctuations with a covariance $\mathbf{C}_i$ of Eq. (4.11) at each pixel whose components are computed by CAMB [7] using the cosmological parameters that are consistent with the 7-year results of *WMAP* [37, 34]; $\Omega_M = 0.27$, $\Omega_\Lambda = 0.73$, $\Omega_b = 0.045$, and $H_0 = 70$ km s^{-1} Mpc^{-1}. The tensor-to-scalar ratio is taken to be $r = 0.01$. The angular resolution of the signal maps is 28 arcminutes, corresponding to a maximum available multipole of $\ell_{max} = 384$.

Measuring the Stokes Q visibilities in an experiment with linear polarizers requires perfect cancellation of the much stronger temperature signal from the visibility matrix of Eq. (2.14), which is unfeasible. Instead, in a linear experiment, the Stokes Q visibilities are obtained by measuring the Stokes U visibilities with 45° rotated polarizers since under a 45° rotation $U \to -Q$. However, measuring V_Q and V_U from different observations decreases the sensitivity. The problem does not arise in an experiment with circular polarizer where the cancellations required for V_U measurements are not problematic since $Q \sim U$. Hence, in a circular experiment, V_Q and V_U are measured simultaneously from the same observation without sacrificing the sensitivity.

The noise at each pixel for the temperature data is simulated according to the total observation time that all baselines spend in the pixel. The noise covariance for each baseline is given by Eq. (4.2). The noise value is normalized by a constant to have an rms noise level of $0.015\mu K$ per visibility.

By adopting the flat-sky approximation the visibility covariances for maximum likelihood method can be written as

$$C_{SS'}^{ij} = \langle V_S(\mathbf{u}_i) V_{S'}^*(\mathbf{u}_j) \rangle = \sum_{b=1}^{N_b} \sum_{X,Y} C_b^{XY} \int_{u_b - \Delta\ell/2}^{u_b + \Delta\ell/2} \frac{1}{2\pi} \frac{dw}{w} \times W_{SS'XY}^{i,j}(w). \tag{5.1}$$

The *window functions* $W_{SS'XY}^{ij}$ are given by

$$W_{SS'XY}^{ij}(|\mathbf{w}|) = \int_0^{2\pi} d\phi_{\mathbf{w}} \, \omega_{SX} \omega_{S'Y} \tilde{A}(\mathbf{u}_i - \mathbf{w}) \tilde{A}^*(\mathbf{u}_j - \mathbf{w}) \,, \tag{5.2}$$

where $S, S' = \{T, Q, U\}$, and $X, Y = \{T, E, B\}$. The only non-vanishing elements of ω_{SX} are $\omega_{TT} = 1$, $\omega_{UE} = \sin 2\phi_{\mathbf{w}}$, $\omega_{UB} = \cos 2\phi_{\mathbf{w}}$, $\omega_{QE} = \cos 2\phi_{\mathbf{w}}$, and $\omega_{QB} = -\sin 2\phi_{\mathbf{w}}$ [82, 29]. Since the window functions $W_{SS'XY}^{ij}(|\mathbf{w}|)$ are independent of C_b, the integrals in Eq. (5.1) is only calculated once before evaluating the covariance matrices. Starting with an appropriate initial guess, maximization of the likelihood function is achieved for 6 CMB power bands in around 20 CPU-hours. Assuming the likelihood function near its peak can be well-approximated by a Gaussian, the confidence intervals for the derived maximum-likelihood CMB power spectra are found by the inverse of the Hessian matrix at the peak. This procedure requires about 30 CPU-mins for ~ 4000 visibilities.

In flat-sky approximation, the data (4.1) can be modeled with the linear operator

$$\mathbf{B} = \mathcal{F} \cdot \mathbf{A} \cdot \mathcal{F}^{-1} \cdot \boldsymbol{\mathcal{U}}, \tag{5.3}$$

where $\mathcal{F}$ represents the Fourier transformation, acting on the $3n_p$ dimensional Fourier space signal vector $\tilde{\mathbf{s}} = (\ldots, \tilde{T}_i, \tilde{E}_i, \tilde{B}_i, \ldots)$, and $\boldsymbol{\mathcal{U}}$ is a block diagonal matrix with submatrices $\mathbf{U}_{\phi_i}$ of Eq. (3.16) with ϕ_i being the angular polar coordinate of the i^{th} pixel. The signal sampling equation (4.19) can be rearranged, for $\mathbf{s} = \mathbf{x} + \boldsymbol{\xi}$, as

$$\left(\boldsymbol{\mathcal{U}} \mathbf{S}^{-1} \boldsymbol{\mathcal{U}}^\dagger + \mathcal{F}^{-1} \mathbf{A}^\dagger \mathcal{F} \mathbf{N}^{-1} \mathcal{F} \mathbf{A} \mathcal{F}^{-1} \right) \mathbf{x} = \mathcal{F}^{-1} \mathbf{A}^\dagger \mathcal{F} \mathbf{N}^{-1} \mathbf{d}, \tag{5.4a}$$

$$\left(\boldsymbol{\mathcal{U}} \mathbf{S}^{-1} \boldsymbol{\mathcal{U}}^\dagger + \mathcal{F}^{-1} \mathbf{A}^\dagger \mathcal{F} \mathbf{N}^{-1} \mathcal{F} \mathbf{A} \mathcal{F}^{-1} \right) \boldsymbol{\xi} = \boldsymbol{\mathcal{U}} \mathbf{S}^{-1/2} \boldsymbol{\omega}_1 + \mathcal{F}^{-1} \mathbf{A}^\dagger \mathcal{F} \mathbf{N}^{-1/2} \boldsymbol{\omega}_2. \tag{5.4b}$$

We obtain numerical solutions for the Eq. (5.4) by the preconditioned conjugate gradient method [62]. A good choice for the preconditioner is the inverse of the diagonal

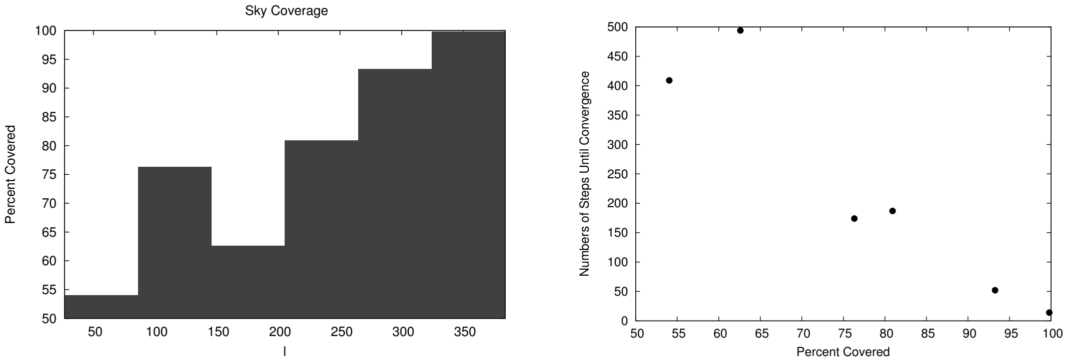

(a) (b)

Figure 5.2: (a) Coverage of uv-plane for each bin $\Delta_b = [\ell_b^{min}, \ell_b^{max}]$. Shown are the percentages of pixels intersected by baseline vectors during the 12-hour observation period in each bin. A pixel in Fourier space is said to be in bin b if its position vector $\mathbf{u}_{pix}$ satisfies $2\pi|\mathbf{u}_{pix}| \in \Delta_b$. (b) The percentage of uv-plane coverage versus the number of steps, after the burn-in phase, required to reach convergence at each ℓ-bin.

part of the operator [28]:

$$\mathbf{P}^{-1} = \mathbf{P}_N^{-1} + diag\{\boldsymbol{\mathcal{U}}\mathbf{S}^{-1}\boldsymbol{\mathcal{U}}^{\dagger}\}. \tag{5.5}$$

The noise portion of the preconditioner, $\mathbf{P}_N$, can be written as [71]

$$\mathbf{P}_N^{-1} = \mathcal{F}(\mathcal{F}^{-1}\mathbf{N}^{-1})(\mathcal{F}^{-1}|\tilde{A}|^2), \tag{5.6}$$

where $\tilde{A}$ is the Fourier transform of the beam pattern.

Signal covariance matrix is sampled by computing the unnormalized variance $\boldsymbol{\sigma}_b$ in an annulus of radius $\ell_b/2\pi$:

$$\boldsymbol{\sigma}_b = \sum_{\ell_i \in b} \ell_i(\ell_i + 1)\ \mathbf{s}_i\mathbf{s}_i^{\dagger} \tag{5.7}$$

where $\mathbf{s}_i = (\tilde{T}_i, \tilde{E}_i, \tilde{B}_i)$ is a three-vector at the i^{th} pixel. Assuming Jeffrey's prior, the number of degrees of freedom becomes $f_b = p_b - 2$, where p_b is the number of pixels in bin b.

We ran four independent Gibbs sampling chains, each chain having $3,000$ iterations of which the first $1,000$ are discarded as the burn-in phase. The convergence is reached in about 500 steps when the potential scale reduction factor of the G-R statistic becomes less than 1.1 for each bin, roughly in 30 CPU-hours. Figure 5.2 shows the uv-plane coverage versus the number of steps, after burn-in, required to reach convergence for each bin. We see that convergence time and uv-plane coverage are weakly correlated. Incomplete coverage leads to a larger correlation length for small power leading to a longer convergence time. Therefore, low-coverage bins have larger effect on overall performance, as expected.

5.1 Power Spectra Inferences

The mean posterior power spectra, together with the associated uncertainties at each ℓ-bin, obtained by the methods of Gibbs Sampling (GS) and Maximum Likelihood (ML) for the ideal experiment with linear polarizers, are shown in Fig. 5.3. The input power spectra, which are used to construct the signal realization, and the spectra of the signal realization are also shown in Fig. 5.3. Nearly all of our estimates fall within 1σ of the expected value [29].

Samples of power spectra produced by Gibbs sampling have highly non-Gaussian probability densities. As an example, we show marginalized posterior joint distributions of EE and TE power spectra for various ℓ-bins in Fig. 5.4. Although combining many modes into each bin has an overall Gaussianizing effect, non-Gaussianity of the distributions is still visible, especially at the bins with lower uv-coverage [28].

Gibbs sampling also provides higher-order statistical information such as the two-point correlations between ℓ-bins. Off-diagonal components of the correlation matrices for TE, EE and BB power spectra are shown in Fig. 5.5. There is a slight correlation between adjacent bins, which is the result of reduced Fourier space resolution caused by finite beam width. The correlation is more pronounced at high ℓ and low signal-to-noise ratio, as seen in BB correlation matrix of Fig. 5.5. Since the correlation matrices carry information about data regions larger than bin sizes, the power spectra are oversampled, causing anti-correlation between nearby bins. Since the power in a region is constraint by the data, whenever a large value is sampled at a certain bin, values of samples from the other bins

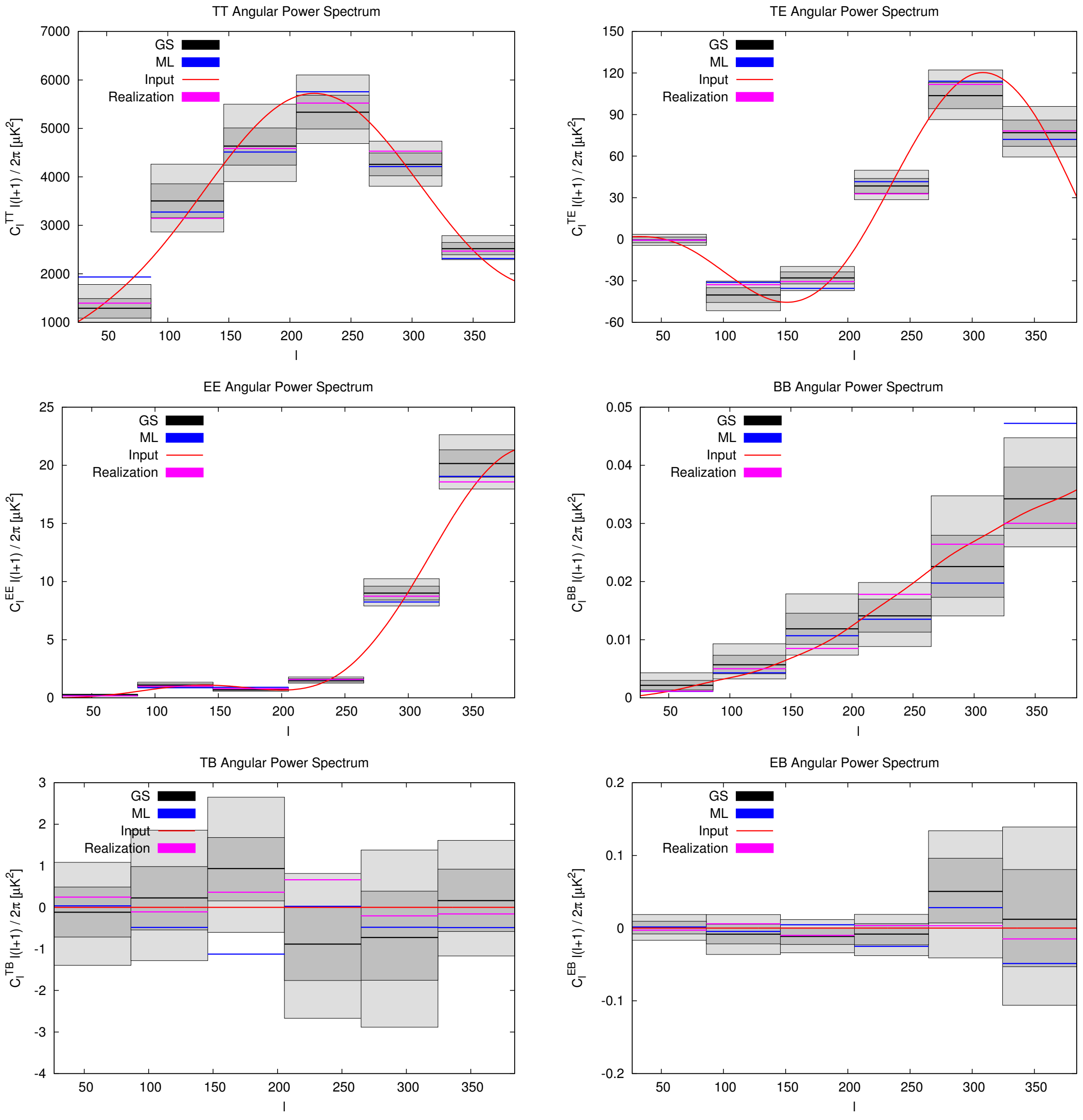

Figure 5.3: Mean posterior power spectra obtained by Gibbs Sampling (GS) for each ℓ-bin are shown in black. The power spectra estimations obtained by Maximum Likelihood (ML) method are shown in blue. Dark and light grey indicate 1σ and 2σ uncertainties for Gibbs sampling results, respectively. The binned power spectra of the signal realization are shown in pink. Red lines are the input CMB power spectra obtained by CAMB for a tensor-to-scalar ratio of $r = 0.01$ [29].

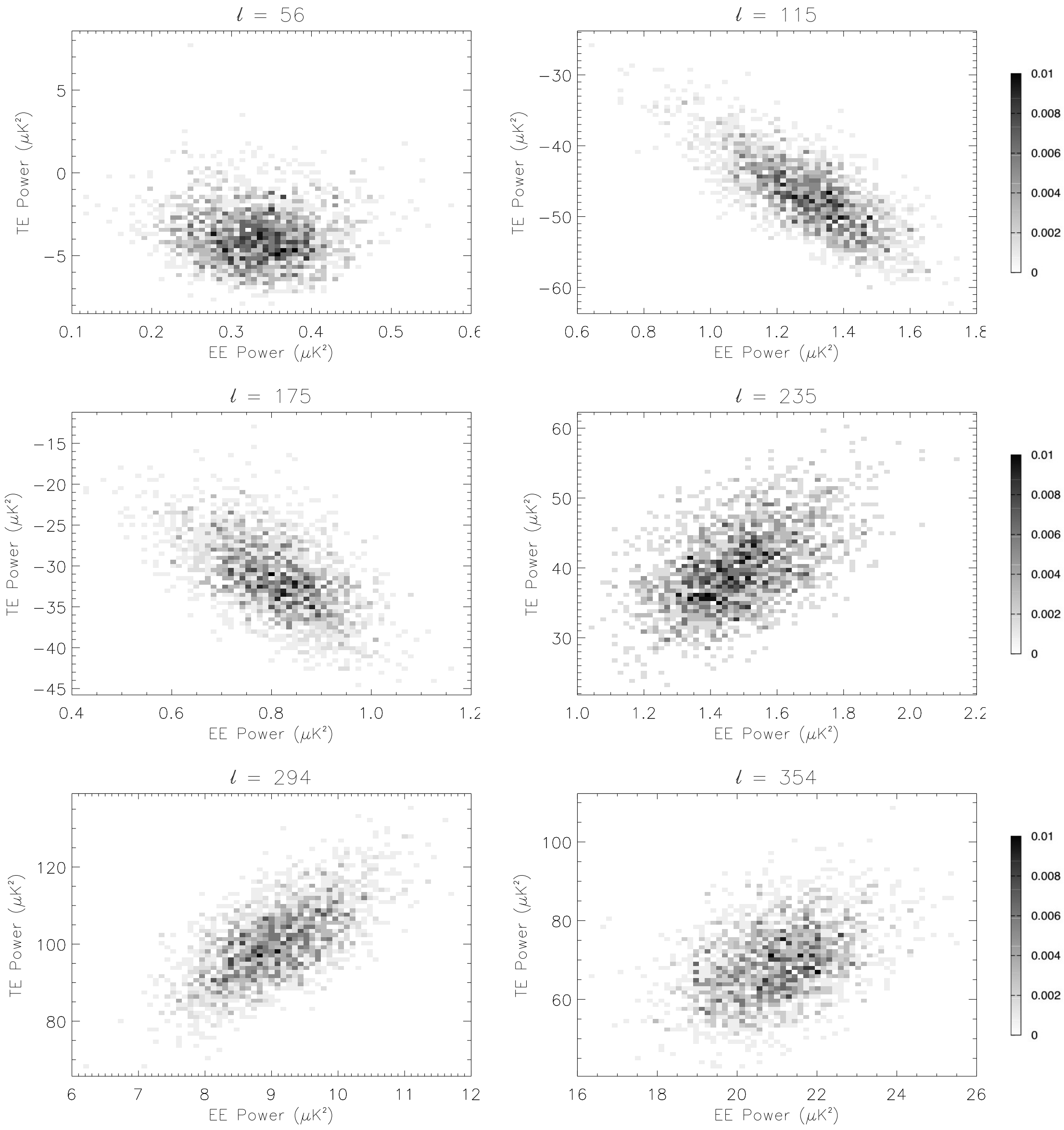

Figure 5.4: Marginalized posterior joint distributions of EE and TE power spectra for different ℓ-bins. Samples of power spectra produced by Gibbs sampling have non-Gaussian distributions.

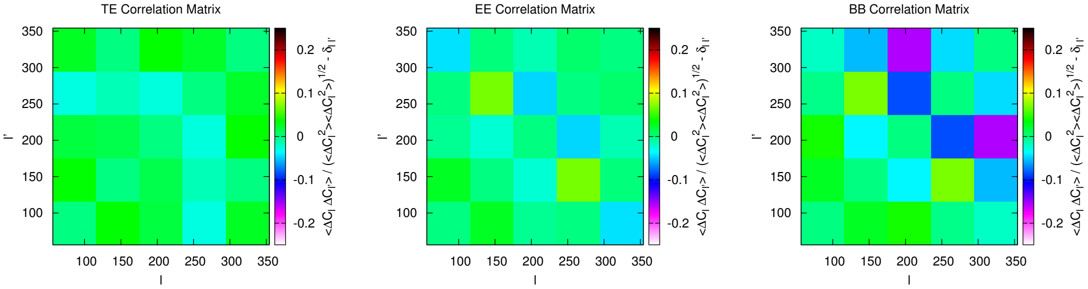

Figure 5.5: Correlation matrices of TE, EE and BB power spectra – diagonal elements are subtracted. Correlations and anti-correlations between nearby power spectrum bins are the results of having a finite beam width and a finite bin size, respectively. Correlations are stronger towards lower signal-to-noise values (from TE to BB) and towards higher ℓ-values.

in the same data region are reduced [28].

5.2 Signal Reconstruction

In addition to the power spectra, Gibbs sampler also provides inference for the observed signal. Signal samples are constructed as constrained realizations by adding a fluctuation map to the mean field (Wiener-filtered) map [28]. We compute Wiener-filtered maps by solving Eq. (5.4a) for $\mathbf{x}$. The Wiener filter provides the information content of the data by filtering out the imperfections caused by finite beam, partial uv-plane coverage and noise. To obtain a Gaussian random variate for the signal sampling we need to add a fluctuation term with zero mean and the covariance of the conditional posterior, $(\mathbf{S}^{-1} + \mathbf{N}^{-1})^{-1}$, to the mean field map. The fluctuations obtained by solving Eq. (5.4b) provide a random complement to the Wiener-filtered map such that their sum is an unbiased signal sample consistent with the data and the current power spectrum. These artificially created fluctuations average out after sufficient iterations leaving us with a reconstruction of the input signal within the area of the primary beam, which we show in Fig. 5.6 as the "Final Mean Reconstructed Signal". For comparison, the "Input Signal" which is constructed from the input power spectra shown in red in Fig. 5.3 is also shown.

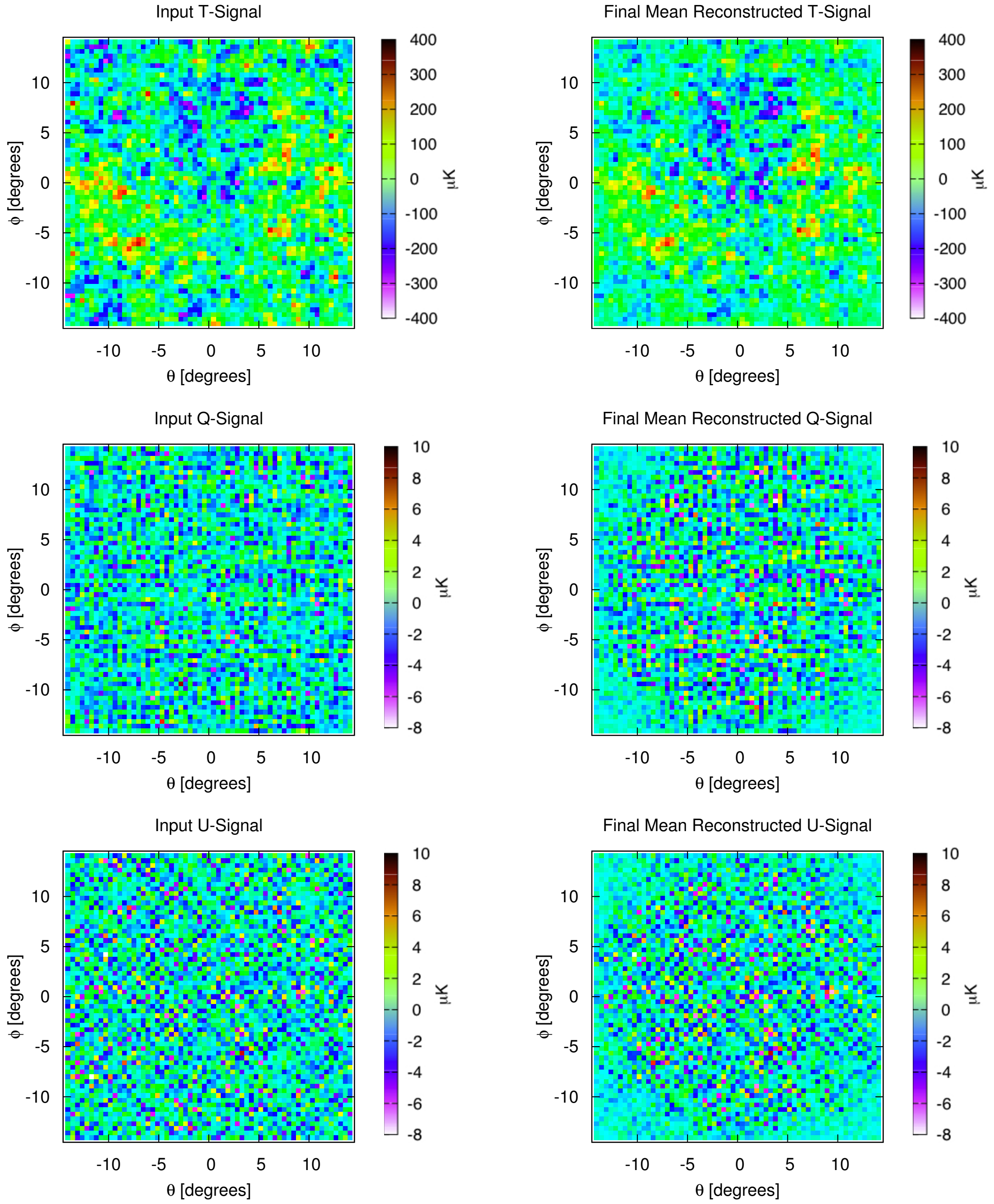

(a) Input Maps (b) Final Maps

Figure 5.6: Signal maps. (a) The signal realization, which is constructed from the input power spectra shown in red in Fig. 5.3, is used as the input map for the interferometer simulation. (b) The final mean posterior map is the sum of solutions of Eq. 5.4; $\langle F^{-1}\boldsymbol{\mathcal{U}}(\mathbf{x}+\boldsymbol{\xi})\rangle$, transformed into Stokes variables T, Q and U and averaged over all iterations. It provides the reconstruction of the noiseless input signal by the Gibbs sampler within the area of the primary beam. The three rows show, from top to bottom, temperature, Stokes Q and Stokes U parameters.

Error Type	*Parameter*	*RMS Value*
Gain	$\lvert g_{rms}\rvert$	0.1
Coupling	$\lvert \epsilon_{rms}\rvert$	5×10^{-4}
Pointing	δ_{rms}	0.7°
Shape	ζ_{rms}	0.7°
Cross-polarization	μ_{rms}	5×10^{-4}

Table 5.1: Root-mean-square values of the error parameters estimated to keep the value of α_r less than 10% tolerance limit at $r = 0.01$ [29].

5.3 Systematic Effects on Power Spectra Inferences

Our interferometer design generates a large number of redundant baselines, ~ 10 baselines per visibility, which can be used to employ a self-calibration technique to significantly reduce the level of systematic errors [43, 30]. Assuming such a calibration has already been made, in this section we shall determine the control levels of residual systematic errors through a complete pipeline of realistic simulations.

In order to estimate the control levels of systematics, we ran preliminary simulations guided by our analytical estimations for a tolerance limit of $\alpha_r = 10\%$ at $r = 0.01$. The rms values of the parameters are given in the Table 5.1. To determine α^{XY} and α_r rigorously, we ran 30 realizations of each systematic error simulation for both linear and circular experiments.

Figure 5.7 shows the mean values of α^{XY} for beam errors, averaged over 30 realizations. The results from ML and GS methods are in good agreement for both linear and circular experiments. In all three cases $\alpha^{BB} \sim 0.1$ at low ℓ, as expected. Although the cross polarization has a much smaller error parameter, its effect on the power spectra is comparable to the pointing and shape errors. The reason for this is the leakage from TT power into BB power that is caused by the off-diagonal elements of the beam pattern, whereas the source of α^{BB} for pointing and shape errors is the $EE \rightarrow BB$ leakage [29].

The mean values of α^{XY} for instrumental errors are shown in Fig. 5.8. For gain and

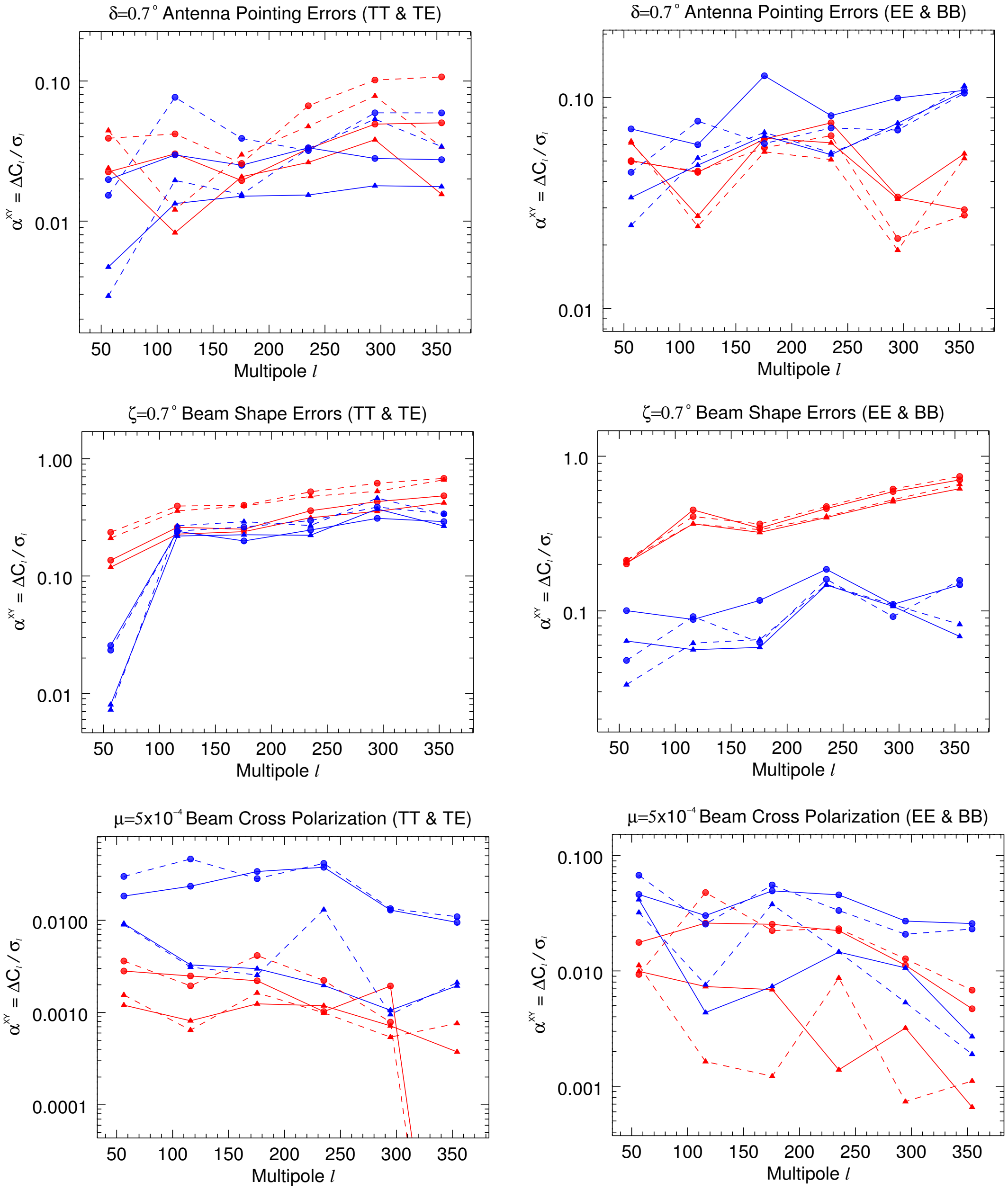

Figure 5.7: Beam errors. The values of α^{XY}, averaged over 30 simulations, obtained by both maximum likelihood (ML) method (triangles) and the method of Gibbs sampling (GS) (solid dots) are shown. The three rows indicate, from top to bottom, pointing errors with $\delta_{rms} \approx 0.7°$, beam shape errors with $\zeta_{rms} \approx 0.7°$, and beam cross-polarization with $\mu_{rms} = 5 \times 10^{-4}$. Left panel shows α^{TT} (red) and α^{TE} (blue). Middle panel shows α^{EE} (red) and α^{BB} (blue). Linear and circular experiments are shown by solid and dashed lines, respectively [29].

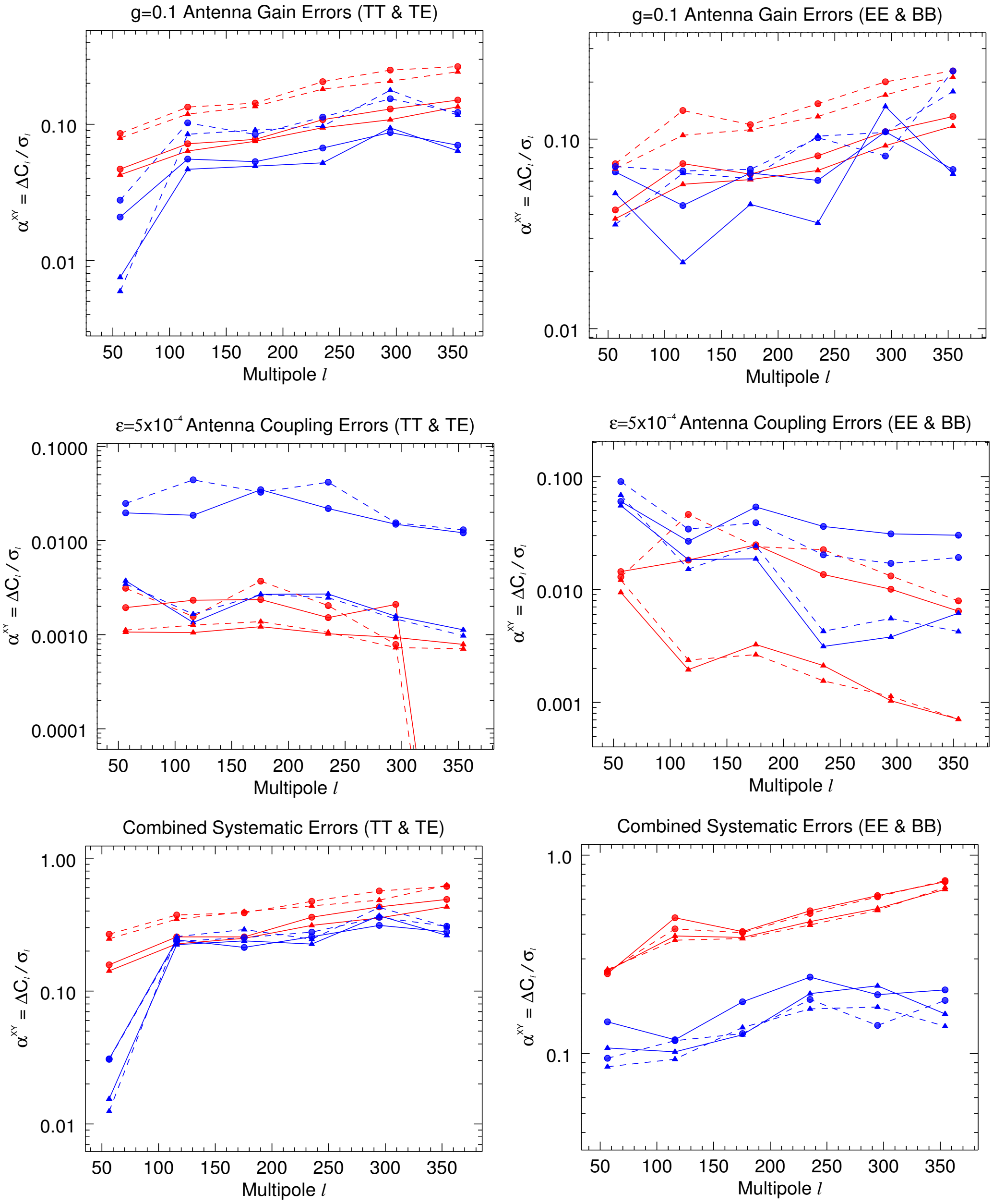

Figure 5.8: Instrumental and combined systematic errors. The values of α^{XY}, averaged over 30 simulations, obtained by both maximum likelihood (ML) method (triangles) and the method of Gibbs sampling (GS) (solid dots) are shown. Top row: antenna gain with $|g_{rms}| = 0.1$. Middle row: antenna couplings with $|\epsilon_{rms}| = 5 \times 10^{-4}$. Bottom row: combined effect of beam and instrumental systematic errors. Left panel shows α^{TT} (red) and α^{TE} (blue). Middle panel shows α^{EE} (red) and α^{BB} (blue). Linear and circular experiments are shown by solid and dashed lines, respectively [29].

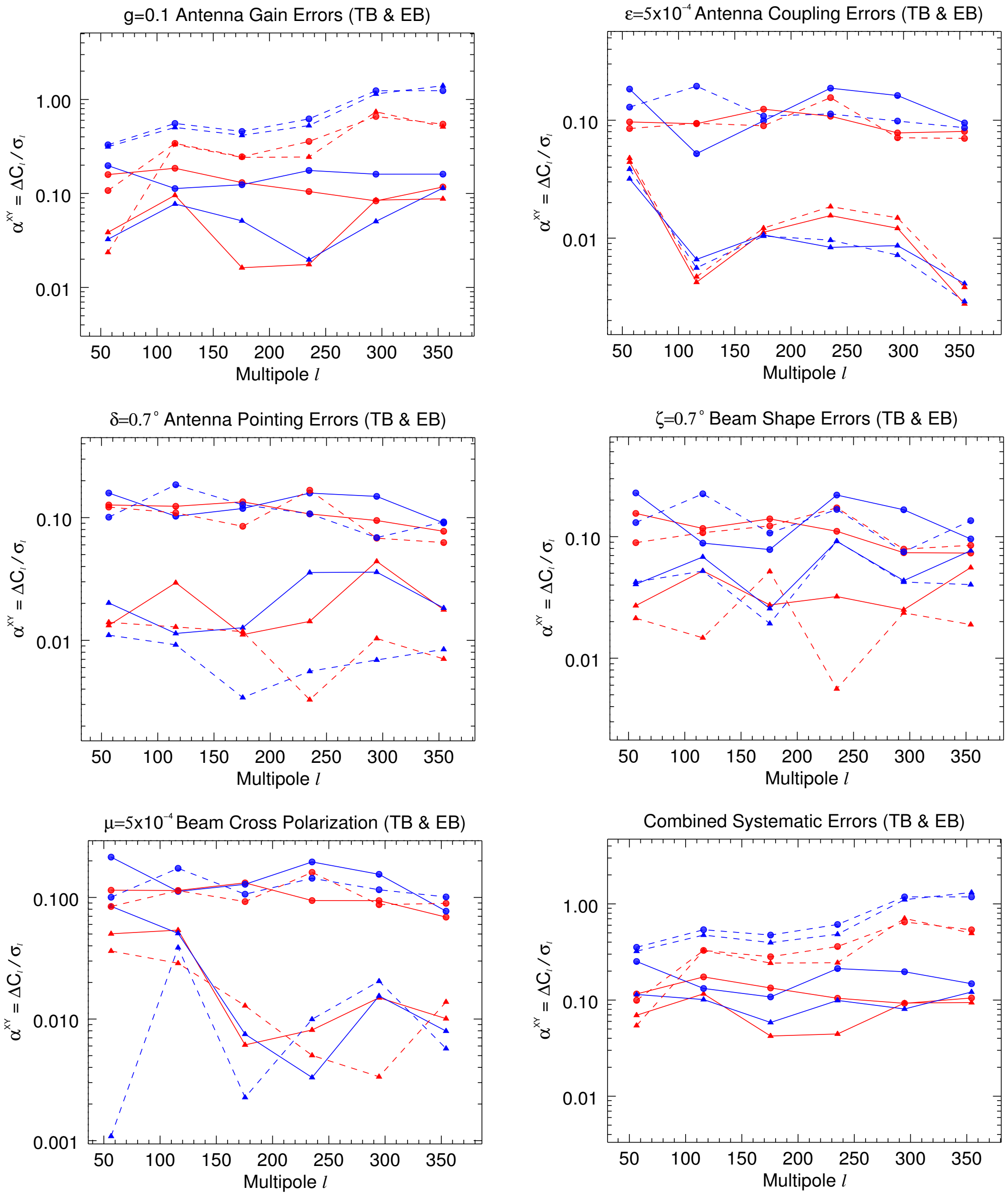

Figure 5.9: Panels show α^{TB} (red) and α^{EB} (blue). The values of α^{XY}, averaged over 30 simulations, obtained by both maximum likelihood (ML) method (triangles) and the method of Gibbs sampling (GS) (solid dots) are shown for antenna gain with $|g_{rms}| = 0.1$, antenna couplings with $|\epsilon_{rms}| = 5 \times 10^{-4}$, pointing errors with $\delta_{rms} \approx 0.7^{\circ}$, beam shape errors with $\zeta_{rms} \approx 0.7^{\circ}$, and beam cross-polarization with $\mu_{rms} = 5 \times 10^{-4}$. Linear and circular experiments are shown by solid and dashed lines, respectively [29].

coupling errors, α^{XY} is roughly at the 10% level. The main contribution for the α^{BB} comes from the leakage from EE power into BB power for gain errors. As in the case of cross-polarization errors, despite having a much smaller parameter than gain, $\alpha^{BB} \sim 0.1$ at low ℓ for antenna coupling errors because of $TT \rightarrow BB$ leakage.

We simulated the systematics by turning on one error at a time. However, in a realistic experiment, all systematic errors act together simultaneously, causing a larger effect on the spectra. In order to see this combined effect we ran 30 realizations with all the systematic errors discussed in previous sections turned on at once. The results are also shown in Fig. 5.8. As expected, the combined effect is almost twice as large as the individual cases.

Although, ideally, cross-correlation spectra C^{TB} and C^{EB} vanish due to the negative parity of the B modes, systematic effects induce biases for these cases, as well. The mean values of α^{TB} and α^{EB} for each type of error are shown in Fig. 5.9.

5.4 Comparison to Analytical Estimations

Analytical estimations for α^{XY} are obtained from the quadrature difference of Eq. 3.32, normalized by the number of baselines. In general α^{XY} has a polynomial dependence on $\overline{s^2}$. For our interferometer configuration roughly $\overline{s^2} \sim 262.7/\ell^2$. The explicit forms of the unnormalized estimations are given in the Appendix A.

In general, our simulated results are larger than the estimations in all ℓ-bins. This is expected because our analytical estimations are only first order approximations where it is also assumed that the errors associated with baselines are uncorrelated, making them lower bounds for the estimations. In reality, there is a correlation between errors associated with baselines having common antennas, a fact that is captured by our simulations. Upper bounds for the estimations can be found by unrealistically assuming full correlation of errors between baselines, where each baseline has the same error. For our interferometer design, this corresponds to roughly 65 times larger values. We expect our results to fall between uncorrelated and fully correlated estimations. In order to compare our results

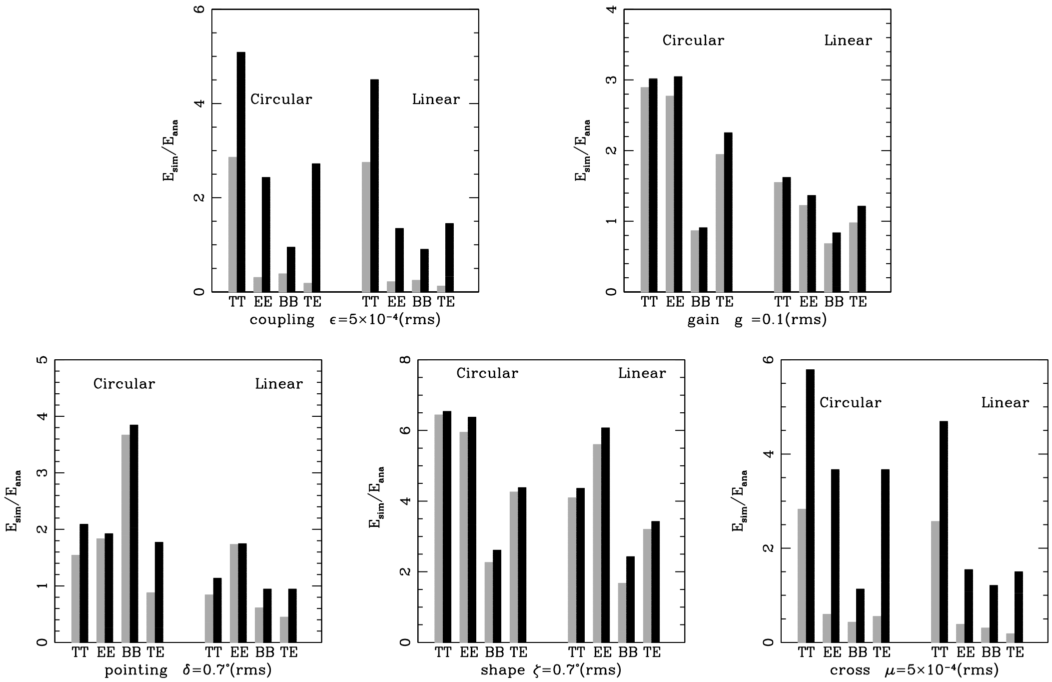

Figure 5.10: The bin-averaged ratios of the simulated and analytical systematic errors. In each panel, the results from the simulations in both the linear and circular bases for TT, EE, BB, TE are shown. The gray and black bars correspond to the maximum-likelihood and Gibbs-sampling methods in analysis of the simulated data, respectively [29].

with the analytical ones, we consider the rms values of α^{XY} averaging over the ℓ-bins. Figure 5.4 shows the ratios of α^{XY}_{rms} obtained by ML and GS methods to the estimated α^{XY}_{rms}. In most cases, both methods are in agreement with the analytical results within a factor of 6.

5.5 Biases in Tensor-to-Scalar Ratio

The major goal of QUBIC-like experiments is to detect the signals of the primordial B-modes, the magnitude of which is characterized by the tensor-to-scalar ratio r. In this context, it is necessary to propagate the effects of systematic errors through r to assess properly the systematic-induced biases in the primordial B-mode measurements.

The shape of the primordial BB power spectrum $C^{BB}_{\ell,prim}$ is insensitive to r but the amplitude is directly proportional to r. We can straightforwardly convert the amplitude of the systematic-induced false BB into the bias in r by writing $C^{BB}_{\ell,prim} = r\ C^{BB}_{\ell,r=1}$ in

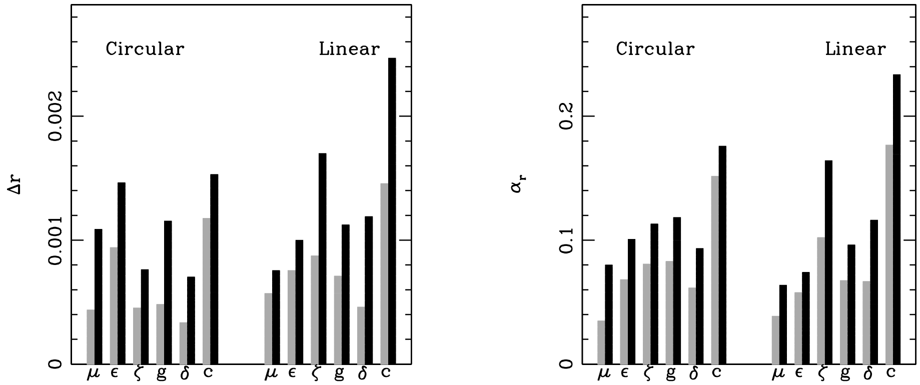

Figure 5.11: The simulated systematic-induced biases in the tensor-to-scalar ratio r (left) and α_r (right) for the same systematic errors as in Fig. 5.7 and 5.8. All the results derived from the maximum-likelihood (gray) and Gibbs-sampling (black) analyses based on the simulations in both the linear and circular bases are shown [29].

Eq. (3.36) and Eq. (3.37) where $C^{BB}_{\ell,r=1}$ is the CAMB calculated primordial BB power spectrum at $r = 1$. The tensor-to-scalar ratios obtained from ideal linear experiment by Gibbs sampling and maximum likelihood methods are found as $r_{GS} = 0.026 \pm 0.012$ and $r_{ML} = 0.006 \pm 0.0095$, respectively. A more conservative estimation for r can be obtained without subtracting the lensed spectrum in Eq. (3.36) and by taking only the first bin where the effect of lensing is the least; $r^{lensed}_{GS} = 0.038 \pm 0.014$ and $r^{lensed}_{ML} = 0.0196 \pm 0.011$.

We vary each systematic error individually and also consider the cross contributions between each error. In realistic observations, all different systematic errors are likely to occur at the same time and we need to understand their combined effects well. We thus evaluate such effects by simulating the systematic errors occurring simultaneously during the observation. The individual and combined systematic-induced biases in r are illustrated in Fig. 5.11, evaluated by both the GS and ML methods based on the simulations performed in the linear and circular bases. Both methods demonstrate good agreement, within a factor of 2.5. Note that ML method consistently underestimates the biases. The reason for that is that the Gaussianity assumption for the data distribution does not hold well because of the incomplete uv-coverage, pixelation, and, especially at low ℓ-bins, the finite beam size, making the ML estimations for the statistical errors less reliable. Although the mock visibility data are simulated based on only one realization of CMB anisotropy fields, drawn from the power spectra with input BB for $r = 0.01$, the resulting false BB band-powers for the different systematic errors are expected to be a good approximation for other r values since the leading-order false B-modes are contaminated only by the leakage of TT, TE and EE power spectra, which are independent of r.

The simulations show that, due to the leakage of TT signals into BB, even though the cross-polarization and coupling errors are very small, e.g., $\mu_{rms} = 5 \times 10^{-4}$ and $|\epsilon_{rms}| = 5 \times 10^{-4}$, the resulting biases in r are comparable to those induced by relatively larger pointing, gain and shape errors. In addition, when increasing the cross-polarization and coupling errors by a factor of 10, the simulations show that the resulting biases would roughly increase by the same factor. As expected, the systematic errors are approximately linearly proportional to their error parameters. We also find that the combined systematic effects (referred to as "c" in Fig. 5.11) would increase the biases and their values are consistent with the quadrature sum of the individual errors within 10%.

If we set up an allowable tolerance level of 10% on r, where r is assumed to be $r = 0.01$, for QUBIC-like experiments the error parameters adopted as in Fig. 5.11 satisfy this threshold when each systematic error occurs alone during observations. But if all the systematic errors are present at the same time, on average, we require roughly 2 times better systematic control on each error parameter for a linear experiment. Nevertheless, the bias in r for a circular experiment, being around 15%, is still within the acceptable level. Although the tolerance level for r is chosen to be $\alpha_r = 0.1$, our results can directly apply to any other desired threshold level to the extent that the linear dependence of systematic effects on error parameters is a good approximation for sufficiently small error parameters.

Chapter 6

Further Directions

6.1 Foregrounds

The major systematic effect that we have not consider yet is the galactic and extragalactic foreground signals which dominate the CMB polarization signal over a large part of the sky. Ground based experiments choose to observe regions of the celestial sphere that are relatively quiet in galactic foreground emission. An ideal observation location for such a region is the South Pole where the observed sky includes some of the largest regions of minimal Galactic foreground emission on the celestial sphere.

Main foreground contamination sources for the CMB polarization signal are the diffuse galactic foregrounds: synchrotron, free-free, and dust emission, and extra galactic contamination: the SZ effect, and point sources [73]. In order to extract unbiased cosmological information, the foreground components must be successfully separated from the CMB signal. The method of Gibbs sampling can be extended to include an efficient Bayesian component separation technique through signal sampling for multifrequency observations [15]. The data taken at frequency ν can be written as, including the Stokes V that could be produced by some foreground signals, a $4n_p$ dimensional vector:

$$\mathbf{d}_\nu = \mathbf{A}_\nu \left(\mathbf{s} + \sum_{k=1}^{n_f} \mathbf{f}_\nu^k \right) + \mathbf{n}_\nu \tag{6.1}$$

where $\mathbf{s}$ is the signal, which has the same spectrum at each frequency, $\mathbf{f}_\nu^k$ is the k^{th} foreground component, $\mathbf{n}_\nu$ is the noise and $\mathbf{A}_\nu$ represents the beam convolution operator.

The foreground components can be modeled as

$$\mathbf{f}_\nu = \sum_{k=1}^{n_f} \mathbf{f}_\nu^k = \mathbf{G}_\nu \cdot \mathbf{c} = \mathbf{G}_\nu \cdot \begin{pmatrix} \mathbf{c}_1 \\ \vdots \\ \mathbf{c}_{n_f} \end{pmatrix} \tag{6.2}$$

where $\mathbf{c}_k$ is the $4n_p$ dimensional amplitude vector of the k^{th} foreground component and $\mathbf{G}_\nu$ is an $4n_p \times 4n_p n_f$ matrix:

$$\mathbf{G}_\nu = \begin{pmatrix} \mathbf{G}_\nu^1 & \dots & \mathbf{G}_\nu^{n_f} \end{pmatrix}. \tag{6.3}$$

$\mathbf{G}_\nu^k$ are defined as $4n_p \times 4n_p$ diagonal matrices representing the frequency spectrum:

$$\mathbf{G}_\nu^k = diagonal\ \left\{\ g_k^p(\nu, \alpha_k^p(i))\ \right\}, \quad i = 1, ..., n_p, \quad and \quad p = \{T, Q, U, V\}, \tag{6.4}$$

where $g_k^p(\nu, \alpha_k^p(i))$ is generally modeled as a power law $g_k^p(\nu, \alpha_k^p(i)) = b_k^p(\nu)\nu^{\alpha_k^p(i)}$ [32], and the spectral index $\alpha_k^p(i)$ has a different value at each line of sight for each polarization.

In terms of harmonic coefficients $\tilde{\mathbf{s}} = (\dots, a^s_{T,\ell m}, a^s_{E,\ell m}, a^s_{B,\ell m}, a^s_{V,\ell m}, \dots)$ and $\tilde{\mathbf{c}} = (\dots, a^k_{T,\ell m}, a^k_{E,\ell m}, a^k_{B,\ell m}, a^k_{V,\ell m}, \dots)$, the data can be written as

$$\mathbf{d}_\nu = \mathbf{B}_\nu \cdot \tilde{\mathbf{s}} + \mathbf{\Theta}_\nu \cdot \tilde{\mathbf{c}} + \mathbf{n}_\nu, \tag{6.5}$$

where $\mathbf{B}_\nu$ and $\mathbf{\Theta}_\nu$ are block column matrices with submatrices $\mathbf{B}_\nu^i = (\dots, \mathbf{B}_{\nu,\ell m}, \dots)$ and $\mathbf{\Theta}_\nu^i = (\dots, \mathbf{\Theta}^k_{\nu,\ell m}, \dots)$;

$$\mathbf{B}_{\nu,\ell m} = \begin{pmatrix} \beta^\nu_{\ell m} & 0 & 0 & 0 \\ 0 & \frac{1}{2}(\beta^\nu_{2,\ell m} + \beta^\nu_{-2,\ell m}) & \frac{i}{2}(\beta^\nu_{2,\ell m} - \beta^\nu_{-2,\ell m}) & 0 \\ 0 & -\frac{i}{2}(\beta^\nu_{2,\ell m} - \beta^\nu_{-2,\ell m}) & \frac{1}{2}(\beta^\nu_{2,\ell m} + \beta^\nu_{-2,\ell m}) & 0 \\ 0 & 0 & 0 & \beta^\nu_{\ell m} \end{pmatrix}, \tag{6.6a}$$

$$\mathbf{\Theta}^k_{\nu,\ell m} = \begin{pmatrix} \theta^{k,\nu}_{T,\ell m} & 0 & 0 & 0 \\ 0 & \frac{1}{2}({}_2\theta^{k,\nu}_{Q,\ell m} + {}_{-2}\theta^{k,\nu}_{Q,\ell m}) & \frac{i}{2}({}_2\theta^{k,\nu}_{Q,\ell m} - {}_{-2}\theta^{k,\nu}_{Q,\ell m}) & 0 \\ 0 & -\frac{i}{2}({}_2\theta^{k,\nu}_{U,\ell m} - {}_{-2}\theta^{k,\nu}_{U,\ell m}) & \frac{1}{2}({}_2\theta^{k,\nu}_{U,\ell m} + {}_{-2}\theta^{k,\nu}_{U,\ell m}) & 0 \\ 0 & 0 & 0 & \theta^{k,\nu}_{V,\ell m} \end{pmatrix}, \tag{6.6b}$$

where $\beta^{\nu}_{s,\ell m}$ are given by Eq. (3.13) for the beam pattern A_ν, and

$$\theta^{k,\nu}_{p,\ell m} = \int Y^m_\ell(\hat{\mathbf{r}}) A_\nu(\boldsymbol{\sigma}) g^p_k(\nu, \alpha^p_k(\boldsymbol{\sigma})) e^{-2\pi i \boldsymbol{\sigma}\cdot\mathbf{u}} d\Omega, \tag{6.7a}$$

$$_{\pm 2}\theta^{k,\nu}_{p,\ell m} = -\int {}_{\pm 2}Y^m_\ell(\hat{\mathbf{r}}) A_\nu(\boldsymbol{\sigma}) g^p_k(\nu, \alpha^p_k(\boldsymbol{\sigma})) e^{-2\pi i \boldsymbol{\sigma}\cdot\mathbf{u}} d\Omega. \tag{6.7b}$$

We define a block vector of amplitude coefficients $\mathbf{x} = (\tilde{\mathbf{s}}, \tilde{\mathbf{c}})$ and a symbolic block vector of matrices $\mathbf{H}_\nu = (\mathbf{B}_\nu\ ,\ \boldsymbol{\Theta}_\nu)$ such that the data can be written as $\mathbf{d}_\nu = \mathbf{H}_\nu \cdot \mathbf{x} + \mathbf{n}_\nu = \mathbf{H}_\nu \cdot \boldsymbol{\rho}_\nu$, where $\boldsymbol{\rho}_\nu = (\ \tilde{\mathbf{s}} + \mathbf{n}_{r,\nu}\ ,\ \tilde{\mathbf{c}}\ )$. To sample all components we write the joint amplitude distribution as:

$$\begin{aligned} P(\tilde{\mathbf{s}}, \tilde{\mathbf{c}}_k | \boldsymbol{\Sigma}, \boldsymbol{\alpha}, \mathbf{d}) &\propto P(\mathbf{d}|\mathbf{x}, \boldsymbol{\Sigma}) P(\mathbf{x}|\boldsymbol{\Sigma}) \\ &\propto \exp\left\{-\frac{1}{2}\sum_\nu^{n_z} (\mathbf{d}_\nu - \mathbf{H}_\nu \cdot \mathbf{x})^\dagger \mathbf{N}_\nu^{-1} (\mathbf{d}_\nu - \mathbf{H}_\nu \cdot \mathbf{x})\right\}\ \exp\left\{-\frac{1}{2}\mathbf{x}^\dagger \boldsymbol{\Sigma}^{-1}\mathbf{x}\right\} \\ &\propto \exp\left\{-\frac{1}{2}\sum_\nu^{n_z} (\boldsymbol{\rho}_\nu - \mathbf{x})^\dagger \cdot \mathbf{M}_\nu^{-1} \cdot (\boldsymbol{\rho}_\nu - \mathbf{x})\right\}\ \exp\left\{-\frac{1}{2}\mathbf{x}^\dagger \boldsymbol{\Sigma}^{-1}\mathbf{x}\right\} \end{aligned} \tag{6.8}$$

where

$$\mathbf{M}_\nu^{-1} = \mathbf{H}_\nu{}^\dagger\ \mathbf{N}_\nu^{-1}\ \mathbf{H}_\nu = \begin{pmatrix} \mathbf{B}_\nu^\dagger \mathbf{N}_\nu^{-1} \mathbf{B}_\nu & \mathbf{B}_\nu^\dagger \mathbf{N}_\nu^{-1} \boldsymbol{\Theta}_\nu \\ \boldsymbol{\Theta}_\nu^\dagger \mathbf{N}_\nu^{-1} \mathbf{B}_\nu & \boldsymbol{\Theta}_\nu^\dagger \mathbf{N}_\nu^{-1} \boldsymbol{\Theta}_\nu \end{pmatrix}, \tag{6.9}$$

and

$$\boldsymbol{\Sigma} = \left\langle \mathbf{x}\ \mathbf{x}^\dagger \right\rangle = \begin{pmatrix} \mathbf{S} & \\ & \mathbf{C} \end{pmatrix}, \tag{6.10}$$

assuming the signal and the foregrounds are uncorrelated. As before, the Wiener filtered signal can be written as $\boldsymbol{\mu}_x = (\boldsymbol{\Sigma}^{-1} + \sum_\nu \mathbf{M}_\nu^{-1})^{-1} \sum_\nu \mathbf{M}_\nu^{-1} \boldsymbol{\rho}_\nu$, and the sampling equation becomes

$$\left(\boldsymbol{\Sigma}^{-1} + \sum_\nu^{n_z} \mathbf{M}_\nu^{-1}\right) \cdot \mathbf{x} = \begin{pmatrix} \sum_\nu \mathbf{B}_\nu^\dagger \mathbf{N}_\nu^{-1} \mathbf{d}_\nu + \mathbf{S}^{-\frac{1}{2}} \boldsymbol{\omega}_s + \sum_\nu \mathbf{B}_\nu^\dagger \mathbf{N}_\nu^{-\frac{1}{2}} \boldsymbol{\chi} \\ \sum_\nu \boldsymbol{\Theta}_\nu^\dagger \mathbf{N}_\nu^{-1} \mathbf{d}_\nu + \mathbf{C}^{-\frac{1}{2}} \boldsymbol{\omega}_c + \sum_\nu \boldsymbol{\Theta}_\nu^\dagger \mathbf{N}_\nu^{-\frac{1}{2}} \boldsymbol{\chi} \end{pmatrix}, \tag{6.11}$$

where $\boldsymbol{\omega} = (\boldsymbol{\omega}_s, \boldsymbol{\omega}_c)$ and $\boldsymbol{\chi}$ are univariate Gaussian random fields. Eq. (6.11) represents $4(\ell_{max} + 1)^2 (n_f + 1)$ linear equations which can be solved by applying the preconditioned conjugate gradients method.

Spectrum sampling is achieved by independently sampling the signal and foreground covariances. Signal covariance is sampled exactly the same way as before. The foreground covariance $\mathbf{C}$ is a block diagonal matrix with 4×4 submatrices

$$\boldsymbol{\Gamma}_\ell = \begin{pmatrix} \Gamma_\ell^{TT} & \Gamma_\ell^{TE} & \Gamma_\ell^{TB} & \Gamma_\ell^{TV} \\ \Gamma_\ell^{ET} & \Gamma_\ell^{EE} & \Gamma_\ell^{EB} & \Gamma_\ell^{EV} \\ \Gamma_\ell^{BT} & \Gamma_\ell^{BE} & \Gamma_\ell^{BB} & \Gamma_\ell^{BV} \\ \Gamma_\ell^{VT} & \Gamma_\ell^{VE} & \Gamma_\ell^{VB} & \Gamma_\ell^{VV} \end{pmatrix}, \tag{6.12}$$

where Γ_ℓ^{XY} is the XY power spectrum of the foreground signal. The foreground covariance is sampled from an inverse Wishart distribution $\mathcal{W}(\mathbf{C}, h_b)$ by drawing $h_b = L_b - 5 + 2q$ vectors, L_b being the number of monopoles in the bin b, from a Gaussian distribution with covariance matrix $\boldsymbol{\gamma}_b^{-1}$, where

$$\boldsymbol{\gamma}_b = \sum_{\ell \in b} \sum_{m=-\ell}^{m=\ell} \ell(\ell+1) \mathbf{c}_{\ell m} \mathbf{c}_{\ell m}^\dagger \tag{6.13}$$

with the four-vector $\mathbf{c}_{\ell m} = (a_{f,\ell m}^T, a_{f,\ell m}^E, a_{f,\ell m}^B, a_{f,\ell m}^V)$, where $a_{f,\ell m}^V$ is the harmonic coefficient of the Stokes V parameter of the foreground signal. The uninformative prior is chosen to be $P(\mathbf{C}) \propto \prod_\ell |\boldsymbol{\Gamma}_\ell|^{-q}$, where $q = 0$ for a uniform prior, and $q = 1$ for a Jeffrey's prior. The sample $\boldsymbol{\Gamma}_b$ is, then, given by the inverse of the sum of outer products of these independently sampled vectors.

To complete the Gibbs sampling, we must add another step, namely the spectral index sampling. Starting from initial guesses for spectral indices $\boldsymbol{\alpha}$ and the component covariances $\boldsymbol{\Sigma}$, the sampling iterations become [15]

$$\{\tilde{\mathbf{s}}, \tilde{\mathbf{c}}\}^{i+1} \leftarrow P(\tilde{\mathbf{s}}, \tilde{\mathbf{c}}_k | \boldsymbol{\Sigma}^i, \boldsymbol{\alpha}^i, \mathbf{d}), \tag{6.14a}$$

$$\mathbf{S}^{i+1} \leftarrow P(\mathbf{S} | \tilde{\mathbf{s}}^{i+1}), \tag{6.14b}$$

$$\mathbf{C}^{i+1} \leftarrow P(\mathbf{C} | \tilde{\mathbf{c}}^{i+1}), \tag{6.14c}$$

$$\alpha_k^{i+1} \leftarrow P(\alpha_k | \tilde{\mathbf{s}}^{i+1}, \tilde{\mathbf{c}}^{i+1}, \{\alpha_{k' \neq k}\}^i, \mathbf{d}). \tag{6.14d}$$

Sampling α_k^{i+1} can be done directly from the conditional density by inversion sampling method: $r = \int_0^{\alpha_k} d\alpha \; P(\alpha|\tilde{\mathbf{s}}, \tilde{\mathbf{c}}, \{\alpha_{k'\neq k}\}, \mathbf{d})$, where r is a random number drawn from the uniform distribution $U[0,1]$, and

$$P(\alpha|\tilde{\mathbf{s}}, \tilde{\mathbf{c}}, \{\alpha_{k'\neq k}\}, \mathbf{d}) = \mathcal{L}(\alpha)P(\alpha) = \exp\left(-\frac{1}{2}\sum_{\nu}\left[\frac{\mathbf{d}_\nu - \mathbf{A}_\nu(\mathbf{s}+\mathbf{f}_\nu)}{\sigma_n}\right]^2\right)P(\alpha), \qquad (6.15)$$

σ_n^2 being the noise variance [15]. The prior $P(\alpha)$ can be chosen as Jeffrey's prior:

$$P(\alpha) \propto \sqrt{F_{\alpha\alpha}} = \sqrt{-\left\langle \frac{\partial^2 \ln \mathcal{L}}{\partial^2 \alpha} \right\rangle}. \qquad (6.16)$$

Note that the consecutive samples of spectral indices are moderately correlated. In order to reduce the correlation, the last step in each main Gibbs sampling loop (6.14) must be iterated a few times.

6.2 21 cm HI Emission Line

Hyperfine transition line of the neutral hydrogen provides the only known probe to cosmic dark ages, $200 \gtrsim z \gtrsim 30$, from recombination to reionization. Since it is a single frequency radiation, redshift surveys can give three dimensional information about the evolution of matter distribution in the universe. Redshifted 21 cm radiation can potentially provide more precise measurements of cosmological parameters than either the CMB or galaxy surveys, and put rigorous constraints on the properties of dark matter, dark energy [44, 51], and non-Gaussianity from inflation [45].

Neutral hydrogen was reionized by the ultraviolet radiation emitted after the formation of the first stars at $z \sim 30$. Observations of 21 cm emission line at the frequency of the Epoch of Reionization (EoR) can provide valuable information about the formation of the first stars.

After reionization, the residual neutral hydrogen accumulates on the density peaks of the Baryon Acoustic Oscillations, given by the sound horizon at recombination, a characteristic scale of ∼150 Mpc, which is determined by the CMB observations to high accuracy. Measurements of the 21 cm power spectrum over a range of redshifts establish the expansion history through the evolution of this standard ruler provided by BAO. The measurement of the angle subtended by the ruler of length $\Delta\chi(z)$ gives the angular diameter distance $d_A(z)$:

$$d_A(z) = \frac{c}{1+z}\int_0^z \frac{dz'}{H(z')} = \frac{\Delta\chi(z)}{\Delta\theta}. \tag{6.17}$$

The redshift interval, Δz, associated with $\Delta\chi(z)$ determines the Hublle parameter:

$$H(z) = \frac{c\Delta z}{\Delta\chi(z)}. \tag{6.18}$$

Precise measurements of the expansion rate of the universe over $0 < z \lesssim 3$ can ascertain the redshift evolution of the dark energy equation of state and provide further insight into the nature of dark energy.

Several ground based interferometric observations of the 21 cm emission signal are being developed, such as LEDA [39], MWA [52], PAPER [57], LOFAR [46], and CHIME [8]. LEDA measures the sky-averaged 21 cm signal as a function of redshift, whereas the others measure the power spectrum.

The Gibbs sampling method naturally extends to the 3D power spectrum inference from interferometric data of 21 cm signal. Data can be written as an $n_p n_z$ vector, where n_z is the number of redshift slices, and n_p is the number of pixels in each slice. The convolution operator $\mathbf{B}$ of Eq. (4.1) becomes

$$\mathbf{B} = \boldsymbol{\mathcal{F}}_{2D} \cdot \boldsymbol{\mathcal{A}} \cdot \mathcal{F}_{3D}^{-1}, \tag{6.19}$$

where $\boldsymbol{\mathcal{F}}_{2D}$ represents an $n_z \times n_z$ diagonal matrix with elements 2D Fourier transformation operators $\mathcal{F}_{2D}$, $\boldsymbol{\mathcal{A}}$ is a block diagonal matrix with $n_p \times n_p$ submatrices $\mathbf{A}_z$, beam pattern for the redshift z, and $\mathcal{F}_{3D}$ represents the 3D Fourier transformation. The interferometer pattern is represented by a block diagonal matrix, $\boldsymbol{\mathcal{I}}_{3D}$, with $n_p \times n_p$ submatrices $\boldsymbol{\mathcal{I}}_z$. In order to extract BAO information from the 3D power spectrum, the data should be defined in terms of co-moving distances, in which case the field of view of the instrument describes a truncated signal pyramid. Since a sufficiently small primary beam tapers the

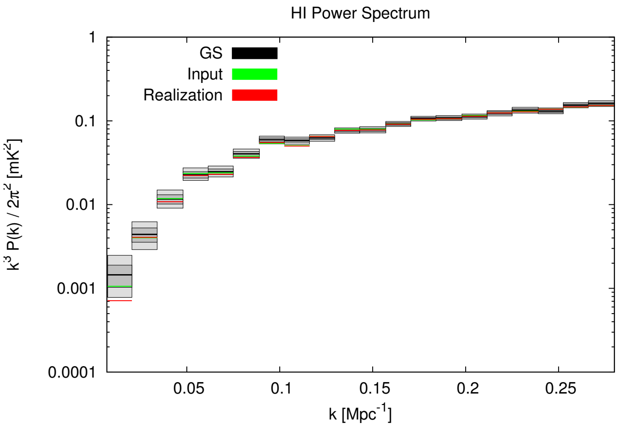

Figure 6.1: 3D power spectrum result from Gibbs sampling analysis of data obtained by a simulation of an interferometric observation of $1146 \times 1146 \times 561$ Mpc^3 HI emission-line signal block of resolution 64^3 pixels without foregrounds. The observation is simulated for an interferometer with complete uv-coverage and a maximum beam size of FWHM$_{\nu=855MHz}$ = 5.3° observing the redshift range of 855-955 MHz with a signal-to-noise ratio of 10. Mean posterior power spectra for each k-bin are shown in black. Dark and light grey indicate 1 and 2 σ uncertainties, respectively. The binned power spectra of the signal realization and the binned input power spectrum are shown in red and green, respectively.

signal at the edges, we can embed the signal into a zero-padded cubic region. We have generalized the CMB code to 3D 21 cm data and shown power spectrum inference for the mock data obtained by a simulation of an interferometric observation of $1146 \times 1146 \times 561$ Mpc^3 HI emission-line signal block of resolution 64^3 pixels without foregrounds in Fig. 6.1. The observation is simulated for an interferometer with complete uv-coverage and a maximum beam size of FWHM$_{\nu=855MHz} = 5.3$ degrees observing the redshift range of 855-955 MHz with a signal-to-noise ratio of 10.

This is, of course, only a first approach. Our analysis must be extended to include realistic scan strategies covering areas much larger than a single primary beam where individual pointings cannot be treated in the flat-sky approximation.

A major challenge in HI tomography is that the synchrotron foregrounds are expected to be orders of magnitude stronger than the 21 cm signal. Any analysis method must, therefore, include an efficient foreground removal technique. The component separation can be achieved by using the dissimilarities between the expected redshift dependent behaviors of the signal and the foregrounds; the 21 cm spectrum varies abruptly with frequency because of the cosmic structure whereas the foreground spectrum varies smoothly. Our method must be extended to include a Bayesian inference technique to distinguish the much weaker cosmic signal from the smoothly changing foreground components. Semi-blind Bayesian foreground rejection methods can be promising approaches for such programs [70, 75].

Chapter 7

Conclusions

Observations of the CMB polarization signal can provide valuable information about the early universe, in particular about the inflationary epoch, and place stringent constraints on the cosmological parameters. In comparison to alternative methods of extracting power spectra, such as maximum likelihood and pseudo-C_l estimators, which often scale as $O(n^3)$ and $O(n^{3/2})$ respectively, the method of Gibbs sampling has an advantage in dealing with the demands of current and future high resolution cosmology observations because it provides simultaneous inference of power spectrum and signal with $O(n^{3/2})$ computational complexity.

The detection of the primordial B-mode spectrum of the polarized CMB signal may provide a probe of inflation. However, observation of such a faint signal requires excellent control of systematic errors. Interferometry proves to be a promising approach for overcoming such a challenge.

We have investigated the method of Gibbs sampling as applied to interferometric polarimetry. The extension of Gibbs sampling to interferometric observations of polarized signals has been successfully demonstrated. An example of signal reconstruction and inference of CMB power spectra from a moderately large ($n_p = 64^2$) mock data set has been provided. The validity of our technique in dealing with realistic interferometric data, including an incomplete uv-plane coverage, finite beam size and baseline-dependent noise, has been shown.

We have developed a complete pipeline of simulations to diagnose the effects of systematic errors on the CMB polarization power spectra obtained by an interferometric observation. We have simulated a realistic, QUBIC-like interferometer design with systematics that incorporate the effects of sky-rotation. We have analyzed the mock data sets by both the maximum likelihood method and the method of Gibbs sampling. The results from both methods have been found to be consistent with each other, as well as with the analytical estimations within a factor of 6.

In order to assess the level at which systematic effects must be controlled, we chose a tolerance level of $\alpha_r = 0.1$. This ensures that the instrument is sensitive enough to detect the B-signal at $r = 0.01$ level. We saw that, for a QUBIC-like experiment, the contamination of the tensor-to-scalar ratio at $r = 0.01$ does not exceed the 10% tolerance level in the multipole range $28 < \ell < 384$ when the Gaussian-distributed systematic errors are controlled with precisions of $|g_{rms}| = 0.1$ for antenna gain, $|\epsilon_{rms}| = 5\times10^{-4}$ for antenna coupling, $\delta_{rms} \approx 0.7^\circ$ for pointing, $\zeta_{rms} \approx 0.7^\circ$ for beam shape, and $\mu_{rms} = 5 \times 10^{-4}$ for beam cross-polarization when each error acts individually. However, in a realistic experiment all the systematic errors are simultaneously present, in which case the tolerance parameter of r roughly reaches the 20% level for the linear experiment and 15% for the circular experiment. Although this suggests that better control of systematics would be needed for a linear experiment, for a QUBIC-like experiment with circular polarizers, bias in r induced by combined systematic errors would still be on the acceptable level when the systematics are controlled with the given precisions.

Apart from the systematics presented in the work, we also ran simulations to analyze the effects of uncertainties in the positions of the antennas. In order to have an effect on the order of $\alpha^{BB} = 0.1$, we found that the uncertainty in the position of each antenna should be on the order of 50% of the size of the uv-plane. Since such an error is unrealistically large, we conclude that the effect of antenna position errors on power spectra is negligible in an interferometric observation of the CMB polarization.

We have shown that a QUBIC-like experiment has fairly manageable systematics, which is essential for the detection of primordial B-modes. Since our interferometer design has a large number of redundant baselines (approximately 10 baselines per visibility), as a further improvement, a self-calibration technique can be employed to significantly reduce the level of instrumental errors.

A major systematic effect in observations of the CMB signal is noncosmological foregrounds. Any analysis method must include a foreground removal strategy. We have developed a Bayesian component separation technique built into the Gibbs sampler. The technique should be implemented for interferometric observations and tested with simulated data.

In dealing with the real data, our methods must be extended to spherical harmonic basis to accommodate the curvature of the observed sky patch. Also, mixing of E and B modes caused by the incomplete sky coverage must be resolved.

HI tomography is one of the next frontiers of observational cosmology. Observations of the redshifted 21 cm emission line of the hyperfine transition of neutral hydrogen can give a detailed picture of the evolution of structure in the universe over a range of redshifts. We have shown that the Gibbs sampling method naturally extends to the 3D power spectrum inference from interferometric data of 21 cm signal. However, foreground signals are generally orders of magnitude brighter than the cosmic signal and the relevant cosmological information demands observations of large areas on the celestial sphere. Therefore, our analysis must be extended to include efficient foreground separation methods and realistic scan strategies covering large areas on the celestial sphere where the flat-sky approximation is no longer valid.

Appendix A

Analytical Estimations of Systematics-Induced Biases in Power Spectra

Following [29], we obtain first order approximations for the $\Delta\hat{C}^{XY}_{rms}$ given, for a single baseline, in Eq. (3.24). For a baseline lying on the x-axis, the matrices in Eq. (3.26) are given as

$$
\begin{aligned}
\mathbf{N}_{TT} = \begin{pmatrix} 1 & 0 & 0 \\ 0 & 0 & 0 \\ 0 & 0 & 0 \end{pmatrix}, \quad \mathbf{N}_{TE} = \frac{1}{2\overline{c}} \begin{pmatrix} 0 & 1 & 0 \\ 1 & 0 & 0 \\ 0 & 0 & 0 \end{pmatrix}, \\
\mathbf{N}_{EE} = \left[\left(\overline{c^2}\right)^2 - \left(\overline{s^2}\right)^2\right]^{-1} \begin{pmatrix} 0 & 0 & 0 \\ 0 & \overline{c^2} & 0 \\ 0 & 0 & -\overline{s^2} \end{pmatrix}, \\
\mathbf{N}_{BB} = \left[\left(\overline{c^2}\right)^2 - \left(\overline{s^2}\right)^2\right]^{-1} \begin{pmatrix} 0 & 0 & 0 \\ 0 & -\overline{s^2} & 0 \\ 0 & 0 & \overline{c^2} \end{pmatrix}, \\
\mathbf{N}_{TB} = \frac{1}{2\overline{c}} \begin{pmatrix} 0 & 0 & 1 \\ 0 & 0 & 0 \\ 1 & 0 & 0 \end{pmatrix}, \quad \mathbf{N}_{EB} = \frac{1}{2(\overline{c^2} - \overline{s^2})} \begin{pmatrix} 0 & 0 & 0 \\ 0 & 0 & 1 \\ 0 & 1 & 0 \end{pmatrix}.
\end{aligned}
\tag{A.1}
$$

The covariance matrix (3.29) can be written in block-matrix form as $\boldsymbol{\mathcal{M}}_w = \begin{pmatrix} \mathbf{M} & \mathbf{M}_1 \\ \mathbf{M}_1^\dagger & \mathbf{M}_2 \end{pmatrix}$ where

$$\mathbf{M} = \begin{pmatrix} C^{TT} & C^{TE}\overline{c} & C^{TB}\overline{c} \\ C^{TE}\overline{c} & C^{EE}\overline{c^2} + C^{BB}\overline{s^2} & C^{EB}(\overline{c^2} - \overline{s^2}) \\ C^{TB}\overline{c} & C^{EB}(\overline{c^2} - \overline{s^2}) & C^{EE}\overline{s^2} + C^{BB}\overline{c^2} \end{pmatrix}. \tag{A.2}$$

A.1 Gain Errors

$$g_1 = \frac{1}{2}(g_1^i + g_2^i + g_1^{j*} + g_2^{j*}),\ g_2 = \frac{1}{2}(g_1^i - g_2^i + g_1^{j*} - g_2^{j*}) \tag{A.3}$$

For instrumental errors we can write $\delta\mathbf{v} = \mathbf{E}\cdot\mathbf{v}$, which gives $\mathbf{M}_1 = \mathbf{M}\cdot\mathbf{E}^\dagger$ and $\mathbf{M}_2 = \mathbf{E}\cdot\mathbf{M}\cdot\mathbf{E}^\dagger$.

A.1.1 Linear Basis

$$\gamma_1 = \frac{1}{2}(g_1^Q + g_1^U),\ \gamma_2 = \frac{1}{2}(g_1^Q - g_1^U),\ \gamma_3 = \frac{1}{2}(g_2^Q + g_2^U), \tag{A.4}$$

$$\mathbf{E}^{gain}_{linear} = \begin{pmatrix} \gamma_1 & \gamma_3 & 0 \\ 0 & \gamma_1 + \gamma_2 & 0 \\ 0 & 0 & \gamma_1 - \gamma_2 \end{pmatrix} \tag{A.5}$$

$$\begin{aligned}
(\Delta\hat{C}^{TT}_{rms})^2 &= 8Re\{\gamma_1\}^2(C^{TT})^2 \\
(\Delta\hat{C}^{TE}_{rms})^2 &= (6Re\{\gamma_1\}^2 + \frac{3}{4}Re\{\gamma_2\}^2 - \frac{1}{4}Im\{\gamma_2\}^2)(C^{TE})^2 \\
&\quad + (2Re\{\gamma_1\}^2 + \frac{1}{4}|\gamma_2|^2)C^{TT}C^{EE} \\
(\Delta\hat{C}^{EE}_{rms})^2 &= (8Re\{\gamma_1\}^2 + 4Re\{\gamma_2\}^2)(C^{EE})^2 \\
(\Delta\hat{C}^{BB}_{rms})^2 &= \overline{s^2}|\gamma_2|^2(C^{EE})^2 \\
(\Delta\hat{C}^{TB}_{rms})^2 &= \frac{1}{4}(3Re\{\gamma_2\}^2 - Im\{\gamma_2\}^2)(C^{TE})^2 + \frac{1}{4}(|\gamma_2|^2 + 8Re\{\gamma_1\}^2)C^{TT}C^{EE} \\
(\Delta\hat{C}^{EB}_{rms})^2 &= Re\{\gamma_2\}^2(C^{EE})^2 + (|\gamma_2|^2 + 2Re\{\gamma_1\}^2)C^{EE}C^{BB}
\end{aligned} \tag{A.6}$$

A.1.2 Circular Basis

$$\mathbf{E}^{gain}_{circular} = \begin{pmatrix} g_1 & 0 & 0 \\ 0 & g_1 & ig_2 \\ 0 & -ig_2 & g_1 \end{pmatrix} \tag{A.7}$$

$$\begin{aligned}
(\Delta\hat{C}^{TT}_{rms})^2 &= 8Re\{g_1\}^2(C^{TT})^2 \\
(\Delta\hat{C}^{TE}_{rms})^2 &= 6Re\{g_1\}^2(C^{TE})^2 + 2Re\{g_1\}^2C^{TT}C^{EE} \\
(\Delta\hat{C}^{EE}_{rms})^2 &= 8Re\{g_1\}^2(C^{EE})^2 \\
(\Delta\hat{C}^{BB}_{rms})^2 &= 2|g_2|^2C^{EE}(C^{BB} + \overline{s^2}C^{EE}) \\
(\Delta\hat{C}^{TB}_{rms})^2 &= (\frac{3}{2}Im\{g_2\}^2 - \frac{1}{2}Re\{g_2\}^2)(C^{TE})^2 + \frac{1}{2}|g_2|^2C^{TT}C^{EE} \\
(\Delta\hat{C}^{EB}_{rms})^2 &= 2Im\{g_2\}^2(C^{EE})^2
\end{aligned} \tag{A.8}$$

A.2 Coupling Errors

$$e_1 = \frac{1}{2}(e^i_1 + e^i_2 + e^{j*}_1 + e^{j*}_2),\ e_2 = \frac{1}{2}(e^i_1 - e^i_2 - e^{j*}_1 + e^{j*}_2) \tag{A.9}$$

A.2.1 Linear Basis

$$\epsilon_1 = \frac{1}{2}(e^Q_1 + e^U_1),\ \epsilon_2 = \frac{1}{2}(e^Q_1 - e^U_1),\ \epsilon_3 = \frac{1}{2}(e^Q_2 + e^U_2),\ \epsilon_4 = \frac{1}{2}(e^Q_2 - e^U_2), \tag{A.10}$$

$$\mathbf{E}^{coupling}_{linear} = \begin{pmatrix} 0 & 0 & \epsilon_1 \\ \epsilon_1 + \epsilon_2 & 0 & -\epsilon_3 - \epsilon_4 \\ \epsilon_1 - \epsilon_2 & \epsilon_3 - \epsilon_4 & 0 \end{pmatrix} \tag{A.11}$$

$$\begin{aligned}
(\Delta\hat{C}^{TT}_{rms})^2 &= (3Re\{\epsilon_1\}^2 - Im\{\epsilon_1\}^2)(C^{TE})^2 + |\epsilon_1|^2 C^{TT}C^{EE} \\
(\Delta\hat{C}^{TE}_{rms})^2 &= 2(Re\{\epsilon_1\}^2 + Re\{\epsilon_2\}^2)(C^{TT})^2 \\
(\Delta\hat{C}^{EE}_{rms})^2 &= 2(|\epsilon_1|^2 + |\epsilon_2|^2)C^{TT}C^{EE} \\
(\Delta\hat{C}^{BB}_{rms})^2 &= 2(|\epsilon_1|^2 + |\epsilon_2|^2)C^{TT}C^{BB} + 2\overline{s^2}(|\epsilon_1|^2 + |\epsilon_2|^2)C^{TT}C^{EE} \\
(\Delta\hat{C}^{TB}_{rms})^2 &= 2(Re\{\epsilon_1\}^2 + Re\{\epsilon_2\}^2)(C^{TT})^2 \\
(\Delta\hat{C}^{EB}_{rms})^2 &= \frac{1}{2}(|\epsilon_1|^2 + |\epsilon_2|^2)C^{TT}C^{EE} \\
&\quad + \frac{1}{2}(3Re\{\epsilon_1\}^2 + 3Re\{\epsilon_2\}^2 - Im\{\epsilon_1\}^2 - Im\{\epsilon_2\}^2)(C^{TE})^2
\end{aligned} \tag{A.12}$$

A.2.2 Circular Basis

$$\mathbf{E}^{coupling}_{circular} = \begin{pmatrix} 0 & e_1 & ie_2 \\ e_1 & 0 & 0 \\ ie_2 & 0 & 0 \end{pmatrix} \tag{A.13}$$

$$\begin{aligned}
(\Delta\hat{C}^{TT}_{rms})^2 &= (3Re\{e_1\}^2 - Im\{e_1\}^2 + 2Im\{e_2\}^2)(C^{TE})^2 \\
&\quad + (|e_1|^2 + |e_2|^2)C^{TT}C^{EE} \\
(\Delta\hat{C}^{TE}_{rms})^2 &= (Re\{e_1\}^2 + Im\{e_2\}^2)((C^{TT})^2 + (C^{TE})^2 + C^{TT}C^{EE}) \\
(\Delta\hat{C}^{EE}_{rms})^2 &= (3Re\{e_1\}^2 - Im\{e_1\}^2 + 2Im\{e_2\}^2)(C^{TE})^2 \\
&\quad + (|e_1|^2 + |e_2|^2)C^{TT}C^{EE} \\
(\Delta\hat{C}^{BB}_{rms})^2 &= (|e_1|^2 + |e_2|^2)C^{TT}(C^{BB} + \overline{s^2}C^{EE}) \\
(\Delta\hat{C}^{TB}_{rms})^2 &= (Re\{e_1\}^2 + Im\{e_2\}^2)(C^{TT})^2 \\
(\Delta\hat{C}^{EB}_{rms})^2 &= \frac{1}{4}(|e_1|^2 + |e_2|^2)C^{TT}C^{EE} + \frac{1}{4}(3Re\{e_1\}^2 \\
&\quad + 3Im\{e_2\}^2 - Im\{e_1\}^2 - Re\{e_2\}^2)(C^{TE})^2
\end{aligned} \tag{A.14}$$

A.3 Pointing Errors

Defining $\delta\hat{\mathbf{r}}_k$ as the deviation of the k^{th} antenna's pointing center, we can write, to the first order,

$$A^j(\hat{\mathbf{r}})A^k(\hat{\mathbf{r}}) = \exp[-(\hat{\mathbf{r}} - \sigma\boldsymbol{\delta})^2/2\sigma^2], \tag{A.15}$$

where $\boldsymbol{\delta} = (\delta\hat{\mathbf{r}}_j + \delta\hat{\mathbf{r}}_k)/2\sigma$.

$$\delta V_S = -i\sigma \int d^2\mathbf{k}\tilde{S}(\mathbf{k})[\tilde{A_0^2}(\mathbf{k} - 2\pi\mathbf{u})]^*[(\mathbf{k} - 2\pi\mathbf{u}) \cdot \boldsymbol{\delta}_S] \tag{A.16}$$

$$\langle V_X \delta V_Y^* \rangle = 0 \textit{ and } \langle \delta V_X \delta V_Y^* \rangle = \frac{1}{2}(\boldsymbol{\delta}_X \cdot \boldsymbol{\delta}_Y) \langle V_X V_Y^* \rangle . \tag{A.17}$$

A.3.1 Linear Basis

$$\boldsymbol{\delta}_1 = \frac{1}{2}(\boldsymbol{\delta}_Q + \boldsymbol{\delta}_U), \quad \boldsymbol{\delta}_2 = \frac{1}{2}(\boldsymbol{\delta}_Q - \boldsymbol{\delta}_U) \tag{A.18}$$

$$\begin{aligned}
(\Delta\hat{C}^{TT}_{rms})^2 &= |\boldsymbol{\delta}_1|^2(C^{TT})^2 \\
(\Delta\hat{C}^{TE}_{rms})^2 &= \frac{1}{2}|\boldsymbol{\delta}_1|^2(C^{TE})^2 + \frac{1}{8}(4|\boldsymbol{\delta}_1|^2 + |\boldsymbol{\delta}_2|^2)C^{TT}C^{EE} \\
(\Delta\hat{C}^{EE}_{rms})^2 &= (|\boldsymbol{\delta}_1|^2 + \frac{1}{2}|\boldsymbol{\delta}_2|^2)(C^{EE})^2 \\
(\Delta\hat{C}^{BB}_{rms})^2 &= |\boldsymbol{\delta}_1|^2C^{BB}(C^{BB} + 2\overline{s^2}C^{EE}) + \frac{1}{2}|\boldsymbol{\delta}_2|^2C^{EE}(C^{BB} + \overline{s^2}C^{EE}) \\
(\Delta\hat{C}^{TB}_{rms})^2 &= \frac{1}{2}|\boldsymbol{\delta}_1|^2C^{TT}(C^{BB} + \overline{s^2}C^{EE}) + \frac{1}{8}|\boldsymbol{\delta}_2|^2C^{TT}C^{EE} \\
(\Delta\hat{C}^{EB}_{rms})^2 &= \frac{1}{2}|\boldsymbol{\delta}_1|^2C^{EE}(C^{BB} + \overline{s^2}C^{EE}) + \frac{1}{8}|\boldsymbol{\delta}_2|^2(C^{EE})^2
\end{aligned} \tag{A.19}$$

A.3.2 Circular Basis

$$\boldsymbol{\delta}_2 = 0. \tag{A.20}$$

A.4 Shape Errors

The product of two elliptic Gaussian beams can be written as a single elliptic Gaussian:

$$A^j(\hat{\mathbf{r}})A^k(\hat{\mathbf{r}}) = \exp\left[-\frac{(x\cos\beta + y\sin\beta)^2}{2(\sigma + \sigma_x)^2} - \frac{(y\cos\beta - x\sin\beta)^2}{2(\sigma + \sigma_y)^2}\right], \tag{A.21}$$

where β is the angle between the major axis of the resulting ellipse and the x-axis.

$$\delta V_S = -\frac{1}{\sigma^2}\int d^2\mathbf{k}\tilde{S}(\mathbf{k})[(\widetilde{A_0^2\Delta_S})(\mathbf{k}-2\pi\mathbf{u})]^* \tag{A.22}$$

where $\Delta_S(x,y) = x^2(\zeta_x^S\cos^2\beta + \zeta_y^S\sin^2\beta) + y^2(\zeta_y^S\cos^2\beta + \zeta_x^S\sin^2\beta) + xy(\zeta_x^S - \zeta_y^S)\sin 2\beta$, and $\zeta_{x,y}^S = \sigma_{x,y}^S/\sigma$. The only non-vanishing integrals in the covariance matrix are:

$$\begin{aligned}\int |\tilde{A}^2|^2 &= \pi\sigma^2,\\ \int |\widetilde{x^2A^2}|^2 = \int |\widetilde{y^2A^2}|^2 &= \frac{3}{4}\pi\sigma^6,\\ \int \tilde{A}^2(\widetilde{x^2A^2})^* = \int \tilde{A}^2(\widetilde{y^2A^2})^* &= \frac{1}{2}\pi\sigma^4,\\ \int (\widetilde{x^2A^2})(\widetilde{y^2A^2})^* = \int |\widetilde{xyA^2}|^2 &= \frac{1}{4}\pi\sigma^6.\end{aligned} \tag{A.23}$$

$$\zeta_1^S = \frac{1}{2}(\zeta_x^S + \zeta_y^S),\ \zeta_2^S = \frac{1}{2}(\zeta_x^S - \zeta_y^S);\quad \zeta_{i+} = \frac{1}{2}(\zeta_i^Q + \zeta_i^U),\ \zeta_{i-} = \frac{1}{2}(\zeta_i^Q - \zeta_i^U). \tag{A.24}$$

Averaging over β we get

$$\langle V_X\delta V_Y^*\rangle = -\zeta_1^Y\langle V_XV_Y^*\rangle \ \textit{and}\ \langle\delta V_X\delta V_Y^*\rangle = (2\zeta_1^X\zeta_1^Y + \zeta_2^X\zeta_2^Y)\langle V_XV_Y^*\rangle. \tag{A.25}$$

A.4.1 Linear Basis

$$\begin{aligned}(\Delta\hat{C}_{rms}^{TT})^2 &= (10\zeta_{1+}^2 + 2\zeta_{2+}^2)(C^{TT})^2\\ (\Delta\hat{C}_{rms}^{TE})^2 &= (7\zeta_{1+}^2 + \frac{3}{4}\zeta_{1-}^2 + \zeta_{2+}^2)(C^{TE})^2\\ &\quad + (3\zeta_{1+}^2 + \frac{1}{2}\zeta_{1-}^2 + \zeta_{2+}^2 + \frac{1}{4}\zeta_{2-}^2)C^{TT}C^{EE}\\ (\Delta\hat{C}_{rms}^{EE})^2 &= (10\zeta_{1+}^2 + 5\zeta_{1-}^2 + 2\zeta_{2+}^2 + \zeta_{2-}^2)(C^{EE})^2\\ (\Delta\hat{C}_{rms}^{BB})^2 &= (2\zeta_{1-}^2 + \zeta_{2-}^2)\overline{s^2}(C^{EE})^2\\ &\quad + (12\zeta_{1+}^2 + 12\zeta_{1-}^2 + 4\zeta_{2+}^2 + \zeta_{2-}^2)\overline{s^2}C^{EE}C^{BB}\\ &\quad + (10\zeta_{1+}^2 + 5\zeta_{1-}^2 + 2\zeta_{2+}^2 + \zeta_{2-}^2)(C^{BB})^2\\ (\Delta\hat{C}_{rms}^{TB})^2 &= \frac{3}{4}\zeta_{1-}^2(C^{TE})^2 + \frac{1}{4}(2\zeta_{1-}^2 + \zeta_{2-}^2)C^{TT}C^{EE}\\ &\quad + (3\zeta_{1+}^2 + \frac{1}{2}\zeta_{1-}^2 + \zeta_{2+}^2 + \frac{1}{4}\zeta_{2-}^2)\overline{s^2}C^{TT}C^{EE}\\ (\Delta\hat{C}_{rms}^{EB})^2 &= (\frac{5}{4}\zeta_{1-}^2 + \frac{1}{4}\zeta_{2-}^2 + \overline{s^2}(3\zeta_{1+}^2 + \zeta_{2+}^2))(C^{EE})^2\end{aligned} \tag{A.26}$$

A.4.2 Circular Basis

$$\zeta_{i-} = 0. \tag{A.27}$$

A.5 Cross-Polarization

The only non-vanishing integrals in the covariance matrix are:

$$\int |\tilde{A^2}|^2 = \pi\sigma^2, \quad \int |A^2 \widetilde{\rho^2 \cos 2\phi}|^2 = \int |A^2 \widetilde{\rho^2 \sin 2\phi}|^2 = \pi\sigma^6. \tag{A.28}$$

A.5.1 Linear Basis

$$\mu_1 = \frac{1}{2}(\mu^Q + \mu^U), \quad \mu_2 = \frac{1}{2}(\mu^Q - \mu^U) \tag{A.29}$$

$$\begin{aligned} \delta I &= \mu_1 \frac{\rho^2}{\sigma^2}(Q\cos 2\phi + U \sin 2\phi), \\ \delta Q &= (\mu_1 + \mu_2)\frac{\rho^2}{\sigma^2} I \cos 2\phi, \\ \delta U &= (\mu_1 - \mu_2)\frac{\rho^2}{\sigma^2} I \sin 2\phi \end{aligned} \tag{A.30}$$

$$\begin{aligned} (\Delta \hat{C}^{TT}_{rms})^2 &= 2\mu_1^2 C^{TT} C^{EE} \\ (\Delta \hat{C}^{TE}_{rms})^2 &= \frac{1}{2}(\mu_1^2 + \mu_2^2)(C^{TT})^2 \\ (\Delta \hat{C}^{EE}_{rms})^2 &= 2(\mu_1^2 + \mu_2^2) C^{TT} C^{EE} \\ (\Delta \hat{C}^{BB}_{rms})^2 &= 2(\mu_1^2 + \mu_2^2) C^{TT} (C^{BB} + \overline{s^2} C^{EE}) \\ (\Delta \hat{C}^{TB}_{rms})^2 &= \frac{1}{2}(\mu_1^2 + \mu_2^2)(C^{TT})^2 \\ (\Delta \hat{C}^{EB}_{rms})^2 &= \frac{1}{2}(\mu_1^2 + \mu_2^2) C^{TT} C^{EE} \end{aligned} \tag{A.31}$$

A.5.2 Circular Basis

$$\mu_+ = \frac{1}{2}(\mu^i + \mu^j), \quad \mu_- = \frac{1}{2}(\mu^i - \mu^j) \tag{A.32}$$

$$\begin{aligned} \delta I &= \mu_+ \frac{\rho^2}{\sigma^2} Q \sin 2\phi, \\ \delta Q &= \mu_+ \frac{\rho^2}{\sigma^2} I \sin 2\phi + i\mu_- \frac{\rho^2}{\sigma^2} U \cos 2\phi, \\ \delta U &= -i\mu_- \frac{\rho^2}{\sigma^2} Q \cos 2\phi \end{aligned} \tag{A.33}$$

$$
\begin{aligned}
(\Delta\hat{C}^{TT}_{rms})^2 &= \mu_+^2 C^{TT} C^{EE} \\
(\Delta\hat{C}^{TE}_{rms})^2 &= \frac{1}{4}\mu_+^2 (C^{TT})^2 \\
(\Delta\hat{C}^{EE}_{rms})^2 &= (\mu_+^2 C^{TT} - 2\mu_-^2 C^{EE}) C^{EE} \\
(\Delta\hat{C}^{BB}_{rms})^2 &= (\mu_+^2 C^{TT} - 2\mu_-^2 C^{EE})(C^{BB} + \overline{s^2} C^{EE}) \\
(\Delta\hat{C}^{TB}_{rms})^2 &= \frac{1}{4}(\mu_+^2 C^{TT} - 2\mu_-^2 C^{EE}) C^{TT} \\
(\Delta\hat{C}^{EB}_{rms})^2 &= \frac{1}{4}(\mu_+^2 C^{TT} - 2\mu_-^2 C^{EE}) C^{EE}
\end{aligned}
\tag{A.34}
$$

Appendix B

Gelman-Rubin Convergence Diagnostic

Gelman-Rubin diagnostics monitor the convergence of Markov chain Monte Carlo (MCMC) algorithms by comparing inferences made from several independently sampled sequences with different starting points [20]. Multiple instances of chains are simulated in parallel and first n_{burn} iterations of each chain are discarded for a burn-in phase. To determine that the stationary distribution of the Markov chain is reached we can employ the *Geweke test*, which compares the first and last 10% of the samples after the burn-in phase. If the mean of the subsamples is still drifting, then a larger number of steps is required for the burn-in phase.

After the burn-in phase, each chain is run for n samples and inferences of sample mean and variance of each chain are made. If approximate convergence has been reached, these independent inferences must be similar enough. Assuming that m instances of chains are simulated, these m inferences are compared to the inference made for the entire collection of mn samples. Denoting the i^{th} sample of the κ^{th} chain by $x_{\kappa i}$, we can calculate the between-sequence variance B/n, and the within-sequence variance W by

$$B/n = \frac{1}{m-1}\sum_{\kappa=1}^{m}(\mu_\kappa - \mu)^2, \tag{B.1a}$$

$$W = \frac{1}{m(n-1)}\sum_{\kappa=1}^{m}\sum_{i=1}^{n}(x_{\kappa i} - \mu_\kappa)^2, \tag{B.1b}$$

where μ_κ is the mean of the κ^{th} chain and μ is the mean of the entire collection samples.

An unbiased estimate of the true variance σ^2 can be made by a weighted average of B and W:

$$\hat{V} = \frac{n-1}{n} W + \frac{m+1}{mn} B. \tag{B.2}$$

The comparison of pooled posterior variance estimate $\hat{V}$, and within-sequence variance is given by the *potential scale reduction factor*:

$$\mathcal{R} = \sqrt{\frac{\hat{V}}{W}}. \tag{B.3}$$

If $\mathcal{R}$ is close to unity inferences from independent chains are close enough to conclude that the convergence is reached. A value of $1.1 \leq \mathcal{R} \leq 1.2$ is generally considered to be an acceptable measure of convergence [20].

Appendix C

Mode Mixing

The spherical harmonics form a complete orthonormal basis on the whole sphere and the polarization field can be uniquely decomposed into E and B modes. However, on a patch of cut sphere the $E-B$ decomposition is not unique [42, 6]. The non-uniqueness of the decomposition causes a confusion of E and B signals. The net result appears as the leakage of much stronger E mode signal into the B modes. The spherical harmonic expansion of Eq. (2.17) and spin-2 harmonic expansion of Eq. (2.16) can be rearranged as

$$\bar{a}_{E,\ell m} = \sum_{\ell',m'} (a_{E,\ell'm'} W_{+(\ell m)(\ell'm')} + i a_{B,\ell'm'} W_{-(\ell m)(\ell'm')}), \tag{C.1a}$$

$$\bar{a}_{B,\ell m} = \sum_{\ell',m'} (a_{B,\ell'm'} W_{+(\ell m)(\ell'm')} - i a_{E,\ell'm'} W_{-(\ell m)(\ell'm')}), \tag{C.1b}$$

where

$$W_{\pm(\ell m)(\ell'm')} \equiv \frac{1}{2}({}_2W_{(\ell m)(\ell'm')} \pm {}_{-2}W_{(\ell m)(\ell'm')}), \tag{C.2a}$$

$${}_sW_{(\ell m)(\ell'm')} \equiv \int_{\mathcal{S}} {}_sY^*_{\ell m} {}_sY_{\ell'm'} d\Omega. \tag{C.2b}$$

Over the complete sphere $\mathcal{S} \to S^2$ and ${}_{\pm 2}W_{(\ell m)(\ell'm')}$ become projection operators [42].

In order to separate the pure E and B mode signals, we write Eq. (C.1) in matrix form as

$$\bar{\mathbf{E}} = \mathbf{W}_+\mathbf{E} + i\mathbf{W}_-\mathbf{B}, \quad \bar{\mathbf{B}} = \mathbf{W}_+\mathbf{B} - i\mathbf{W}_-\mathbf{E}. \tag{C.3}$$

The components of $\mathbf{W}_+\mathbf{B}$ that correspond to very small eigenvalues of $\mathbf{W}_+$ are poorly determined by $\bar{\mathbf{B}}$. Since they represent polarization patterns whose support is outside of the observed region, they generate ambiguous polarization modes. In order to remove these components, we diagonalize $\mathbf{W}_+ = \mathbf{Q}_+\mathbf{D}_+\mathbf{Q}_+^\dagger$ and define a truncated operator $\tilde{\mathbf{Q}}_+$ by removing the columns of $\mathbf{Q}_+$ corresponding to the eigenvalues $\ll 1$ of $\mathbf{W}_+$. Since $\mathbf{Q}_+$ is column orthogonal we have $\tilde{\mathbf{Q}}_+^\dagger\tilde{\mathbf{Q}}_+ = \mathbf{I}$ and

$$\tilde{\mathbf{D}}_+^{-1/2}\tilde{\mathbf{Q}}_+^\dagger\bar{\mathbf{B}} \approx \tilde{\mathbf{D}}_+^{1/2}\tilde{\mathbf{Q}}_+^\dagger\mathbf{B} - i\tilde{\mathbf{D}}_+^{-1/2}\tilde{\mathbf{Q}}_+^\dagger\mathbf{W}_-\mathbf{E}, \tag{C.4}$$

where $\tilde{\mathbf{D}}_+$ is the corresponding truncated square diagonal matrix. The factor $\tilde{\mathbf{D}}_+^{-1/2}\tilde{\mathbf{Q}}_+^\dagger$ in Eq. (C.4) ensures that the projection operator is constructed from a reduced basis that is complete and orthonormal over the patch $\mathcal{S}$ [42].

In order to remove the components of $\mathbf{E}$ that contaminate $\bar{\mathbf{B}}$, the range of $\tilde{\mathbf{D}}_+^{-1/2}\tilde{\mathbf{Q}}_+^\dagger\mathbf{W}_-$ must be projected out through the singular value decomposition $\tilde{\mathbf{D}}_+^{-1/2}\tilde{\mathbf{Q}}_+^\dagger\mathbf{W}_- = \mathbf{U}\mathbf{\Sigma}\mathbf{V}^\dagger$. The range can be projected out by including the truncated matrix $\tilde{\mathbf{U}}$, which is constructed by removing the columns of $\mathbf{U}$ corresponding to non-zero singular values, into the definition of the projection operator:

$$\mathbf{\Pi} = \tilde{\mathbf{U}}^\dagger\tilde{\mathbf{D}}_+^{-1/2}\tilde{\mathbf{Q}}_+^\dagger. \tag{C.5}$$

Therefore, the separated pure E and B mode polarization signals become

$$\mathbf{B}_{pure} = \mathbf{\Pi}\cdot\bar{\mathbf{B}} = \tilde{\mathbf{U}}^\dagger\tilde{\mathbf{D}}_+^{-1/2}\tilde{\mathbf{Q}}_+^\dagger\bar{\mathbf{B}} \approx \tilde{\mathbf{U}}^\dagger\tilde{\mathbf{D}}_+^{1/2}\tilde{\mathbf{Q}}_+^\dagger\mathbf{B}, \tag{C.6a}$$

$$\mathbf{E}_{pure} = \mathbf{\Pi}\cdot\bar{\mathbf{E}} = \tilde{\mathbf{U}}^\dagger\tilde{\mathbf{D}}_+^{-1/2}\tilde{\mathbf{Q}}_+^\dagger\bar{\mathbf{E}} \approx \tilde{\mathbf{U}}^\dagger\tilde{\mathbf{D}}_+^{1/2}\tilde{\mathbf{Q}}_+^\dagger\mathbf{E}. \tag{C.6b}$$

The formalism discussed here applies to azimuthally symmetric patches on a sphere. See [6] for a more general treatment of the decomposition of polarizations field into scalar and pseudo-scalar modes on patches of a closed manifold.

Bibliography

[1] R. A. Alpher, H. Bethe, and G. Gamow. The origin of chemical elements. *Phys. Rev.*, 73:803–804, Apr 1948.

[2] R. A. Alpher and R. Herman. Evolution of the Universe. *Nature*, 162:774–775, Nov 1948.

[3] A Avison and S J George. A graphical tool for demonstrating the techniques of radio interferometry. *European Journal of Physics*, 34(1):7, 2013.

[4] C. L. Bennett, M. Halpern, G. Hinshaw, N. Jarosik, A. Kogut, M. Limon, S. S. Meyer, L. Page, D. N. Spergel, G. S. Tucker, E. Wollack, E. L. Wright, C. Barnes, M. R. Greason, R. S. Hill, E. Komatsu, M. R. Nolta, N. Odegard, H. V. Peiris, L. Verde, and J. L. Weiland. First-Year Wilkinson Microwave Anisotropy Probe (WMAP) Observations: Preliminary Maps and Basic Results. *ApJS*, 148:1–27, September 2003.

[5] E. F. Bunn. Systematic errors in cosmic microwave background interferometry. *Phys. Rev. D*, 75(8):083517, April 2007.

[6] E. F. Bunn, M. Zaldarriaga, M. Tegmark, and A. de Oliveira-Costa. E/B decomposition of finite pixelized CMB maps. *Phys. Rev. D*, 67(2):023501, January 2003.

[7] A. Challinor and A. Lewis. Lensed CMB power spectra from all-sky correlation functions. *Phys. Rev. D*, 71(10):103010, May 2005.

[8] CHIME. Canadian hydrogen intensity mapping experiment, 2013. `http://chime.pas.ubc.ca/`.

[9] B. P. Crill, P. A. R. Ade, E. S. Battistelli, S. Benton, R. Bihary, J. J. Bock, J. R. Bond, J. Brevik, S. Bryan, C. R. Contaldi, O. Doré, M. Farhang, L. Fissel, S. R. Golwala, M. Halpern, G. Hilton, W. Holmes, V. V. Hristov, K. Irwin, W. C. Jones, C. L. Kuo, A. E. Lange, C. Lawrie, C. J. MacTavish, T. G. Martin, P. Mason, T. E. Montroy, C. B. Netterfield, E. Pascale, D. Riley, J. E. Ruhl, M. C. Runyan, A. Trangsrud, C. Tucker, A. Turner, M. Viero, and D. Wiebe. SPIDER: a balloon-borne large-scale CMB polarimeter. In *Society of Photo-Optical Instrumentation Engineers (SPIE) Conference Series*, volume 7010 of *Society of Photo-Optical Instrumentation Engineers (SPIE) Conference Series*, August 2008.

[10] C. Dickinson, R. A. Battye, P. Carreira, K. Cleary, R. D. Davies, R. J. Davis, R. Genova-Santos, K. Grainge, C. M. Gutiérrez, Y. A. Hafez, M. P. Hobson, M. E. Jones, R. Kneissl, K. Lancaster, A. Lasenby, J. P. Leahy, K. Maisinger, C. Ödman, G. Pooley, N. Rajguru, R. Rebolo, J. A. Rubiño-Martin, R. D. E. Saunders, R. S. Savage, A. Scaife, P. F. Scott, A. Slosar, P. Sosa Molina, A. C. Taylor, D. Titterington, E. Waldram, R. A. Watson, and A. Wilkinson. High-sensitivity measurements of the cosmic microwave background power spectrum with the extended Very Small Array. *MNRAS*, 353:732–746, September 2004.

[11] D. J. Eisenstein, I. Zehavi, D. W. Hogg, R. Scoccimarro, M. R. Blanton, R. C. Nichol, R. Scranton, H.-J. Seo, M. Tegmark, Z. Zheng, S. F. Anderson, J. Annis, N. Bahcall, J. Brinkmann, S. Burles, F. J. Castander, A. Connolly, I. Csabai, M. Doi, M. Fukugita, J. A. Frieman, K. Glazebrook, J. E. Gunn, J. S. Hendry, G. Hennessy, Z. Ivezić, S. Kent, G. R. Knapp, H. Lin, Y.-S. Loh, R. H. Lupton, B. Margon, T. A. McKay, A. Meiksin, J. A. Munn, A. Pope, M. W. Richmond, D. Schlegel, D. P. Schneider, K. Shimasaku, C. Stoughton, M. A. Strauss, M. SubbaRao, A. S. Szalay,

I. Szapudi, D. L. Tucker, B. Yanny, and D. G. York. Detection of the Baryon Acoustic Peak in the Large-Scale Correlation Function of SDSS Luminous Red Galaxies. *ApJ*, 633:560–574, November 2005.

[12] H. K. Eriksen, C. Dickinson, J. B. Jewell, A. J. Banday, K. M. Górski, and C. R. Lawrence. The Joint Large-Scale Foreground-CMB Posteriors of the 3 Year WMAP Data. *ApJ*, 672:L87–L90, January 2008.

[13] H. K. Eriksen, G. Huey, A. J. Banday, K. M. Górski, J. B. Jewell, I. J. O'Dwyer, and B. D. Wandelt. Bayesian Analysis of the Low-Resolution Polarized 3 Year WMAP Sky Maps. *ApJL*, 665:L1–L4, August 2007.

[14] H. K. Eriksen, G. Huey, R. Saha, F. K. Hansen, J. Dick, A. J. Banday, K. M. Górski, P. Jain, J. B. Jewell, L. Knox, D. L. Larson, I. J. O'Dwyer, T. Souradeep, and B. D. Wandelt. A Reanalysis of the 3 Year Wilkinson Microwave Anisotropy Probe Temperature Power Spectrum and Likelihood. *ApJL*, 656:641–652, February 2007.

[15] H. K. Eriksen, J. B. Jewell, C. Dickinson, A. J. Banday, K. M. Górski, and C. R. Lawrence. Joint Bayesian Component Separation and CMB Power Spectrum Estimation. *ApJ*, 676:10–32, March 2008.

[16] H. K. Eriksen, I. J. O'Dwyer, J. B. Jewell, B. D. Wandelt, D. L. Larson, K. M. Górski, S. Levin, A. J. Banday, and P. B. Lilje. Power Spectrum Estimation from High-Resolution Maps by Gibbs Sampling. *ApJS*, 155:227–241, December 2004.

[17] D. J. Fixsen, E. S. Cheng, J. M. Gales, J. C. Mather, R. A. Shafer, and E. L. Wright. The Cosmic Microwave Background Spectrum from the Full COBE FIRAS Data Set. *ApJ*, 473:576, December 1996.

[18] G. Gamow. Erratum: Expanding universe and the origin of elements [phys. rev. 70, 572-573 (1946)]. *Phys. Rev.*, 71:273–273, Feb 1947.

[19] G. Gamow. On relativistic cosmogony. *Rev. Mod. Phys.*, 21:367–373, Jul 1949.

[20] Andrew Gelman and Donald B. Rubin. Inference from iterative simulation using multiple sequences. *Statistical Science*, 7(4):457–472, 11 1992.

[21] G. Hinshaw, M. R. Nolta, C. L. Bennett, R. Bean, O. Doré, M. R. Greason, M. Halpern, R. S. Hill, N. Jarosik, A. Kogut, E. Komatsu, M. Limon, N. Odegard, S. S. Meyer, L. Page, H. V. Peiris, D. N. Spergel, G. S. Tucker, L. Verde, J. L. Weiland, E. Wollack, and E. L. Wright. Three-Year Wilkinson Microwave Anisotropy Probe (WMAP) Observations: Temperature Analysis. *ApJS*, 170:288–334, June 2007.

[22] M. P. Hobson and K. Maisinger. Maximum-likelihood estimation of the cosmic microwave background power spectrum from interferometer observations. *MNRAS*, 334:569–588, August 2002.

[23] W. Hu, M. M. Hedman, and M. Zaldarriaga. Benchmark parameters for CMB polarization experiments. *Phys. Rev. D*, 67(4):043004, February 2003.

[24] W. Hu and M. White. A CMB polarization primer. *New Astronomy*, 2:323–344, October 1997.

[25] J. Jewell, S. Levin, and C. H. Anderson. Application of Monte Carlo Algorithms to the Bayesian Analysis of the Cosmic Microwave Background. *ApJ*, 609:1–14, July 2004.

[26] M. Kamionkowski, A. Kosowsky, and A. Stebbins. Statistics of cosmic microwave background polarization. *Phys. Rev. D*, 55:7368–7388, June 1997.

[27] J. Kaplan. Polarisation du CMB comme information complémentaire aux anisotropies. *Comptes Rendus Physique*, 4:917–924, October 2003.

[28] A. Karakci, P. M. Sutter, L. Zhang, E. F. Bunn, A. Korotkov, P. Timbie, G. S. Tucker, and B. D. Wandelt. Bayesian Inference of Polarized CMB Power Spectra from Interferometric Data. *Astrophys.J.Suppl.*, 204:8, 2013.

[29] A. Karakci, L. Zhang, P. M. Sutter, E. F. Bunn, A. Korotkov, P. Timbie, G. S. Tucker, and B. D. Wandelt. Systematic Effects in Interferometric Observations of the Cosmic Microwave Background Polarization. *ApJS*, 207:14, July 2013.

[30] B. A. Keating, M. Shimon, and A. P. S. Yadav. Self-calibration of cosmic microwave background polarization experiments. *The Astrophysical Journal Letters*, 762(2):L23, 2013.

[31] B. G. Keating, P. A. R. Ade, J. J. Bock, E. Hivon, W. L. Holzapfel, A. E. Lange, H. Nguyen, and K. W. Yoon. BICEP: a large angular scale CMB polarimeter. In S. Fineschi, editor, *Polarimetry in Astronomy*, volume 4843 of *Society of Photo-Optical Instrumentation Engineers (SPIE) Conference Series*, pages 284–295, February 2003.

[32] A. Kogut, J. Dunkley, C. L. Bennett, O. Doré, B. Gold, M. Halpern, G. Hinshaw, N. Jarosik, E. Komatsu, M. R. Nolta, N. Odegard, L. Page, D. N. Spergel, G. S. Tucker, J. L. Weiland, E. Wollack, and E. L. Wright. Three-Year Wilkinson Microwave Anisotropy Probe (WMAP) Observations: Foreground Polarization. *ApJ*, 665:355–362, August 2007.

[33] A. Kogut, D. N. Spergel, C. Barnes, C. L. Bennett, M. Halpern, G. Hinshaw, N. Jarosik, M. Limon, S. S. Meyer, L. Page, G. S. Tucker, E. Wollack, and E. L. Wright. First-Year Wilkinson Microwave Anisotropy Probe (WMAP) Observations: Temperature-Polarization Correlation. *ApJS*, 148:161–173, September 2003.

[34] E. Komatsu, K. M. Smith, J. Dunkley, C. L. Bennett, B. Gold, G. Hinshaw, N. Jarosik, D. Larson, M. R. Nolta, L. Page, D. N. Spergel, M. Halpern, R. S. Hill,

A. Kogut, M. Limon, S. S. Meyer, N. Odegard, G. S. Tucker, J. L. Weiland, E. Wollack, and E. L. Wright. Seven-year wilkinson microwave anisotropy probe (wmap) observations: Cosmological interpretation. *The Astrophysical Journal Supplement Series*, 192(2):18, 2011.

[35] J. M. Kovac, E. M. Leitch, C. Pryke, J. E. Carlstrom, N. W. Halverson, and W. L. Holzapfel. Detection of polarization in the cosmic microwave background using DASI. *Nature*, 420:772–787, December 2002.

[36] A. Kurek and M. Szydowski. Chasing Lambda. *Nuovo Cimento B Serie*, 122:1359–1364, December 2007.

[37] D. Larson, J. Dunkley, G. Hinshaw, E. Komatsu, M. R. Nolta, C. L. Bennett, B. Gold, M. Halpern, R. S. Hill, N. Jarosik, A. Kogut, M. Limon, S. S. Meyer, N. Odegard, L. Page, K. M. Smith, D. N. Spergel, G. S. Tucker, J. L. Weiland, E. Wollack, and E. L. Wright. Seven-year wilkinson microwave anisotropy probe (wmap) observations: Power spectra and wmap-derived parameters. *The Astrophysical Journal Supplement Series*, 192(2):16, 2011.

[38] D. L. Larson, H. K. Eriksen, B. D. Wandelt, K. M. Grski, Greg Huey, J. B. Jewell, and I. J. ODwyer. Estimation of polarized power spectra by gibbs sampling. *The Astrophysical Journal*, 656(2):653, 2007.

[39] LEDA. The large-aperture experiment to detect the dark ages, 2012. `http://www.cfa.harvard.edu/LEDA/`.

[40] A. T. Lee, P. Ade, A. Balbi, J. Bock, J. Borrill, A. Boscaleri, P. de Bernardis, P. G. Ferreira, S. Hanany, V. V. Hristov, A. H. Jaffe, P. D. Mauskopf, C. B. Netterfield, E. Pascale, B. Rabii, P. L. Richards, G. F. Smoot, R. Stompor, C. D. Winant, and J. H. P. Wu. A High Spatial Resolution Analysis of the MAXIMA-1 Cosmic Microwave Background Anisotropy Data. *ApJL*, 561:L1–L5, November 2001.

[41] A. T. Lee, H. Tran, P. Ade, K. Arnold, J. Borrill, M. A. Dobbs, J. Errard, N. Halverson, W. L. Holzapfel, J. Howard, A. Jaffe, B. Keating, Z. Kermish, E. Linder, N. Miller, M. Myers, A. Niarchou, H. Paar, C. Reichardt, H. Spieler, B. Steinbach, R. Stompor, C. Tucker, E. Quealy, P. L. Richards, and O. Zahn. POLARBEAR: Ultra-high Energy Physics with Measurements of CMB Polarization. In H. Kodama and K. Ioka, editors, *American Institute of Physics Conference Series*, volume 1040 of *American Institute of Physics Conference Series*, pages 66–77, August 2008.

[42] A. Lewis, A. Challinor, and N. Turok. Analysis of CMB polarization on an incomplete sky. *Phys. Rev. D*, 65(2):023505, January 2002.

[43] A. Liu, M. Tegmark, S. Morrison, A. Lutomirski, and M. Zaldarriaga. Precision calibration of radio interferometers using redundant baselines. *MNRAS*, 408:1029–1050, October 2010.

[44] A. Loeb and J. S. B. Wyithe. Possibility of Precise Measurement of the Cosmological Power Spectrum with a Dedicated Survey of 21cm Emission after Reionization. *Physical Review Letters*, 100(16):161301, April 2008.

[45] A. Loeb and M. Zaldarriaga. Measuring the Small-Scale Power Spectrum of Cosmic Density Fluctuations through 21cm Tomography Prior to the Epoch of Structure Formation. *Physical Review Letters*, 92(21):211301, May 2004.

[46] LOFAR. The low-frequency array, 2013. `http://www.lofar.org/`.

[47] J. C. Mather, E. S. Cheng, R. E. Eplee, Jr., R. B. Isaacman, S. S. Meyer, R. A. Shafer, R. Weiss, E. L. Wright, C. L. Bennett, N. W. Boggess, E. Dwek, S. Gulkis, M. G. Hauser, M. Janssen, T. Kelsall, P. M. Lubin, S. H. Moseley, Jr., T. L. Murdock, R. F. Silverberg, G. F. Smoot, and D. T. Wilkinson. A preliminary measurement of the cosmic microwave background spectrum by the Cosmic Background Explorer (COBE) satellite. *ApJL*, 354:L37–L40, May 1990.

[48] A. Miller, J. Beach, S. Bradley, R. Caldwell, H. Chapman, M. J. Devlin, W. B. Dorwart, T. Herbig, D. Jones, G. Monnelly, C. B. Netterfield, M. Nolta, L. A. Page, J. Puchalla, T. Robertson, E. Torbet, H. T. Tran, and W. E. Vinje. The QMAP and MAT/TOCO Experiments for Measuring Anisotropy in the Cosmic Microwave Background. *ApJS*, 140:115–141, June 2002.

[49] N. J. Miller, M. Shimon, and B. G. Keating. Cmb beam systematics: Impact on lensing parameter estimation. *Phys. Rev. D*, 79:063008, Mar 2009.

[50] Planck Mission. 2009. `http://sci.esa.int/planck`.

[51] M. F. Morales and J. S. B. Wyithe. Reionization and Cosmology with 21-cm Fluctuations. *Annual Review of Astronomy and Astrophysics*, 48:127–171, September 2010.

[52] MWA. The murchison wide field array, 2013. `http://www.mwatelescope.org/`.

[53] D. O'Dea, A. Challinor, and B. R. Johnson. Systematic errors in cosmic microwave background polarization measurements. *MNRAS*, 376:1767–1783, April 2007.

[54] I. J. O'Dwyer, H. K. Eriksen, B. D. Wandelt, J. B. Jewell, D. L. Larson, K. M. Górski, A. J. Banday, S. Levin, and P. B. Lilje. Bayesian Power Spectrum Analysis of the First-Year Wilkinson Microwave Anisotropy Probe Data. *ApJL*, 617:L99–L102, December 2004.

[55] S. Padin, M. C. Shepherd, J. K. Cartwright, R. G. Keeney, B. S. Mason, T. J. Pearson, A. C. S. Readhead, W. A. Schaal, J. Sievers, P. S. Udomprasert, J. K. Yamasaki, W. L. Holzapfel, J. E. Carlstrom, M. Joy, S. T. Myers, and A. Otarola. The Cosmic Background Imager. *PASP*, 114:83–97, January 2002.

[56] L. Page, G. Hinshaw, E. Komatsu, M. R. Nolta, D. N. Spergel, C. L. Bennett, C. Barnes, R. Bean, O. Doré, J. Dunkley, M. Halpern, R. S. Hill, N. Jarosik, A. Kogut,

M. Limon, S. S. Meyer, N. Odegard, H. V. Peiris, G. S. Tucker, L. Verde, J. L. Weiland, E. Wollack, and E. L. Wright. Three-Year Wilkinson Microwave Anisotropy Probe (WMAP) Observations: Polarization Analysis. *ApJS*, 170:335–376, June 2007.

[57] PAPER. The precision array for probing the epoch of reionization, 2013. `http://eor.berkeley.edu/`.

[58] C.-G. Park and K.-W. Ng. E/B Separation in Cosmic Microwave Background Interferometry. *ApJ*, 609:15–21, July 2004.

[59] A. A. Penzias and R. W. Wilson. A Measurement of Excess Antenna Temperature at 4080 Mc/s. *ApJ*, 142:419–421, July 1965.

[60] Planck Collaboration, P. A. R. Ade, N. Aghanim, C. Armitage-Caplan, M. Arnaud, M. Ashdown, F. Atrio-Barandela, J. Aumont, C. Baccigalupi, A. J. Banday, and et al. Planck 2013 results. I. Overview of products and scientific results. *ArXiv e-prints*, arXiv:1303.5062, March 2013.

[61] Planck Collaboration, P. A. R. Ade, N. Aghanim, C. Armitage-Caplan, M. Arnaud, M. Ashdown, F. Atrio-Barandela, J. Aumont, C. Baccigalupi, A. J. Banday, and et al. Planck 2013 results. XVI. Cosmological parameters. *ArXiv e-prints*, arXiv:1303.5076, March 2013.

[62] W. H. Press, B. P. Flannery, and S. A. Teukolsky. *Numerical Recipes: The Art of Scientific Computing.* Cambridge University Press, 1986.

[63] Qubic Collaboration, E. Battistelli, A. Baú, D. Bennett, L. Bergé, J.-P. Bernard, P. de Bernardis, G. Bordier, A. Bounab, É. Bréelle, E. F. Bunn, M. Calvo, R. Charlassier, S. Collin, A. Coppolecchia, A. Cruciani, G. Curran, M. de Petris, L. Dumoulin, A. Gault, M. Gervasi, A. Ghribi, M. Giard, C. Giordano, Y. Giraud-Héraud, M. Gradziel, L. Guglielmi, J.-C. Hamilton, V. Haynes, J. Kaplan, A. Korotkov,

J. Landé, B. Maffei, M. Maiello, S. Malu, S. Marnieros, J. Martino, S. Masi, A. Murphy, F. Nati, C. O'Sullivan, F. Pajot, A. Passerini, S. Peterzen, F. Piacentini, M. Piat, L. Piccirillo, G. Pisano, G. Polenta, D. Prêle, D. Romano, C. Rosset, M. Salatino, A. Schillaci, G. Sironi, R. Sordini, S. Spinelli, A. Tartari, P. Timbie, G. Tucker, L. Vibert, F. Voisin, R. A. Watson, M. Zannoni, and QUBIC Collaboration. QUBIC: The QU bolometric interferometer for cosmology. *Astroparticle Physics*, 34:705–716, April 2011.

[64] C. L. Reichardt, P. A. R. Ade, J. J. Bock, J. R. Bond, J. A. Brevik, C. R. Contaldi, M. D. Daub, J. T. Dempsey, J. H. Goldstein, W. L. Holzapfel, C. L. Kuo, A. E. Lange, M. Lueker, M. Newcomb, J. B. Peterson, J. Ruhl, M. C. Runyan, and Z. Staniszewski. High-Resolution CMB Power Spectrum from the Complete ACBAR Data Set. *ApJ*, 694:1200–1219, April 2009.

[65] B. Reichborn-Kjennerud, A. M. Aboobaker, P. Ade, F. Aubin, C. Baccigalupi, C. Bao, J. Borrill, C. Cantalupo, D. Chapman, J. Didier, M. Dobbs, J. Grain, W. Grainger, S. Hanany, S. Hillbrand, J. Hubmayr, A. Jaffe, B. Johnson, T. Jones, T. Kisner, J. Klein, A. Korotkov, S. Leach, A. Lee, L. Levinson, M. Limon, K. MacDermid, T. Matsumura, X. Meng, A. Miller, M. Milligan, E. Pascale, D. Polsgrove, N. Ponthieu, K. Raach, I. Sagiv, G. Smecher, F. Stivoli, R. Stompor, H. Tran, M. Tristram, G. S. Tucker, Y. Vinokurov, A. Yadav, M. Zaldarriaga, and K. Zilic. EBEX: a balloon-borne CMB polarization experiment. In *Society of Photo-Optical Instrumentation Engineers (SPIE) Conference Series*, volume 7741 of *Society of Photo-Optical Instrumentation Engineers (SPIE) Conference Series*, July 2010.

[66] J. A. Rubiño-Martín, R. Rebolo, M. Aguiar, R. Génova-Santos, F. Gómez-Reñasco, J. M. Herreros, R. J. Hoyland, C. López-Caraballo, A. E. Pelaez Santos, V. Sanchez de la Rosa, A. Vega-Moreno, T. Viera-Curbelo, E. Martínez-Gonzalez, R. B. Barreiro, F. J. Casas, J. M. Diego, R. Fernández-Cobos, D. Herranz, M. López-Caniego,

D. Ortiz, P. Vielva, E. Artal, B. Aja, J. Cagigas, J. L. Cano, L. de la Fuente, A. Mediavilla, J. V. Terán, E. Villa, L. Piccirillo, R. Battye, E. Blackhurst, M. Brown, R. D. Davies, R. J. Davis, C. Dickinson, S. Harper, B. Maffei, M. McCulloch, S. Melhuish, G. Pisano, R. A. Watson, M. Hobson, K. Grainge, A. Lasenby, R. Saunders, and P. Scott. The QUIJOTE-CMB experiment: studying the polarisation of the galactic and cosmological microwave emissions. In *Society of Photo-Optical Instrumentation Engineers (SPIE) Conference Series*, volume 8444 of *Society of Photo-Optical Instrumentation Engineers (SPIE) Conference Series*, September 2012.

[67] J. E. Ruhl, P. A. R. Ade, J. J. Bock, J. R. Bond, J. Borrill, A. Boscaleri, C. R. Contaldi, B. P. Crill, P. de Bernardis, G. De Troia, K. Ganga, M. Giacometti, E. Hivon, V. V. Hristov, A. Iacoangeli, A. H. Jaffe, W. C. Jones, A. E. Lange, S. Masi, P. Mason, P. D. Mauskopf, A. Melchiorri, T. Montroy, C. B. Netterfield, E. Pascale, F. Piacentini, D. Pogosyan, G. Polenta, S. Prunet, and G. Romeo. Improved Measurement of the Angular Power Spectrum of Temperature Anisotropy in the Cosmic Microwave Background from Two New Analyses of BOOMERANG Observations. *ApJ*, 599:786–805, December 2003.

[68] U. Seljak and M. Zaldarriaga. A Line-of-Sight Integration Approach to Cosmic Microwave Background Anisotropies. *ApJ*, 469:437, October 1996.

[69] G. F. Smoot, C. L. Bennett, A. Kogut, E. L. Wright, J. Aymon, N. W. Boggess, E. S. Cheng, G. de Amici, S. Gulkis, M. G. Hauser, G. Hinshaw, P. D. Jackson, M. Janssen, E. Kaita, T. Kelsall, P. Keegstra, C. Lineweaver, K. Loewenstein, P. Lubin, J. Mather, S. S. Meyer, S. H. Moseley, T. Murdock, L. Rokke, R. F. Silverberg, L. Tenorio, R. Weiss, and D. T. Wilkinson. Structure in the COBE differential microwave radiometer first-year maps. *ApJL*, 396:L1–L5, September 1992.

[70] H. Snoussi, G. Patanchon, J. F. Macías-Pérez, A. Mohammad-Djafari, and J. Delabrouille. Bayesian blind component separation for cosmic microwave background observations. In R. L. Fry, editor, *Bayesian Inference and Maximum Entropy Methods in Science and Engineering*, volume 617 of *American Institute of Physics Conference Series*, pages 125–140, May 2002.

[71] P.M. Sutter, Benjamin D. Wandelt, and Siddarth Malu. Bayesian angular power spectrum analysis of interferometric data. *Astrophys.J.Suppl.*, 202:9, 2012.

[72] G. B. Taylor, C. L. Carilli, and R. A. Perley, editors. *Synthesis Imaging in Radio Astronomy II*. Astronomical Society of the Pacific, August 1999.

[73] M. Tegmark, D. J. Eisenstein, W. Hu, and A. de Oliveira-Costa. Foregrounds and Forecasts for the Cosmic Microwave Background. *ApJ*, 530:133–165, February 2000.

[74] A. R. Thompson, J. M. Moran, and G. W. Swenson. *Interferometry and Synthesis in Radio Astronomy*. Wiley-VCH; 2 edition, April 2001.

[75] F. Vansyngel, B. D. Wandelt, and J. F. Cardoso. Semi-blind bayesian inference of cmb map and power spectrum. *In preparation*, 2014.

[76] B. D. Wandelt, D. L. Larson, and A. Lakshminarayanan. Global, exact cosmic microwave background data analysis using Gibbs sampling. *Phys. Rev. D*, 70(8):083511, October 2004.

[77] S. Weinberg. *Cosmology*. Oxford University Press, USA, April 2008.

[78] M. White, editor. *Anisotropies in the CMB*, 1999.

[79] M. White, J. E. Carlstrom, M. Dragovan, and W. L. Holzapfel. Interferometric Observation of Cosmic Microwave Background Anisotropies. *ApJ*, 514:12–24, March 1999.

[80] M. Zaldarriaga. The Polarization of the Cosmic Microwave Background. *Measuring and Modeling the Universe*, page 309, 2004.

[81] M. Zaldarriaga and U. Seljak. All-sky analysis of polarization in the microwave background. *Phys. Rev. D*, 55:1830–1840, February 1997.

[82] L. Zhang, A. Karakci, P. M. Sutter, E. F. Bunn, A. Korotkov, P. Timbie, G. S. Tucker, and B. D. Wandelt. Maximum Likelihood Analysis of Systematic Errors in Interferometric Observations of the Cosmic Microwave Background. *ApJS*, 206:24, June 2013.